3-2021

Data Driven Investigation into the Off-Axis BRDF to Develop an Algorithm to Classify Anisotropicity

Anne W. Werkley

DATA DRIVEN INVESTIGATION INTO THE OFF-AXIS BRDF TO DEVELOP AN ALGORITHM TO CLASSIFY ANISOTROPICITY

THESIS

Anne W. Werkley, 1st Lieutenant, USAF

AFIT-ENP-MS-21-M-140

DEPARTMENT OF THE AIR FORCE
AIR UNIVERSITY

AIR FORCE INSTITUTE OF TECHNOLOGY

Wright-Patterson Air Force Base, Ohio

AFIT-ENP-MS-21-M-140

DATA DRIVEN INVESTIGATION INTO THE OFF-AXIS BRDF TO DEVELOP AN ALGORITHM TO CLASSIFY ANISOTROPICITY

THESIS

Presented to the Faculty

Department of Engineering Physics

Graduate School of Engineering and Management

Air Force Institute of Technology

Air University

Air Education and Training Command

in Partial Fulfillment of the Requirements for the

Degree of Master of Science in Applied Physics

Anne W. Werkley, BS

1st Lieutenant, USAF

25 March 2021

AFIT-ENP-MS-21-M-140

DATA DRIVEN INVESTIGATION INTO THE OFF-AXIS BRDF TO DEVELOP AN ALGORITHM TO CLASSIFY ANISOTROPICITY

Anne W. Werkley, BS
1st Lieutenant, USAF

Committee Membership:

Lieutenant Colonel Samuel D. Butler, PhD
Chair

Dr. Michael A. Marciniak, PhD
Member

Dr. Manuel R. Ferdinandus, PhD
Member

Abstract

The Bi-directional Reflectance Distribution Function (BRDF) is used to describe reflectances of materials by calculating the ratio of the reflected radiance to the incident irradiance. BRDF is often modeled using microfacet models, which assume geometric optics. Many of these representations conjecture that the facets are distributed isotropically, and that radiation is scattered symmetrically about the specular peak, where $\theta_i = \theta_s$ and $\phi_s = \pi$ in spherical coordinates. While it was found that the isotropic models maintained symmetry about $\phi_s = \pi$, such symmetry was not maintained about the $\theta_s = \theta_i$ axis, except for close to the specular peak. This led to development of a novel data-driven metric for how isotropic a BRDF measurement is. The isotropic models were investigated along with anisotropic models to develop a metric of anisotropicity for a given material. As studies of the validity of anisotropic models have been limited in comparison to studies of isotropic microfacet models, this study investigated various anisotropic microfacet models, including the Ward BRDF model. Research efforts centered around developing an algorithm that could determine material anisotropy without having to fit to models. This algorithm was tested using high fidelity data, which was collected via a modified Complete Angle Scatter Instrument (CASI) with a CCD. The modified set-up captured off-axis data points, accounting for material anisotropies such as machine lining. The algorithm developed was able to accurately characterize the anisotropicity four out of five materials. The algorithm works for cases where the BRDF is higher than 100 1/sr. This algorithm bypasses the step of fitting data to models to determine anisotropy, and thus is subject less to the flaws associated with various microfacets models (such as improper modeling of grazing angle behavior). In doing so, this algorithm is intended

to improve BRDF characterization, ultimately improving the applications of light curve analysis, scene generation, and remote sensing.

Acknowledgments

Thank you to my parents, who have always supported my education and fostered my love of learning. I would not have made it without the support of my friends and family. Finally, thank you to my advisor, Lt Col Butler, for helping me through this arduous task. I appreciate that I could ask any question at any time and you would get back to me promptly, no matter how silly the question.

This material is based upon work supported by the Air Force Office of Scientific Research under award number F4FGA09014J002.

Anne W. Werkley

Table of Contents

Page

List of Figures

List of Tables

DATA DRIVEN INVESTIGATION INTO THE OFF-AXIS BRDF TO DEVELOP AN ALGORITHM TO CLASSIFY ANISOTROPICITY

I. Introduction

1.1 Motivation

As the demands of the warfighting domain increase, so does the need for an accurate and timely picture of the battlespace environment. Remote sensing is a key component that informs commanders and operators of this environment, filling in key gaps in the warfighter's picture. Remote sensing across both the visible and infrared (IR) wavelengths provides information about the physical features of a scene, as light reflected off a material's surface can apprise one of that material's properties [1]. With advancements in remote sensing, new sensors can be developed, improving technologies across the warfighting domain, including aircraft, satellites and munitions.

A fundamental aspect of these remote sensing processes is understanding the Bidirectional Reflectance Distribution Function (BRDF). BRDF is a description of how incident light reflects or scatters off of a material's surface, which can then be collected by a detector and provide information about the object [2]. BRDF changes as the material properties change, as an aluminum surface will reflect light differently than a copper surface, and a rough surface will reflect light more evenly across a hemisphere compared to a smooth surface. In accurately modeling the BRDF, one can use the function to perform more accurate remote sensing [1] [3]. BRDF can also be used in light curve analysis, as accurate characterization of reflectance data (for space-based objects) allows one to identify other properties of satellites (such as geo-

metric properties) [4]. For example, understanding the reflectance of solar panels on satellites can allow a Space Force operator to determine the orientation of a satellite.

1.2 Research Objective

Currently, the BRDF models used for most applications are geometric approximations of reflection. These models are known as microfacet models, and simplify physical optics models, which often are computationally expensive. The microfacet models work by fitting data to a series of parameters, such as σ_g, which represents the distribution of facets, and is proportional to how smooth or rough a surface is [5]. Essentially, by fitting the data to the models, one can determine the material composition and surface characteristics of a sample. The models have no predictive ability; they are merely empirical [6]. This is problematic in that some models fit some samples better than others; there is no streamlined method to determine surface characteristics other than by fitting BRDF data. For example, to determine if a sample reflects light isotropically, one must first fit the BRDF data to an isotropic model to determine quality of fit, which in turn determines the degree of material isotropy.

This study instead proposes an algorithm in which no fits to models are required to determine surface characteristics. Instead, the algorithm relies solely upon the actual BRDF data to determine the degree of surface isotropy or anisotropy. In this paper, anisotropy is given to mean any surface that produces directionally dependent reflection. This can be due either to a material with directionally dependent characteristics, such as machine linings or a change in material across a surface (an inhomogeneous sample). The algorithm is blind to which type of anisotropy is present in the sample; it merely detects to what extent isotropy is broken. In doing such, the algorithm prevents a user from erroneously fitting anisotropic data to isotropic

BRDF models.

The algorithm relies upon a series of image processing techniques to analyze the degree of rotational symmetry or isotropy present in the BRDF data. This is done by transforming the BRDF (in scatter coordinate space) into contour plots in direction cosine space. BRDFs that maintain rotational symmetry in direction cosine space as θ_i increases are due to more isotropic surfaces, and the degree to which this symmetry is broken determines how anisotropic a surface is. Ultimately, the developed algorithm successfully classified four out of five samples of varying degrees of anisotropy. The algorithm was found to work best for highly specular materials, as BRDFs (produced by simulated data sets) below 100 sr^{-1} cannot be classified by the algorithm. While some refinement is needed to fine tune the algorithm (especially for the diffuse cases), this study demonstrates that material classification is possible without requiring data fits to a model (some of which can be flawed).

1.3 Document Structure

This paper outlines the development and effectiveness of this algorithm, beginning with more background on microfacet models and the current state of research on anisotropic/out-of-plane BRDFs (Chapter 2). From this background, investigation began into isotropic and anisotropic microfacet models to determine key characteristics of isotropic and anisotropic materials. In these investigations, an algorithm was developed to classify materials based on their degree of anisotropicity. The details of these investigations and development of the algorithm are detailed in Chapter 3. In Chapter 4, the algorithm is laid out in full detail (in Section 4.2). BRDFs of five different samples were processed by the algorithm and the results were analyzed in this chapter. Chapter 5 provides a conclusion and recommendations for future work.

II. Background

2.1 BRDF

The Bidirectional Reflectance Distribution Function (BRDF) describes how incident radiation is scattered or reflected off a surface, and is the ratio of the reflected radiance to the incident irradiance as defined by Nicodemus [2]:

$$f_r(\hat{\omega}_i, \hat{\omega}_s, \lambda) = \frac{dL_r(\hat{\omega}_i, \hat{\omega}_s, \lambda)}{dE_i(\hat{\omega}_i, \lambda)}. \tag{2.1}$$

where f_r is the BRDF, $\hat{\omega}_i$ represents the incident vector with respect to the material's surface normal, $\hat{\omega}_s$, represents the outgoing or "scattered" vector, L_r, the reflected radiance, E_i, the incident irradiance, and λ, the respective wavelength. In this study, only one wavelength was used to illuminate samples, and thus wavelength dependence will not be considered here. Figure 2.1 illustrates the incidence and scattering angles [7].

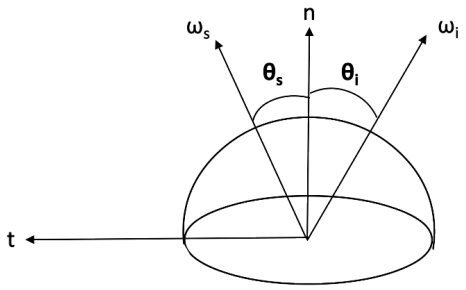

Figure 2.1: This diagram is a 2D representation of the 3D incidence, $\hat{\omega}_i$ and scatter, $\hat{\omega}_s$ vectors for BRDF. This coordinate system can be directly mapped to spherical coordinates, where θ_i and θ_s represent the in-plane direction, and ϕ_i and ϕ_s (not shown) are the out of plane direction.

Surface reflections are more readily modeled if the material's surface is characterized as specular or diffuse. In the specular case, electromagnetic radiation tends to reflect

in accordance with Snell's Law, where the reflected light scatters at an angle (in spherical coordinates) of θ_i=θ_s and ϕ_s=π radians [8]. This notation here assumes the convention where ϕ_i=0, so that ϕ_s=π radians constitutes forward scatter for isotropic materials. With anisotropic materials, ϕ_i is surface dependent [5]. For the perfectly diffuse or Lambertian case, light tends to scatter evenly about a hemisphere, so that the BRDF can be modeled as:

$$f_r = \frac{\rho_d}{\pi} \tag{2.2}$$

where ρ_d represents the diffuse reflectance of a given material [1].

However, in most cases, scattering cannot be discretely categorized as a specular nor as a Lambertian reflection. Modeling efforts must employ a more sophisticated approach. There are typically two approaches to modeling BRDF: physical optics models and microfacet models. The physical optics approach starts with first principles by solving Maxwell's equations at a rough surface. This approach is typically very computationally expensive and not feasible for most Air Force applications, as it requires fully characterizing the surface or optical roughness and calculating the field reflected from the surface. As such, the majority of this work shall focus on microfacet models.

2.2 Physical Optics Models

Before delving into the details of the microfacet models, this work will first enumerate on physical optics models and their relation to microfacet models. These models begin with a surface transfer function, which is the phase shift produced by the surface. The Fourier transform of this function is the Angle Spread Function (ASF), which is related to the BRDF and is equivalent to such in the case of total Fresnel reflectance.

This formulation (Equation (2.3)) of the Angle Spread Function (ASF) from the

Modified Beckmann Kirchoff Model uses a Gaussian distribution function to describe the surface statistics [9] [10] [11].

$$f_a = \frac{\pi l_c^2 K e^{-g}}{\lambda^2} \sum_{n=1}^{\infty} \frac{g^m}{m!m} exp(-\frac{v_{xy}^2 l_c^2}{4m}) \tag{2.3}$$

$$g(\theta_i, \theta_s) = (\frac{2\pi\sigma_s}{\lambda})^2 (\cos(\theta_i) + \cos(\theta_s))^2 \tag{2.4}$$

In Equations (2.3) (2.4), l_c is the correlation length or how often the surface repeats, K is a term that accounts for conservation of energy (as the original model used a paraxial approximation [11]), and σ_s is the surface height standard deviation. v_{xy} is related to the angular extent in direction cosine space by the wave vector, k. (Direction cosine space will be explained in greater detail in Section 2.5.)

For the microfacet models, the terms in the physical optics models can be related to the terms in the microfacet models, specifically when a Gaussian distribution function is used. For example, the Gaussian width for a rough surface σ_g is essentially the probability distribution of microfacet normals, related to σ_s and l_c [12].

$$\sigma_{g,vr} = \frac{\sigma_s \sqrt{2}}{l_c} \tag{2.5}$$

For glossier materials, the Gaussian width varies with wavelength, and shows that the microfacet regime does not work well for a highly polished material, as the distribution should not vary with wavelength. [12].

$$\sigma_{g,p} = \frac{\lambda}{\pi l_c \sqrt{2}} \tag{2.6}$$

Despite the issues in the glossier regime with respect to σ_g, physical optics models were not used in this study. This is due to the fact that the ASF (Equation (2.3)) relies upon an infinite summation, making it computationally expensive for use in

most Air Force applications. An additional issue with this formulation for the ASF is that it relies upon Gaussian surface statistics, which does not necessarily describe all surfaces well.

2.3 Microfacet

The microfacet models start with a geometric optics approximation to simplify the computational complexity, making modeling the BRDF more tractable for most applications, including light curve analysis and scene generation. These models approximate a rough surface as a set of microfacets from which electromagnetic waves are reflected. Figure 2.2 illustrates the incident $\hat{\omega_i}$ and outgoing vectors $\hat{\omega_o}$ relative to the overall surface normal $\hat{z}$, and was formally defined in both the θ and ϕ dimensions by Rusinkiewicz [7].

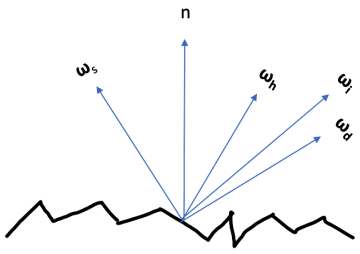

Figure 2.2: This 2D diagram of the 3D microfacet geometry illustrates how there is an overall macrosurface normal, n, with ω_i and ω_s as the incident and scattered radiation relative to n. ω_d is the incident vector with respect to the specified microfacet, and ω_h is the orientation or surface normal of the specified microfacet. Reproduction of Fig. 1 in [13].

While the microfacet models employ the paraxial approximation at the microfacet surface, the models also incorporate elements of physical optics models. These borrowed terms include the Fresnel reflectance, as well as Lambertian and specular terms.

Generically, microfacet models include a surface reflection term, ρ_s, which consti-

tutes a specular reflection and the first term in Equation (2.7), a volumetric scattering term (the second term), $\rho_v \mathrm{V}(\omega_i, \omega_o)$ and a Lambertian scattering term, ρ_d/π (the final term) [13]. Butler described the generic terms [13] in Equation (2.7).

$$f_r(w_i, w_o) = \rho_s P(\hat{\omega_i}, \omega_s) D(\hat{\omega_h}) F(\theta_d) G(\hat{\omega_i}, \hat{\omega_s}) \sigma(\theta_i, \theta_s) + \rho_v V(\hat{\omega_i}, \hat{\omega_s}) + \frac{\rho_d}{\pi} \tag{2.7}$$

Breaking down each component of Equation (2.7) beyond what was described previously, P merely represents a prefactor term included for some of the microfacet models to get each in the same form [13]. $\sigma(\theta_i, \theta_s)$ is a term used to convert from scattering cross section to BRDF [13]. F is the Fresnel reflection, which will be described in Equations (2.12)-(2.14).

Equation (2.7) can be used to describe several microfacet models [13] to include the Sandford-Robertson [3], Blinn-Phong [14], Torrance-Sparrow [15] and Cook-Torrance models [16]. Most of the development of these models took place in the late 1960s to early 1980s, generally with the intention of improving computer graphics.

The Cook-Torrance model was developed by a group out of Lucasfilm and Cornell University, and it took various aspects of previous microfacet models and improved upon those models [16]. Cook and Torrance began with the assumption that the surface was composed of various microfacets with differing orientations, similar to the previously described microfacet geometry. Their BRDF formulation consisted of a linear combination of specular and diffuse components [16]. The specular and diffuse components were modeled separately. For the specular component, the BRDF was modeled as shown in Equation (2.8) [16].

$$R_s = \frac{F}{\pi} \frac{DG}{(\mathbf{N} \cdot \mathbf{L})(\mathbf{N} \cdot \mathbf{V})} \tag{2.8}$$

In this equation, F merely represents the Fresnel reflectance, and N the overall surface

normal. L and V are respectively ω_i and ω_o in Equation (2.1).

G, in both Equations (2.8) and (2.7) represents the geometric attenuation factor and describes the shadowing and masking of one facet's reflections by another facet [13]. "Shadowing" and "masking" terms imply that the reflection off of certain facets can be blocked by another facet, so that the reflected light is not captured by the detector.

D describes the distribution of facet normal orientations. The more facets oriented in the direction of the microfacet surface normal, described by θ_h, the more specular reflection that occurs at the surface as opposed to diffuse reflection. D can be described by a multitude of distributions, including Blinn's Gaussian model [14] (Equation (2.9)) and Beckmann's model [11] (Equation (2.10)). These equation rely upon θ_h and m, which is a term that controls the width of the Gaussian and is related to the specularity/diffusivity of a surface.

$$D = c * Exp\left[-\left(\frac{\theta_h}{m}\right)^2\right] \tag{2.9}$$

$$D = \frac{1}{\pi m^2 \cos^4(\theta_h)} Exp\left[-\left(\frac{\tan(\theta_h)}{m}\right)^2\right] \tag{2.10}$$

Cook and Torrance explored both of the distribution functions and found advantages to using both distribution functions. Beckmann's model accounts for wavelength dependence, but it adds complexity to calculations. Cook and Torrance found that the Blinn distribution models were easiest to calculate, but did not describe as comprehensively rougher surfaces when compared to the Beckmann distribution in Equation (2.10) [16]. Ultimately, the Beckmann distribution accounts for the transition region between physical and geometrical optics, which makes it more suitable for use in isotropic microfacet BRDF models [16].

Beyond the distribution functions used by Cook Torrance model, Hyper-Cauchy

distributions have also been used in BRDF microfacet models to describe the orientation of the facet normals (Equation (2.11)) [13]. As this study focuses on anisotropic models as well as isotropic models, this distribution function will be largely ignored, as there exists merely a Beckmann and cosine lobe formulation for anisotropic models. However, in Equation (2.11), q and s are parameters used to control the width of the distribution function.

$$D_g(\theta_h) = \frac{(q-1)(s\sqrt{2})^{2q-2}}{\pi \cos^4(\theta_h)((s\sqrt{2})^2 + \tan^2(\theta_h))^q} \tag{2.11}$$

Both the diffuse and specular terms depend on F, the Fresnel reflectance. The Fresnel reflectance is split into the specular, ρ_s and diffuse reflectance, ρ_d in Butler's formulation [13]. Cook and Torrance modeled these terms by assuming that the extinction coefficient k goes to zero. The diffuse reflectance term is assumed to be Lambertian, and is modeled as the reflectance, ρ_d multiplied by $1/\pi$. The Fresnel reflectance is described by Equations (2.12), (2.13), and (2.14). Here n indicates the index of refraction of the material, and the perpendicular ($\perp$) and parallel ($\parallel$) terms indicate the polarization of light. The two terms are combined in Equation (2.14) to get unpolarized light [8].

$$\rho_\perp(\theta_i, n) = \left| \frac{\cos(\theta_i) - n\sqrt{1 - \sin(\frac{\theta_i}{n})^2}}{\cos(\theta_i) + n\sqrt{1 - \sin(\frac{\theta_i}{n})^2}} \right|^2 \tag{2.12}$$

$$\rho_\parallel(\theta_i, n) = \left| \frac{-n\cos(\theta_i) + \sqrt{1 - \sin(\frac{\theta_i}{n})^2}}{n\cos(\theta_i) + \sqrt{1 - \sin(\frac{\theta_i}{n})^2}} \right|^2 \tag{2.13}$$

$$\rho(\theta_i, n) = \frac{\rho_\perp(\theta_i, n) + \rho_\parallel(\theta_i, n)}{2} \tag{2.14}$$

These equations have been derived from Maxwell's equations. In the majority of

BRDF models these equations are used, with a few exceptions, including the Sandford-Robertson model. [13].

Ewing improved upon the description of both the Fresnel reflectance and Geometric attenuation term in microfacets by including a Rayleigh-Rice polarization factor, Q. This factor was better able to approximate grazing angle behavior (cases where θ_i approaches 90°), which was notoriously poorly characterized in previous models [17]. The inclusion of the Q term also better accounts for the previously described geometric attenuation term, G, especially when modeling anisotropic materials [18]. The new formulation encompassed describing the Fresnel term as Q/2, and the geometric attenuation term as proportional to Q/F, where F is the Fresnel reflectance. Equations (2.15), 2.16), (2.17), (2.18) below provide a summary of Ewing's work. Note the angles with the subscript s denote the scattered angle. The subscripts for each of the Q factors represent a different polarization of light, where light can be polarized in both perpendicular (s) or parallel (p), or a combination of the two. The unpolarized light is a summation of these four polarization states [17]. $\widetilde{n}$ in these equations below is equal to n+iκ, where n and κ are respectively the real and complex indices of refraction. $\alpha_{i,s}$=$\sqrt{\widetilde{n}^2 - \sin^2(\theta_{i,s})}$ in these equations.

$$Q_{ss} = \left| \frac{[\widetilde{n}^2 - 1]\cos(\phi_s - \pi)}{[\cos(\theta_i) + \alpha_i][\cos(\theta_s) + \alpha_s]} \right|^2 \tag{2.15}$$

$$Q_{sp} = \left| \frac{[\widetilde{n}^2 - 1]\alpha_s \sin(\phi_s - \pi)}{[\cos(\theta_i) + \alpha_i][\widetilde{n}^2\cos(\theta_s) + \alpha_s]} \right|^2 \tag{2.16}$$

$$Q_{ps} = \left| \frac{[\widetilde{n}^2 - 1]\alpha_s \sin(\phi_s - \pi)}{[\widetilde{n}^2\cos(\theta_i) + \alpha_i][\cos(\theta_s) + \alpha_s]} \right|^2 \tag{2.17}$$

$$Q_{pp} = \left| \frac{[\widetilde{n}^2 - 1]\alpha_i\alpha_s \cos(\phi_s + \pi) - \widetilde{n}^2 \sin(\theta_i)\sin(\theta_s)}{[\widetilde{n}^2\cos(\theta_i) + \alpha_i][\widetilde{n}^2\cos(\theta_s) + \alpha_s]} \right|^2 \tag{2.18}$$

2.4 Studies Using Experimental Data

This study employs experimental data to assess the off-axis or out-of-plane nature of BRDF. The earlier efforts to do so were somewhat limited in scope, in that the researchers mainly used experimental data to assess the ability of various models to compute isotropic BRDFs. Generally, the assessment of off-axis data was limited to the collection and cursory analysis of such data.

Matusik from MIT was the first of these researchers to carry out a comprehensive effort to capture high fidelity data and assess various BRDF models using such data. More often than not, BRDF models, to include the Cook and Torrance BRDF model, are "physically inspired" analytic models providing approximations of the reflectance of materials [19]. Researchers prior to Matusuik were able to acquire measurements to assess these models, but the BRDFs were relatively sparsely sampled. Matusik captured this data via image-based techniques, capturing "330 high dynamic range pictures," treating each pixel captured as a separate BRDF measurement [19]. In total, 20-80 million BRDF measurements were captured for each material. While these measurements constituted a high dynamic range, it was not the ten orders of magnitude required for measuring specular BRDFs, working better for more diffuse materials. Ultimately, Matusik leveraged these measurements to interpolate and extrapolate new BRDFs and generate a surface reflectance model [19].

Ngan expanded upon Matusik's efforts by using his measurements to evaluate the performance of various prevalent/notable BRDF models. Ngan also collected data on four anisotropic materials to analyze the models' characterization of the off-axis behavior, discarding data collected at angles close to grazing angles [18]. Generally, Ngan's group found that most isotropic materials could be represented well by models that were more physically based. They concluded that models with more explicit modeling of the Fresnel reflectance produced the best fits of the data

[18]. Most of the models fell short in simulating anisotropic materials with more complex micro-geometry. They found that models fell short of adequately capturing the shadowing/masking or geometric attenuation aspects of BRDF [18]. This study signaled that models fell short of adequately characterizing off-axis behavior [18].

Most of the research thrusts involving anisotropic behavior, past Ngan's, have been improving methods of collecting anisotropic measurements. These include two studies done by Filip, one using a gonionoreflectometer, and another using an ellipsoidal mirror and a compact camera [20]. Filip's group mainly focused on the quality of the measurements as opposed to the experimental analysis of the models Ngan carried out.

2.5 Direction Cosine Space

In general, majority of the models analyze BRDF in the coordinate system defined by Rusinkiewicz [12]. However, some of the analysis work has been done in direction cosine space, such as studies conducted by Harvey. The conversion to coordinate space involves taking the measurements in spherical coordinate space and converting the coordinates to $\Delta\alpha$ and $\Delta\beta$, which can be correlated to the parameters of physical optics models mentioned in Section 2.2. The conversion is enumerated in Equations (3.12)-(3.14) [12]. Looking closely, one can pull out the $\tan^2(\theta_h)$ term from the isotropic Beckmann distribution function. Thus, the isotropic distribution function is symmetric in direction cosine space [12].

$$\Delta\alpha = \sin(\theta_s)\sin(\phi_s - \pi) \tag{2.19}$$

$$\Delta\beta = \sin(\theta_s)\cos(\phi_s - \pi) - \sin(\theta_i) \tag{2.20}$$

$$\tan^2(\theta_h) = \frac{\Delta\alpha^2 + \Delta\beta^2}{\cos(\theta_i) + \cos(\theta_s)} \tag{2.21}$$

This coordinate system was developed by Harvey as a result of studies involving physical optics BRDF models. When Harvey plotted radiance measurements in direction cosine space, the measurements were shift-invariant, meaning that regardless of incidence angle, all of the radiance measurements were the same if scattered off of the same material [21]. This is not necessarily the case for BRDF measurements, as optically smooth surfaces tend to be more shift-invariant than rougher surfaces. Generally, BRDF measurements vary in magnitude with incidence angle and the location of the peak BRDF can shift off of zero in direction cosine space, as the surface becomes rougher and θ_i increases [21]. For optically smooth and isotropic surfaces, the BRDF is rotationally symmetric, maintaining the same diameter for in-plane measurements as θ_i varies [21]. However, this also suggested that rotational symmetry would be broken if a material is anisotropic. In an experimental study, Butler found that measurements of both optically smooth and rough surfaces can be scaled by the directional hemispheric reflectance (DHR) and a cross section conversion term ($\cos \theta_i \sin \theta_s$) to align BRDF measurements in direction cosine space. The study took data at θ_i=20°, 30°, 40° and 50°, to avoid measurements at grazing angles [22].

2.6 Summary

This chapter discussed the general geometric representations of BRDF, as well as the microfacet models used to characterize BRDF. The various terms of these models were discussed, such as the distribution function and geometric attenuation term. Finally, direction cosine space was discussed as a coordinate space in which isotropy can be established.

III. Methodology

3.1 Introduction

This chapter outlines the methodology developed to assess the anisotropicity of BRDF data. This methodology was developed by first investigating isotropic models, determining which behaviors remained constant while parameters of the models were changed. It was found that symmetry about ϕ_s=π radians is a key component of isotropicity, given that $\phi_i = 0$ for isotropic materials. (This is not the case for anisotropic materials, as ϕ_i is surface dependent). After investigating isotropic models, anisotropic BRDF models were investigated to find behavior unique to anisotropic materials. This study exposed flaws in current anisotropic models. From there, simulated data was produced by isotropic models and transformed to direction cosine space. Using image processing techniques, information about the symmetry in direction cosine space was used to signify isotropy. Some of these parameters included the eccentricity of contour plots. From the results of these investigations, an algorithm was developed. Using this algorithm, signature beam data was smoothed and fit to verify the results found with the simulated data. The combination of the results from the simulated data and signature beam established baselines for what is considered an isotropic material.

3.2 Generating Simulated Data

In order to develop a methodology or algorithm to assess the degree of isotropy of BRDF data, simulated data was first created. For isotropic BRDFs, the Beckmann distribution in the form of Equation (3.1) was used (the terms in these equations are described earlier in Chapter 2). For anisotropic BRDFs, the distribution function in the form of Equation (3.2) was used. These distribution functions were then

plugged into Equation (3.3) to generate simulated data. As mentioned previously, θ_h references the orientation of the facet normals. For isotropic materials, no ϕ_h term exists in Equation (3.1) as ϕ_i=0. However, this is not the case for anisotropic materials, where ϕ_i depends on the material's surface, and thus the presence of the ϕ_h term in Equation (3.2).

$$D_g(\theta_h) = \frac{1}{2\pi\sigma_g^2 \cos^4(\theta_h)} exp\left[-\left(\frac{\tan^2(\theta_h)}{2\sigma_g^2}\right)\right] \tag{3.1}$$

$$D(\hat{\omega}_h) = \frac{1}{\pi m_x m_y \cos^4\theta_h} exp\left[-\tan^2\theta_h\left(\frac{\cos^2\phi_h}{m_x^2} + \frac{\sin^2\phi_h}{m_y^2}\right)\right] \tag{3.2}$$

$$f_r(\theta_i, \theta_s, \phi_s, \sigma_g) = (\rho_s D_{beckmann}\frac{Q}{2}\sigma + \frac{\rho_d}{\pi})\cos(\theta_i)\cos(\theta_s) \tag{3.3}$$

In Equation (3.3), ρ_s is set to 0.9, to simulate mainly specular reflection and σ represents a cross-section conversion term to spherical coordinates $(\cos\theta_i \cos\theta_s)^{-1}$. The Q term uses the index of refraction for Gold, with n=0.27732 and κ=2.9278 [23], and ρ_d=0.05 to model diffuse reflectance. BRDFs are then generated by plugging in either set values or arrays of θ_i, θ_s, ϕ_i and ϕ_s to generate a BRDF that extends a full hemisphere in scatter coordinate space. BRDFs are then plotted in scatter coordinate space as a contour plot to generate a "simulated BRDF."

3.3 Investigation of Isotropic Models

For BRDF microfacet models, the model has a heavy dependence on the distribution function term. As such, the study focused at first on the distribution function. The Beckmann distribution function (Equation (3.1)) was the focus of this isotropic study as it has been found to be computationally inexpensive while accurate for both optically smooth and rough surfaces.

As the distribution function has a heavy dependence upon θ_h, the impact of vary-

ing θ_i, θ_s and ϕ_s on θ_h was first investigated. Equation (3.1) above was modeled computationally, where σ_g was varied, θ_i was set to a constant value (15°, 20°, 40°, 45° or 60°), ϕ_i was set to 0°, θ_s varied from 0° to 90° and ϕ_s varied from 0° to 360°. ϕ_i was set to zero, as this is this standard convention to model forward scattering occuring at ϕ_s=π. The plots in Figure 3.1-3.2 show that the peaks of the distribution function occur at θ_i =θ_s and ϕ_s =π, which is the specular peak.

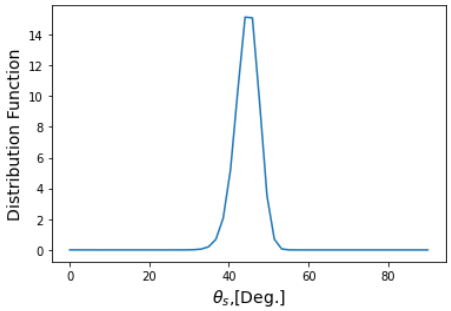

Figure 3.1: 2D slice of θ_s in scatter coordinate space plotted against the distribution function (in arbitrary units). θ_i = 45° and σ_g=0.1 in this plot, and the peak occurs at θ_i=θ_s and ϕ_s=180°, respectively.

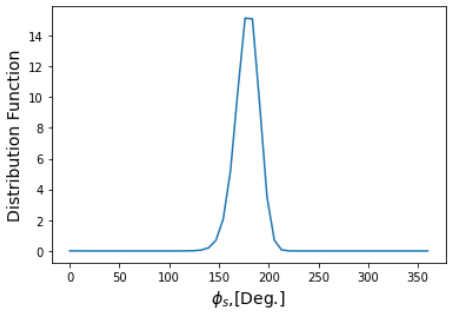

Figure 3.2: 2D slice of $_s$ in scatter coordinate space plotted against the distribution function (in arbitrary units). θ_i=45° and σ_g=0.1 in this plot, and the peak occurs at θ_i=θ_s and ϕ_s=180°, respectively.

When plotting in θ_h space, it was verified that θ_h is zero at the specular peak of θ_s=θ_i and ϕ_s = π. Additionally, as θ_i increased, the region where θ_h was near zero decreased, meaning that the distribution function spreads out from the specular peak as θ_i increases. These findings are summarized in Figure 4.40 where θ_h is plotted against the distribution function.

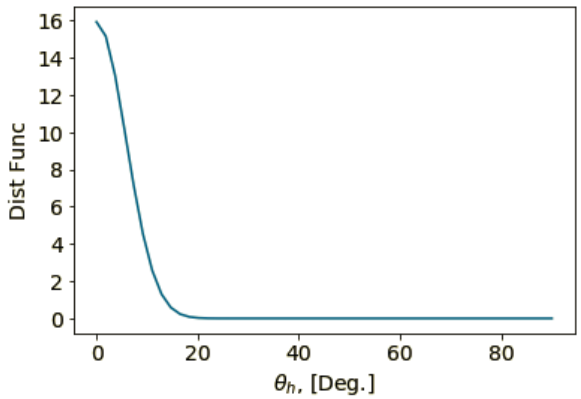

Figure 3.3: This plot shows θ_h plotted against the distribution function (in arbitrary units), where σ_g=0.1, and $\theta_i = 45°$. As one can see here, as θ_h moves off of zero, the distribution function drops off significantly. As θ_i increases, the distribution function begins to spread out from the peak at θ_h=0, meaning that the distribution function spreads out in scatter coordinate space.

The specular peak of θ_i=θ_s and ϕ_s=π continues to be of importance, as the distribution function reaches a maximum at the specular peak. For optically smooth surfaces, the distribution function is strongly concentrated at the peak, and is more spread out in scatter space for rougher surfaces, where σ_g is larger. While σ_g itself does not directly correspond to how optically rough/smooth the surface is, as it more so represents the orientation of facets, the two properties can be related to one another. Figures 4.40-3.5show the impact of changing σ_g, keeping θ_i constant. The impact of changing θ_i is that the peak of the plot shifts in scatter space to where θ_s=θ_i.

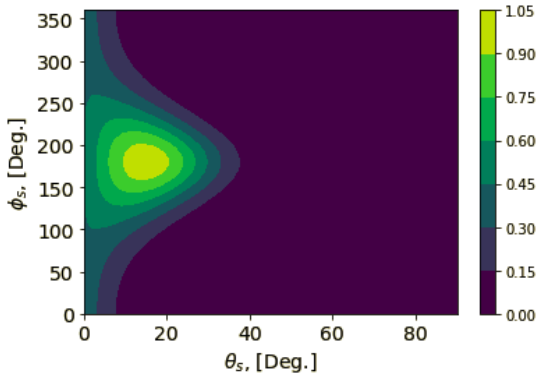

Figure 3.4: Contour plots in scatter coordinate space of the distribution function (in arbitrary units). The colorbar represents the distribution function divided by the maximum value for easier comparison. $\theta_i = 15°$ and σ_g=0.1 in this plot.

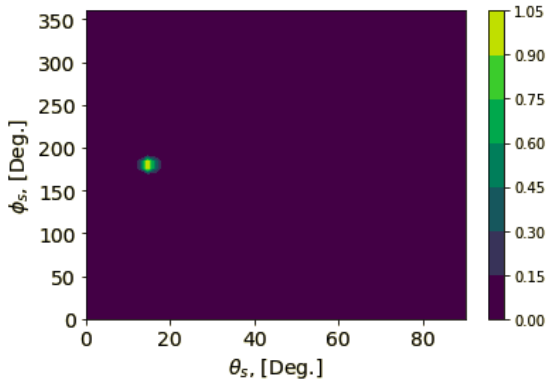

Figure 3.5: Contour plots in scatter coordinate space of the distribution function (in arbitrary units). The colorbar represents the distribution function divided by the maximum value for easier comparison. $\theta_i = 15°$ and σ_g=0.01 in this plot.

Upon verifying these characteristics of the distribution function, the symmetry of the distribution function about the specular peak in scatter coordinates was investigated. This investigation was part of an attempt to determine what makes a material isotropic. The symmetry was first investigated about the point ϕ_s=π. The first attempt to determine symmetry was to step off of ϕ_s=π in steps of $\pi/4$ radians to determine if there were any differences moving in ϕ_s. A difference plot (for the distribution function normalized by the maximum value) between ϕ_s= $3\pi/4$ and $5\pi/4$ radians for σ_g=0.1 was generated. It was found that there was little difference

between the two plots, excepting some computational rounding errors (on the order of 1×10^{-12}), as seen in Figure 3.6.

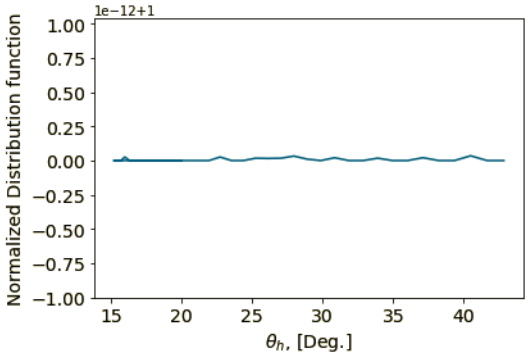

Figure 3.6: This plot shows the difference between the normalized (divided by maximum value) distribution functions when θ_i and σ_g are kept constant at 40°, and 0.1 respectively and ϕ_s is varied from $3\pi/4$ to $5\pi/4$ (in radians). As one can see, the difference is minimal, on the order of 1×10^{-12}, which is likely due to computational rounding error in the trigonometric functions.

This can also be shown analytically, using Equations (3.4)-(3.5) for the in-plane relationship between θ_h, θ_i, θ_s and ϕ_s.

$$2\cos(\theta_d) = \cos(\theta_i)\cos(\theta_s) + \sin(\theta_i)\sin(\theta_s)\cos(\phi_s) \tag{3.4}$$

$$\cos(\theta_h) = \frac{\cos(\theta_i) + \cos(\theta_s)}{2\cos(\theta_d)} \tag{3.5}$$

To evaluate symmetry about ϕ_s=π, an arbitrary θ_i and θ_s were kept constant and plugged into the distribution function (Equation (3.1)). The relationship in Equation (3.6) was found (where b can be any number) showing that the distribution function is symmetric about ϕ_s=π analytically, regardless of distance from this point.

$$D(\theta_i, \theta_s, \pi + b) - D(\theta_i, \theta_s, \pi - b) = 0 \tag{3.6}$$

When this methodology was extended to the θ_s direction, the symmetry did not hold nearly as well. For small changes in θ_s (on the order of 0.5°), the differences

between the distribution function were minimal (at most a difference of 0.2). However, this difference is still significant in comparison to the differences between moving off the peak in steps of ϕ_s. These differences moving in θ_s are exacerbated as σ_g increases, as the maximum difference for σ_g=0.01 is 1.5 in comparison to the 0.2 difference for σ_g=0.1. While these comparisons were done for specific θ_i and σ_g, these differences were also generalized first by finding an analytic expression, as found with Equation (3.6) and then by taking the Taylor series expansion about θ_h=0, (i.e. the specular peak), to validate these specific cases. Analytically, the expression for the symmetry about θ_i=θ_s reduced to:

$$D(\theta_i, \theta_i{+}b, \phi_s){-}D(\theta_i, \theta_i{-}b, \phi_s) = \frac{8}{\pi}\frac{-1}{\cos(b-\theta_i)+\cos^4(\theta_i)}Exp[\frac{-2-\cos(b+\phi_s)+...}{8\cos(b-\theta_i)+Cos^4(\theta_i)}]{+}... \tag{3.7}$$

As shown in Equation (3.7), this does not reduce to a clean expression, indicating that symmetry is not maintained about θ_i=θ_s, if one moves a distance b off this point. For the Taylor series expansion about θ_h=0, the expression for the distribution function reduced to:

$$D(\theta_h) = \frac{1}{2\pi\sigma_g^2} + \frac{\theta_h^2(-1+4\sigma_g^2)}{4\pi\sigma_g^4} \tag{3.8}$$

The same expansion was then applied to the case where θ_s=θ_i with the expectation that this case would also reduce to a clean expression, as one is moving only a small distance in θ off of θ_i=θ_s. However, such was not the case, and thus the expression is not included here. When specific values were plugged in for θ_i and ϕ_s, the same issue resulted. Thus, the previous findings with specified θ_i, σ_g were all that one could conclude using the isotropic distribution functions. Even though these were specific cases, a number of σ_g values from 0.01 to 0.1 in intervals of 0.01 was investigated to determine differences in the distribution function stepping in ϕ_s and θ_s. Based upon these results, it has been safely concluded that the isotropic distribution function

maintains symmetry in scatter space about ϕ_s=π but not about θ_i=θ_s.

The distribution function was then extended to the full BRDF to verify that close investigation of the distribution function for "isotropicity" was a legitimate method. The full BRDF followed the form of:

$$f_r = \rho_s D(\theta_h) F \sigma + \rho_d / \pi \tag{3.9}$$

where ρ_s was set to 0.9, ρ_d set to 0.05, D was Equation (2.1), σ is a cross section conversion term, described in the background section, and F was either the Fresnel reflection (Model 1) or a Q/2, Rayleigh-Rice Polarization Term (Model 2). The equations describing these models are listed in Chapter 2. Difference plots were generated in scatter coordinate space for both of these cases. n and κ for the Fresnel dependent terms were set to 0.27732 and 2.9278i, respectively, which are the indices of Gold from 0.1879-1.937 μm [23]. The results of the difference plots are shown in Figure 3.7-3.8.

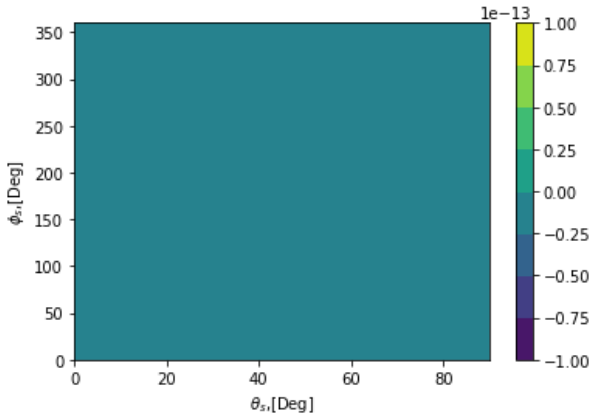

Figure 3.7: Model 1 using the Fresnel reflectance term compared with the distribution function.

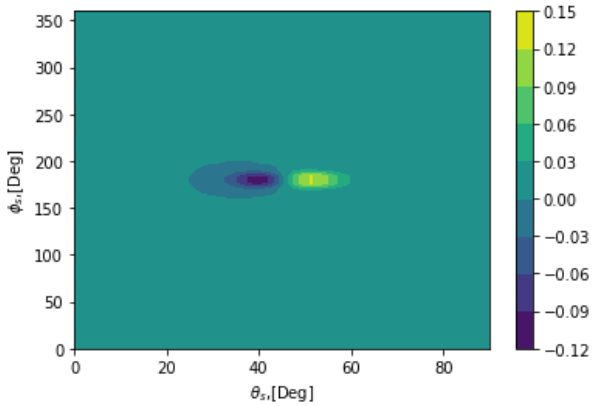

Figure 3.8: Model 2 using the Rayleigh-Rice Polarization Term compared with the distribution function.

While there are no significant differences between the distribution function and Model 1, near the specular peak there are noticeable differences between Model 2 and the distribution function. Since these plots are on a relative scale, where each model has been scaled by its maximum value, differences of 0.15 are somewhat significant. However, Model 2 handles behavior at grazing angles better than Model 1, as shown in Figures 3.9-3.10.

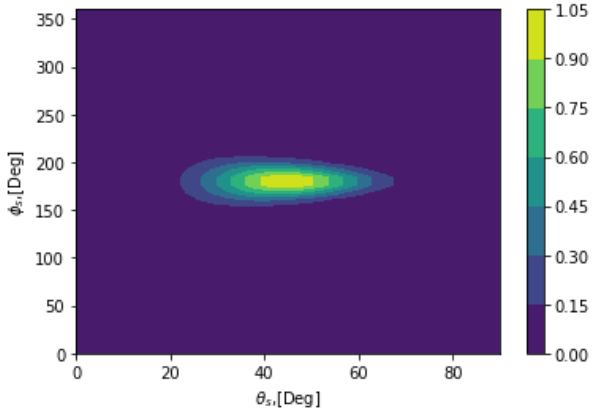

Figure 3.9: Model 1 Full Normalized BRDF with σ_g=0.1, and θ_i=45°.

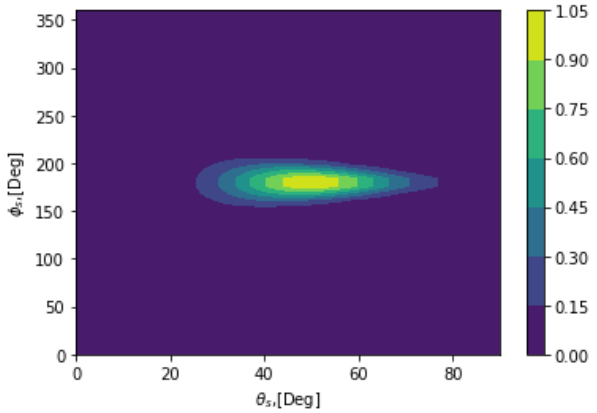

Figure 3.10: Model 2 Full Normalized BRDF with σ_g=0.1, and θ_i=45°.

While there were differences between the full BRDF and the distribution function, it was investigated whether the symmetry about ϕ_s=π remained. As can be seen in Figure 3.11, the difference between ϕ_s=3π/4 and 5π/4 are on the order of 1×10^{-15}, which is likely due to computational rounding errors. Thus, it is safe to say that symmetry in ϕ_s is maintained with the full BRDF, even when Model 2 is employed.

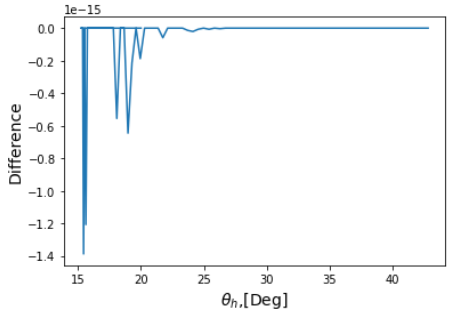

Figure 3.11: This plot shows the difference between the full BRDF (un-normalized) functions when θ_i and σ_g are kept constant at 40°, and 0.1 respectively and ϕ_s is varied from 3π/4 to 5π/4 (in radians). As one can see, the difference is minimal, on the order of $1 * 10^{-15}$, which is likely due to computational rounding error in the trigonometric functions.

3.4 Investigation of Anisotropic Models

Upon finishing the in-depth exploration of the isotropic BRDF models, the next step was to investigate trends in the anisotropic models, beginning with the an-

iostropic distribution function (Equation (3.2)).

For the anisotropic distribution function, there is both a θ_h and ϕ_h dependence, and the σ_g term has been replaced by m_x and m_y, to account for surface roughness varying differently in x and y. Here m=$\sigma_g\sqrt{2}$. When $m_x = m_y = m$, Equation (3.2) reduces to the form of Equation (2.1). While ϕ_i and θ_i were both kept constant in the isotropic case, ϕ_i and θ_i were allowed to vary in these simulations of the anisotropic distribution function. This is because ϕ_i becomes surface dependent, as one must align this parameter with the sample so that ϕ_h=0 at the specular peak. Several different instances of σ_x and σ_y were investigated, some of which where σ_x was significantly larger than σ_y, and vice versa (i.e. 0.1 vs 0.01) as well as cases where σ_x and σ_y were slightly larger than one another (i.e. 0.1 vs 0.09). When both θ_i and ϕ_i were kept constant (with ϕ_i=0), the peak occurred at θ_i=θ_s. However, depending on the value of ϕ_i, the specular peak occurred at various ϕ_s values. For example, when ϕ_i=0 or 360°, the peak occured at ϕ_s=180°. When ϕ_i=90°, the peak occurred at ϕ_s=270°, and when ϕ_i=270°, the peak occurred at ϕ_s=90°. The ϕ_i values resulted in a peak exactly 180° away in ϕ_s. This is due to the fact that the specular peak (where θ_h and ϕ_h are zero) is given by facets aligned with the macrosurface normal (with the distribution function peaking at this point). When ϕ_i is shifted, the location of the surface normal changes, causing ϕ_s to shift 180°. This is shown both analytically in Equation and in Figures 3.12-3.13.

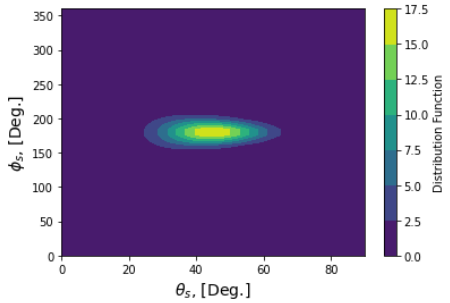

Figure 3.12: Contour plot illustrating how changing ϕ_i causes the peak in ϕ_s to shift. Shown for an example where θ_i=45°, σ_x=0.09 and σ_y=0.1, and ϕ_i=0°.

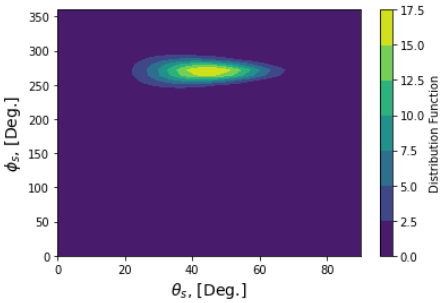

Figure 3.13: Contour plot illustrating how changing ϕ_i causes the peak in ϕ_s to shift. Shown for an example where θ_i=45°, σ_x=0.09 and σ_y=0.1, and ϕ_i=90°.

One can also vary θ_i and ϕ_i, allowing the surface to be struck by a cone of illumination as opposed to a single point source. When there is uniform illumination across θ_i (this is where θ_i forms a plane of illumination), the model predicts that there will be uniform reflection in θ_s at a plane of a specified ϕ_s. When there is uniform illumination across ϕ_i (illumination in a cone), the model predicts that two peaks will form at ϕ_s=90° and 270°, with a much smaller peak at ϕ_s=180 °. Overall, the model predicts that changing σ_x and σ_y only changes the width of the reflection (smaller σ results in a smaller peak, as with the isotropic model). Changing σ does not change the centers of the peaks, only changing ϕ_i and θ_i will change the center of the scattered radiation. Fig. 3.14-3.15 show the impact of varying either θ_i or ϕ_i, creating either a plane of uniform illumination in θ_i or a cone of illumination in ϕ_i.

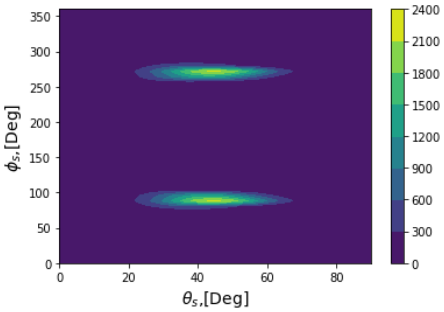

Figure 3.14: Contour plot illustrating how allowing either θ_i or ϕ_i to vary causes the location of the reflection peak to change. Shown for a case where σ_x=0.09 and σ_y=0.1. Case where ϕ_i is a cone of illumination from 0° to 360°, and θ_i=45°.

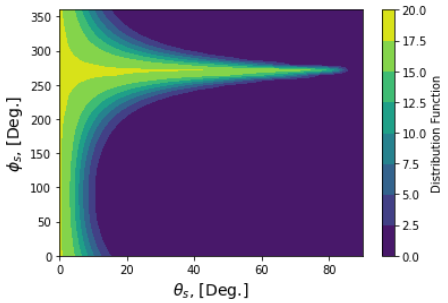

Figure 3.15: Contour plot illustrating how allowing either θ_i or ϕ_i to vary causes the location of the reflection peak to change. Shown for a case where σ_x=0.09 and σ_y=0.1. Case where ϕ_i=90°, and θ_i is allowed to vary.

As one can see in Figures 3.13-3.15, the peak of the distribution no longer necessarily occurs at $\phi_s = \pi$ radians. The peak remains centered about θ_i=θ_s, however, peaks now occur π radians from ϕ_i. This is due to the cosine and sine terms in the exponential of Equation (3.2), which result in the peaks shifting in ϕ_s.

Despite peaks no longer being centered strictly at $\phi_s = \pi$, behaviors and trends of the anisotropic model were investigated, with hopes of expanding upon the symmetry metric developed from the isotropic models. Thus, the next step was to investigate symmetries about the specular peak of θ_i=θ_s and ϕ_s=π. As with the isotropic case, there were asymmetries about θ_s. The center (which for isotropic models coincided with the peak) of the distribution function no longer necessarily occurred at θ_i=θ_s. The symmetry in ϕ_s is not maintained for the anisotropic case, either, as shown in Figure 3.16 below for the case where σ_x=0.1 and σ_y=0.01. Here θ_s is varied and illuminated by a cone of ϕ_i, and slices of ϕ_s have been taken. The largest value was expected to occur at $\phi_s = \pi$, which it does, but the slices at $\phi_s = \pi/2$ and $\phi_s = 3\pi/2$ are not equivalent, indicating a lack of symmetry in ϕ_s.

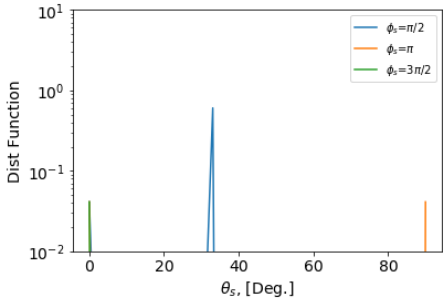

Figure 3.16: This plot shows various slices of ϕ_s at $\pi/2$, π and $3\pi/2$ (radians), for the case where θ_i=45°,σ_x=0.1 and σ_y=0.01, and ϕ_i is a cone of illumination. Symmetry is not maintained in ϕ_s as the distribution function values vary significantly for ϕ_s values that are equally spaced from ϕ_s=π.

While looking at the symmetry in ϕ_s proved to be a dead end for the anisotropic models, another approach was attempted to categorize materials as either isotropic or anisotropic. Looking at the form of Equations (2.1) and (3.2), one can divide out the normalization term, take the log of each equation and divide each equation by $-\tan^2(\theta_h)$ to get each equation in the form of Equations (3.10)&(3.11).

$$\frac{1}{2\sigma_g^2} \tag{3.10}$$

$$\frac{\cos^2(\phi_h)}{m_x^2} + \frac{\sin^2(\phi_h)}{m_y^2} \tag{3.11}$$

These equations appear to follow the familiar form of the circle equation and ellipse equations, where $(x-h)^2+(y-k)^2=r^2$ is the circle equation $x^2/a^2+y^2/b^2=1$ is the ellipse equation. Thus, the next step was to model various isotropic and anisotropic instances (dividing out the normalization term, tan term and taking the log) to attempt to simplify modeling BRDF based on σ_g or m_x and m_y values.

For the isotropic case, it was found that reducing the modeled data to the form of Equation (3.10) produced Figures 3.17-3.18. The line at y=5000 directly corresponds to $1/\sigma_g^2$ divided by 2, when σ_g=0.01. Reducing the anisotropic distribution function

to the form of Equation (3.11) produces Figure 3.17-3.18, where the maxima and minima of the plot directly correspond to $1/m_x^2/2$ and $1/m_y^2/2$, depending on if m_x or m_y is larger.

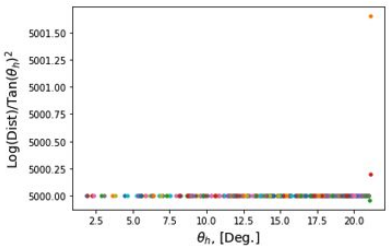

Figure 3.17: Isotropic Distribution Function in the form of Equation (3.10) when σ_g=0.01.

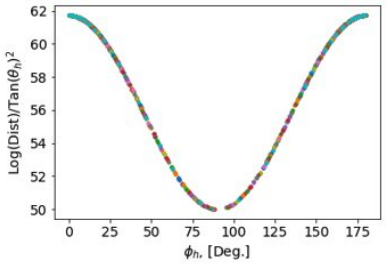

Figure 3.18: Anisotropic distribution function in the form of Equation (3.11), where m_x=0.09 and m_y=0.1

However, extending the to the full BRDF does not produce the same clean linear relationship for isotropic BRDFs (when plotted against θ_h) nor the same sinusoidal trend for anisotropic BRDFs (when plotted against ϕ_h). This is likely due to the inclusion of additional terms for the full BRDF, especially that of the Rayleigh Rice Polarization factor term. This term has several componets which distort the sinuosidal relationship between ϕ_h and Equation (3.11) and the linear relationship between θ_h and Equation (3.10). The linear relationship for isotropic BRDFs is only accurate for a small region close to the specular peak at θ_h=0. This is shown in Figures 3.19-3.20.

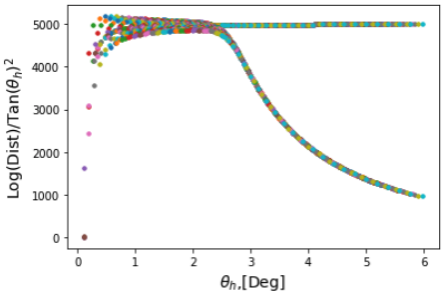

Figure 3.19: Log of Isotropic BRDF divided by $\tan(\theta_h)^2$ when σ_g=0.01.The straight line at y=5000 is the distribution function is the plot, and the curved line is the BRDF.

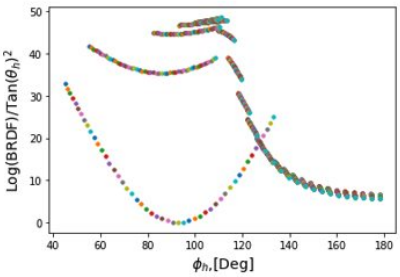

Figure 3.20: Log of Anisotropic BRDF divided by $\tan(\theta_h)^2$, where m_x=0.09 and m_y=0.1 The thinner line is the distribution function, and the thicker line is the BRDF.

Ultimately, while algebraic manipulation of Equation (2.1) and (3.2) were able to simplify modeling the distribution function, the addition of terms to extend to the full BRDF made this method of determining anisotropy infeasible. The hope was that when extended to the full BRDF, one would quickly observe if a plot of the log divided by the tan term versus θ_h would produce a linear plot indicating isotropy or if it would produce a sinusoidal plot when plotted against ϕ_h, indicating anisotropy. However, upon further consideration, this method would not be robust, failing for materials that fall between "perfectly isotropic" or "very anisotropic." Thus, this lack of robustness, paired with the non-physical results (see Figures 3.14-3.15) produced by the anisotropic distribution function, meant that the model was abandoned as a means of determining metrics for isotropy/anisotropy.

Instead, what was proposed and ultimately used for this study, was to build an algorithm that assess the degree of isotropy of each material. This was done as, firstly, the investigation of anisotropic models did not produce any fruitful metric for assessing a material's anisotropy. Secondly, the anisotropic models rely heavily upon align the sample adequately so that ϕ_i produces a ϕ_h=0. With experimental data, sample alignment is difficult to do (especially with more diffuse materials), and relying upon models that require precise alignment to judge anisotropy is not necessarily the best approach. Thus, the algorithm (which is detailed in Section 4.2), was developed with the intention of assessing deviation from isotropy in order to determine if an isotropic model can be used for the data set, or if other models should be used.

3.5 Fitting Routines in Direction Cosine Space

While algebraic manipulation of the distribution functions (in θ) did not yield clean results, it was found that transforming BRDFs to direction cosine space produced results that could distinguish isotropic from anisotropic surfaces. This is because the $\tan^2(\theta_h)$ term present in the distribution function can be directly correlated to direction cosine space terms $\Delta\alpha$ and $\Delta\beta$ through Equations (3.12)- (3.14).

$$\Delta\alpha = \sin(\theta_s)\sin(\phi_s - \pi) \tag{3.12}$$

$$\Delta\beta = \sin(\theta_s)\cos(\phi_s - \pi) - \sin(\theta_i) \tag{3.13}$$

$$\tan^2(\theta_h) = \frac{\Delta\alpha^2 + \Delta\beta^2}{\cos(\theta_i) + \cos(\theta_s)} \tag{3.14}$$

In fact, the isotropic distribution function is rotationally symmetric about the specular peak in direction cosine space. This symmetry is shown analytically in Equations (3.15)-(3.16), where $\Delta\alpha$ and $\Delta\beta$ are plugged into Equation (3.1) to evaluate

the rotational symmetry.

$$D(\Delta\alpha + b, \Delta\beta) - D(\Delta\alpha - b, \Delta\beta) = 0 \tag{3.15}$$

$$D(\Delta\alpha, \Delta\beta + b) - D(\Delta\alpha, \Delta\beta - b) = 0 \tag{3.16}$$

The diameter/angular spread of the BRDF remains constant as θ_i increases in direction cosine space. This is the case for in-plane data, when the second (cosine) term in Equation (3.13) is dropped. When out-of-plane data is incorporated, the isotropic distribution function remains symmetric in $\Delta\alpha$ space, but not in $\Delta\beta$ space. This is because the same change in θ_s space does not correspond to an equivalent change in $\Delta\beta$ space. The change in $\Delta\beta$ space is dependent upon θ_s as shown in Figure 3.21.

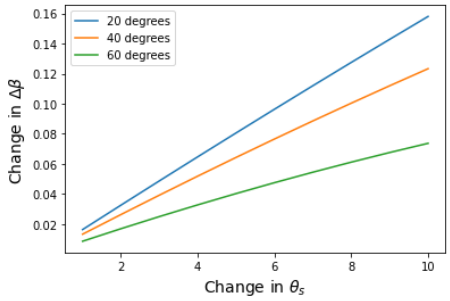

Figure 3.21: This plot shows how a change in θ_s is not the same across all θ_i in $\Delta\beta$ space. While the relationship between θ_s and $\Delta\beta$ is linear, the slope of these lines depends upon θ_s (which is represented by each line for θ_i= 20°, 40° and 60°).

Additionally, the overall diameter, semi-major and semi-minor axes of the BRDF decrease by a constant factor as θ_i increases when out-of-plane data is considered. The constant factor of decrease depends upon θ_s. To map the relationship between the diameter of the BRDF at θ_i=20° and 40°, one must determine the slopes of the lines in Figure 3.21. Dividing these slopes by one another, one can find the constant factor required to get the same diameter for each θ_i. This data has been included for the simulated data for both scaled and unscaled measurements of the diameter,

semi-major and semi-minor axes of the BRDF in direction cosine space.

Since this study dealt with out of plane data, the isotropic distribution function and BRDF were analyzed (using simulated data) in both the 3D Direction Cosine Space, and the 2D $\Delta\alpha$ space. Figures 3.22-3.23 illustrate the symmetry in $\Delta\alpha$ and how incorporating out of plane (ϕ_s) data breaks symmetry in $\Delta\beta$. The distribution function becomes more skewed in $\Delta\beta$ as σ_g increases, meaning that optically smoother surfaces produce more symmetric BRDFs in direction cosine space.

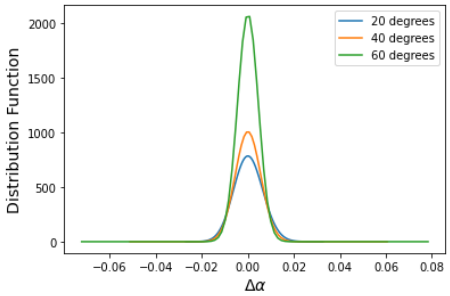

Figure 3.22: Isotropic Distribution function vs $\Delta\alpha$ a σ_g=0.005. θ_i is represented here by each of the different colored lines in the legend. Symmetry is maintained for $\Delta\alpha$. Note that the heights of the distribution function differ as θ_i changes, but the width in $\Delta\alpha$ remains constant.

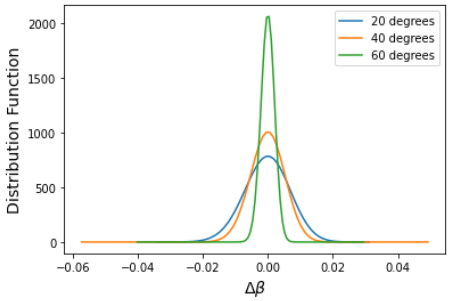

Figure 3.23: Isotropic distribution function vs $\Delta\beta.\theta_i$ is represented here by each of the different colored lines in the legend.

For Figure 3.22, it was found that the full width half maximum (FWHM) remained constant at $\Delta\alpha$=0.01, even as θ_i increased. This was not the case for Figure 3.23. When these plots were extended to the full BRDF, the asymmetry in $\Delta\beta$ was

exacerbated, however, the FWHM remained fairly constant (with a standard deviation of 0.002), with each measurement at each θ_i rounding to the $\Delta\alpha$=0.01 FWHM found for the distribution function.

While including out-of-plane data somewhat breaks the symmetry of these BRDF measurements, one way of measuring the "relative symmetry" is to look at how contours of BRDF change or remain constant in eccentricity. This was something that was investigated in addition to the previously mentioned diameter, semi-major and semi-minor axes of the BRDF in direction cosine space. The contour plot in Figure 3.24 shows how the eccentricity of each contour remains constant for isotropic data. The existence of "white space" in Figure 3.24 is due to the fixed spatial extent created by converting from spherical coordinates to direction cosine space. Were the plot for a θ_i=0°, there would be no white space, as it is a 1:1 conversion from spherical coordinates to direction cosine space.

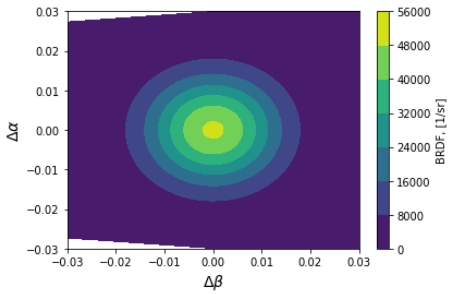

Figure 3.24: This plot shows how the eccentricity remains constant in direction cosine space for an isotropic BRDF with a σ_g=0.005 and θ_i=20°. The average eccentricity was 0.897±0.006 for this particular θ_i.

The eccentricity was determined (along with other parameters such as diameter, center of contours, and semi-major axis) by converting the image to pixel coordinate space. A series of image processing techniques was used to measure these parameters [24]. The image is then converted to a binary image using red, green and blue channels to extract each unique contour. An example of a binary image where the inner most contour has been detected is shown in Figure 3.25.

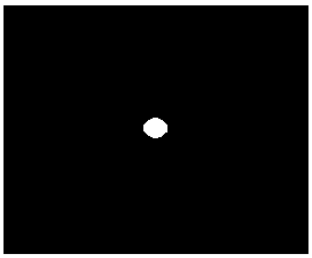

Figure 3.25: Binary image of the innermost contour, separated using a red filter. The red channel is used, as yellow (color of the innermost contour) is closest to red out of the three possible channels of red, green and blue.

For example, the innermost contours can be distinguished by using the red channel (as yellow is closest to red), while the outermost contours are distinguished by using the blue channel (referring to Figures 3.24-3.25), and the middle contours can be separated by the green channel. The image is then transformed using the Hough transform to determine the edges of each contour and attempts to fit ellipses to the edges detected [24]. From there, the algorithm estimates parameters such as the semi-major and semi-minor axes of each ellipse fit. The eccentricity is computed by dividing the semi-minor axis by the semi-major axis. Figure 3.26 shows the fit created from the binary image (Figure 3.25).

Figure 3.26: Ellipse fit to Figure 3.25. The algorithm detected an ellipse with an eccentricity of 0.83.

Table 3.1 below summarizes all of the data collected for the simulated isotropic BRDF data. The symmetry data about ϕ_s is not included as it was previously found

that the percentage difference of the simulated isotropic BRDFs was zero, when taking into accounting computational rounding error (see Section 3.3).

Table 3.1: Table summarizing various parameters for the simulated isotropic data collected at θ_i=20, 40 and 60° for a set σ_g=0.005. The diameter, semi-major and semi-minor (of the outermost contour) axes vary as θ_i increases, as out-of-plane information was taken into account. When the θ_i=40 and 60° measurements are scaled (ref. Chapter 2 for scaling factors), the standard deviation of these measurements drops significantly, signifying rotational symmetry.

Material	θ_i (Deg)	Mean Eccentricity	Scaled Major Axis (Pixels)	Scaled Minor Axis (Pixels)	Scaled Diameter (Pixels)	X Center (Pixels)	Y Center (Pixels)	FWHM ($\Delta\alpha$)
Sim Isotropic	20	0.89	168.06	150.21	130.95	132.98	114.34	0.012
Sim Isotropic	40	0.81	186.23	151.57	136.41	136.63	109.03	0.014
Sim Isotropic	60	0.82	174.65	143.22	136.41	136.63	108.50	0.011
Average		0.84	176.31	148.33	134.80	134.79	110.62	0.012
STD		0.04	9.20	4.48	3.35	1.82	3.23	0.002

While the semi-major axis, semi-minor axis and diameter vary as θ_i increases, other parameters in Table 3.1 remain relatively constant. This variation decreases when each is scaled by the factors determined from dividing the slope of each line by the θ_i= 20° line in Figure 3.21. For the 40° line, the scaling factor is 1.23, and for the 60° line, the scaling factor is 1.86. Part of this variation (for both the unscaled and scaled data) is due to including out-of-plane information, but some is also due to the fact that symmetry is broken by the Q factor, ρ_s and ρ_d terms in the BRDF equation (ref. Equation (3.3)). When including out-of-plane data, the low standard deviation of eccentricity acts as a stand-in for symmetry. This is because a higher (as well as more consistent) eccentricity (closer to 1) signifies that the BRDF changes at nearly the same rate in all directions, signifiying isotropy, whereas a less eccentric, as well as rapidly varying contour eccentricity denotes anisotropy. This metric works better for more specular materials, as it becomes the contours become larger, eventually trans-

forming into horizontal lines as σ_g increases (See Section 4.10 for plots). However, the standard deviation in eccentricity remains low, even as σ_g increases. Ideally, the eccentricity would be 1, but because the full BRDF introduces asymmetry in direction cosine space, the eccentricities recorded in the table are the new ideal. The x-center and y-center standard deviation terms in Table 3.1 also relate to this, as it means that the contours are being measured from the same point. If the eccentricity remained consistent, but the contours were measured from rapidly varying points, this would indicate anisotropy. The combination of the relatively constant eccentricity and constant x and y center coordinates indicates isotropy. The final term of Table 3.1, Full Width Half Maximum (FWHM) also indicates material isotropy. This is because a low standard deviation in this term means that the BRDF remains symmetric about $\Delta\alpha$ as θ_i changes. Referring to Figure 3.22, the distribution function remains relatively constant when plotted against $\Delta\alpha$. This is directly correlated to the rotational symmetry Harvey observed with in-plane data [21], as well as to the symmetry in ϕ_s observed in scatter space.

3.6 Beam Signature Data

Up until this point, the methodology development only included simulated data to determine what makes a material isotropic or anisotropic. As the intention of this study was to evaluate actual experimental data, the methodology needed to be tested on known isotropic sources. In order to test and validate the methodology developed, beam signature data was also analyzed. The beam signature is the Helium-Neon laser source which was used to illuminate all of the samples. The beam signature is merely the source, not reflecting off of any sample, which is then captured by the CCD. As the beam has not reflected off any surfaces, its radial symmetry is assumed to be representative of an isotropic sample. Any "anisotropies" (i.e. why the beam is not

perfectly round) captured are likely due to noise or from the off-axis parabolic mirror in the laser set-up. There is no spatial filter in the setup, so the beam is not exactly Gaussian. Figure 3.27 below shows a contour plot of the beam signature plotted in pixel coordinate space. A Gaussian filter with a σ=1 was applied to the image to filter out some of the noise associated with the data collected.

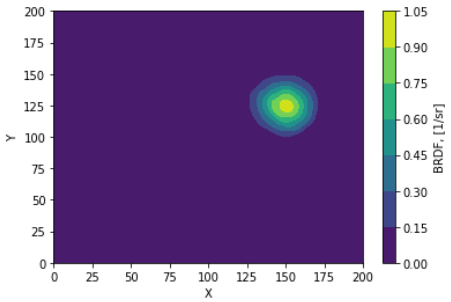

Figure 3.27: Contour plot of the beam signature in pixel coordinate space. A Gaussian filter with a σ of 1 was applied to this image. The scale on the plot is a relative BRDF, which was divided by the maximum value (thus, the maximum value here is 1).

At first glance, the beam signature appears relatively similar to the simulated isotropic BRDF in Figure 3.24. The contours appear to have a relatively high eccentricity, and the beam appears relatively symmetric. However, since the beam signature data is not a reflection (it is the CCD directly collecting on the beam), the data here is a simulation of the case where θ_i=θ_s=0°. Thus, in direction cosine space, $\Delta\beta$=0 when this is the case (ref. Equation (3.13)) and therefore all of the analysis was done in pixel coordinate space. Despite this difference, the beam signature data compared well with the simulated isotropic data. This is expected as Harvey states that the beam is symmetric in scalar wave optics theory [21]. Table 3.2 summarizes the beam signature's characteristics. The FWHM, diameter, and semi-major/semi-minor axis measurements here were ignored as the beam signature was only taken at one angle, and so those parameters do not serve as a useful metric of rotational symmetry here. Three separate measurements of the beam signature were collected and averaged in Table 3.2 below.

Table 3.2: Table summarizing the parameters measured for the beam signature. These measurements have been reported to help determine a baseline error in the data collected and the algorithm used to fit the data. The standard deviation represents the uncertainty in these measurements. Based upon the developed methodology, the beam signature is ruled as "solidly isotropic."

Material	Mean Dif Symm (%)	Min Dif Symm (%)	X Center (Pixels)	Y Center (Pixels)	Eccentricity	Classification
Beam Sig	9.11	6.90×10^{-5}	166.65 $\pm$1.00	53.86$\pm$2.25	0.73$\pm$0.04	Solidly Isotropic

Based on the metrics developed previously, the beam signature is ruled as solidly isotropic. Firstly, the beam signature exhibits significant symmetry about Y in pixel coordinate space (would translate to ϕ_s in scatter coordinate space). The mean percentage difference when the beam signature is folded in half about the center Y coordinate is 9.11%. The center coordinate was determined by indexing the maximum value of the BRDF, assuming that the beam was well-aligned with the CCD, and the maximum value occurred exactly at θ_s=0°. While the percentage difference in symmetry is higher than the 0% difference recorded for the simulated data, the simulated data also has no noise, and the laser passed through an off-axis parabolic mirror before being captured by the CCD. The off-axis mirror likely added some anisotropy to the data. However, this certainly serves as a good baseline for the experimental data to determine what consitutes "noise" or experimental uncertainty. The other parameters such as the mean eccentricity and x-center and y-center metrics also compare well to the simulated data. The eccentricity varies the same amount as the simulated data with a standard deviation of 0.04. However, with a perfectly Gaussian beam, the eccentricity should be 1. Thus, the difference of 0.27 serves as a measurement uncertainty here. The center of the ellipse measurements actually varies less than that of the simulated data, also indicating a higher degree of "isotropy." Thus, based upon all of the metrics, the beam signature has been classified by the algorithm as

"isotropic," and helps create a baseline for what constitutes isotropic data.

3.7 Baselines for Isotropicity

Table 3.3 below summarizes the baselines developed from both the simulated isotropic data and the beam signature data. The scaled diameter, X and Y center, and the FWHM metrics have been derived from the simulated data, as these measure how each of these parameters change with an increasing θ_i. The diameter and FWHM change in value as σ_g increases, but the standard deviation remains low for both of the parameters, which is why the standard deviation is used for these categories in lieu of the actual value. This is why the simulated data is used in this case opposed to the beam signature data. For each of these parameters, the lower the standard deviation, the more isotropic the sample is, as each parameter denotes rotational symmetry in direction cosine space. The eccentricity and mean symmetry baselines were derived from the beam signature. These baselines account for any noise in the experimental set-up, as some of the eccentricity measurements can be affected by Gaussian noise, as smoothing the noise further created contour plots of the beam signature with eccentricities closer to 1. This was not done in this study as a σ=1 (for the Gaussian filter) was applied, to ensure that the inherent variability was still captured. The mean symmetry metric also accounts for some of this noise, and thus the beam signature baseline was used in lieu of the simulated data.

Table 3.3: Table summarizing the various baselines for isotropicity developed from the simulated data and beam signature data. STD stands for standard deviation.

	Scaled Diameter (STD)	X/Y Center (STD)	FWHM (STD)	Eccentricity (Value + STD)	Mean Symm (% difference)
Baseline	3.35	3.23	0.002	0.73 ± 0.04	9.11

In Table 3.3 above, the STD "unit" indicates standard deviation. In this study,

each of these baselines were used to determine the isotropicity of each material. The closer each measured value was to the baseline, the more isotropic the material was considered. The results of such will be discussed further in Chapter 4.

3.8 Summary of Methodology

This section provides a summary of the methodology developed and a step-by-step list of the algorithm used for processing experimental data.

In this study, isotropic models were first investigated to develop a symmetry metric about ϕ_s in scatter coordinate space. This metric is the mean symmetry when the contour plot of the BRDF in scatter coordinate space is folded about ϕ_s=π, and the percentage difference that results between the points above π and below π. The second set of metrics was developed by converting plots to direction cosine space, resulting in measurements of the eccentricity, diameter, x-center, and y-center of the contours of BRDF in direction cosine space. A low standard deviation in these measurements indicates rotational symmetry in this space. The FWHM of the BRDF when plotted against $\Delta\alpha$ was also measured, to account for the asymmetry in $\Delta\beta$ when including out-of-plane data. Overall, six different metrics (x-center and y-center are counted as separate metrics), each with their own baselines were developed and determined to be used in the data processing section, discussed in Chapter 4. Below is a summary of the steps used to process data.

Steps for Processing Data for each measurement at a given θ_i

1. Apply Gaussian Filter with a σ=1.

2. Convert the data to a logarithmic plot by narrowing down CCD data to within 2 orders of magnitude below the peak value

3. Look at the symmetry about ϕ_s=π. Fold the data in half about this point and subtract the data below π (left-hand side) from the data above π (right-hand side),

dividing by the left-hand side to get a relative percentage difference.

4. Convert from scatter coordinate space to direction cosine space, and normalize the data by dividing all of the values by the maximum.

5. Plot the BRDF data against $\Delta\alpha$ and calculate the Full Width Half Maximum.

6. Convert the data to various binary images using red, green, and blue channels.

7. Apply the Hough transform to perform edge detection and use the algorithm to fit ellipses to these edges.

8. Collect and Record information on the semi-major axis, semi-minor axis, center, diameter and eccentricity of each measured ellipse. Scale 40° measurements by 1.23 and 60° measurements by 1.86 (as determined in Section 5 of this Chapter).

In the next chapter, these steps will be applied to five different samples to assess their isotropy/anisotropy.

IV. Results

4.1 Introduction

This section provides an in-depth discussion of the results of the algorithm described in the Methodology chapter. (A step-by-step version of this algorithm is shown in section 2 of this chapter). This algorithm was applied to five different materials of varying roughness and isotropy. The materials were at first qualitatively analyzed in terms of isotropy before applying the algorithm (shown in section 3). Maj Todd Small measured each of these samples using a Complete Angle Scatter Instrument (CASI) with a CCD. The samples were each illuminated by a Helium-Neon laser source (which was the beam signature sample described in Chapter 3). The samples were all rotated so that the beam illuminated the samples at θ_i=20°, 40° and 60°. The CCD was then able to capture data over a full hemisphere (capturing in-plane as well as out-of-plane measurements). The CCD has a resolution able to capture 0.001° per pixel. It also has a dynamic range able to capture six orders of magnitude, ensuring high fidelity experimental data. The algorithm was applied to each of these measurements, and was able to successfully classify four out of five of the materials. Applying this algorithm to actual data determined that the algorithm works well on specular data, but begins to decline in performance as BRDF drops. The conditions for which the algorithm will work were determined, as it fails to classify samples where the measured BRDF is below 100 1 sr^{-1}, or using the Beckmann distribution, cases where σ_g is greater than 0.1. The algorithm is able to classify specular materials by looking at data as opposed to attempting to fit to models to classify the data.

4.2 Algorithm

This section details the steps of the algorithm used to classify each material. The final results of this algorithm are shown in Section 10 in Table 4.34.

Given BRDF measurements of a material at a certain θ_i in scatter coordinate space:

1. Measure the mean symmetry about ϕ_s=π.

2. Convert to direction cosine space.

3. Measure the diameter, x and y center of each contour, the FWHM of the data against $\Delta\alpha$, and the eccentricity of each contour centered about the peak BRDF value.

4. Scale the FWHM and diameter measurements according to θ_i.

5. Combine all of the data for the material (for all θ_i), and find the standard deviations for scaled diameter, x/y center, FWHM and eccentricity.

6. Find the mean of the symmetry and eccentricity measurements.

7. Compare each of these parameters to the baseline (find percentage differences).

8. Weight each parameter by the appropriate factor.

7. Find final score and categorize as isotropic or anisotropic. Scores lower than 1 are highly isotropic, scores 1-10 lean isotropic, scores greater than 10 are anisotropic, and those greater than 30 are highly anisotropic.

4.3 Pixel Space to Scatter Coordinate Space Conversion

As the data was captured using a CCD, the BRDF measurements were each associated with an x and y value in pixel coordinate space. In order to determine symmetry in both scatter coordinate space and ultimately direction cosine space, a conversion was required between pixel space and scatter coordinate space. These conversions were determined by tracing a ray from a point on the sample to a pixel

on the CCD. Figure 4.1 is a 2D representation of the in-plane measurements.

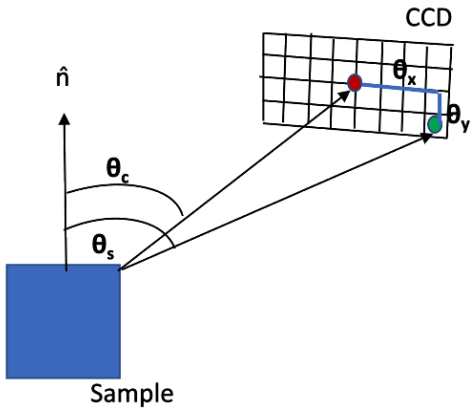

Figure 4.1: The blue square here represents the material surface, and θ_c, the angle between the center pixel (red dot) and the material surface normal, $\hat{n}$. θ_s, the angle between $\hat{n}$ and the target pixel (green dot) can be found using a series of trigonometric relationships if θ_x, θ_c and θ_y are known.

Referring to Figure 4.1, the calculation of the in-plane or θ_s direction is relatively straightforward. θ_c represents the angle between the surface normal, $\hat{n}$ and the center pixel (represented by a red dot in Figure 4.1), and is a known value as it is simply the detector arm angle. θ_x and θ_y are also known values, as they are the angles from the center pixel to the target pixel (green dot). Using these parameters, one can apply simple trigonometry to determine θ_s, using Equation (4.1) [25].

$$\theta_s = \theta_c + \sqrt{\theta_x^2 + \theta_y^2} \tag{4.1}$$

Calculation of the out-of-plane direction (ϕ_s) requires changing the orientation of the CCD. Figure 4.2 illustrates the out-of-plane (ϕ) information in 2D. Using this image as a guide, one can then determine ϕ_s.

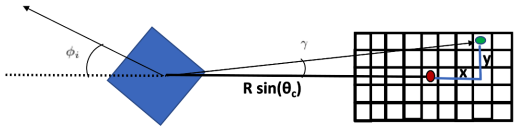

Figure 4.2: The blue square here represents the material surface, and ϕ_i was set to 0°. R sin(θ_c) was the distance from the sample to the center pixel (red dot). x and y were the horizontal and vertical pixel distances, respectively, from the center pixel to the target pixel (green dot). Using these, it was possible to calculate γ to ultimately find ϕ_s.

Figure 4.2 shows (as a 2D representation) how one can use the known values of ϕ_i, which was set to zero, R sin(θ_c), the distance from the sample to the center pixel (represented by a red dot), and x and y, the horizontal and vertical distances, respectively, from the center pixel to the target pixel (green dot) could be used to find γ. Equations (4.2)-(4.3) show how these values can be used to find ϕ_s [25].

$$\gamma = \tan^{-1} \frac{y}{x + R\sin(\theta_c)} \tag{4.2}$$

$$\phi_s = \phi_i + \pi + \gamma \tag{4.3}$$

Equations (4.1)-(4.3) were used in this study to convert pixel data to the scatter coordinate space, which will be the standard coordinate system for the BRDF data. All of the initial contour plots in scatter space were converted using these equations. It is worth noting that these conversions have created "white spaces" in each of these plots which are due to a fixed spatial extent translation. As θ_s increases, the range in ϕ_s decreases, creating the "white space" observed in some of the plots shown later. This same phenomenon is the reason why the θ_i=40° measurements span half the range in ϕ_s than the 20° measurements, and the 60° measurements half the range that the 40° measurements do.

4.4 Overview of Materials

This section provides an overview of all of the materials used in this study to produce BRDF data with both in-plane (θ) and out-of-plane (ϕ) information. Each of the materials are visually assessed to be either leaning isotropic or anisotropic. Throughout this chapter, these initial assessments will then be tested by the algorithm developed in Chapter 3 to determine how well the algorithm works.

4.4.1 Lab Mirror

The lab mirror sample was the first sample to be analyzed, and an image of the sample is shown in Figure 4.3. At first glance, it does not visually appear to have any features that would produce anisotropies. The surface does not appear to have any scratches or visible machine linings, overall appearing to be a very smooth surface. The sample is an aluminum coated surface that is highly specular, as evidenced by the reflection of the ceiling tiles present on the mirror. Overall, with these characteristics, it was determined that this sample is an isotropic surface.

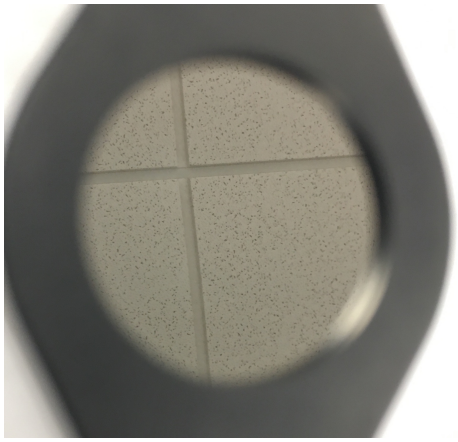

Figure 4.3: Image showing the mount and mirror used to generate BRDF data. The sample is a coated aluminum that is highly specular, as evidenced by the reflection of the ceiling tiles on the mirror. The sample appears quite smooth with no visible scratches or machine lines.

4.4.2 Kapton

Figure 4.4 below shows an image of the Kapton material used for this study. Overall, the Kapton material appears less reflective (and thus less specular) than the mirror, which is likely due to the fact that it is a semi-transparent thin film. Thus, more light is passing through the material and not being reflected by the surface. The material does not visually appear to have any machine linings that could would strongly favor anisotropic reflection, however, the sample does have a few scratches (some brighter spots on the material than in other locations). It is worth noting that if Kapton is not laid completely flat, it can impact the reflectance of the material. Thus, this sample was predicted to be lean isotropic.

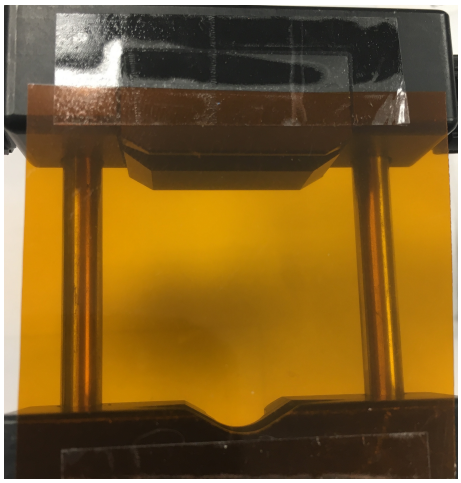

Figure 4.4: Image of the Kapton material (including the mount used to rotate the sample) used to collect out of plane BRDF data. The Kapton is a thin film that is semi-transparent. There appear to be a few scratches, or brighter spots on the sample.

4.4.3 Polished Alumnium

Figure 4.5 is an image of the polished aluminum sample used for this study. The sample is highly specular, as in the image, one can glimpse the reflection of the ceiling tiles on the sample (though not as specular as the mirror). Worth noting is the fact

that the sample has noticeable machine lines, which are the series of circular lines that appear in Figure 4.5. The presence of these circular machine lines indicates a high degree of material anisotropy, as the linings are not homogeneous across the sample, so the reflected beam will vary as the incident beam shifts on the sample. Thus, it was predicted that the machine lines should cause reflection to be distorted radially, and thus the algorithm should register this sample as anisotropic.

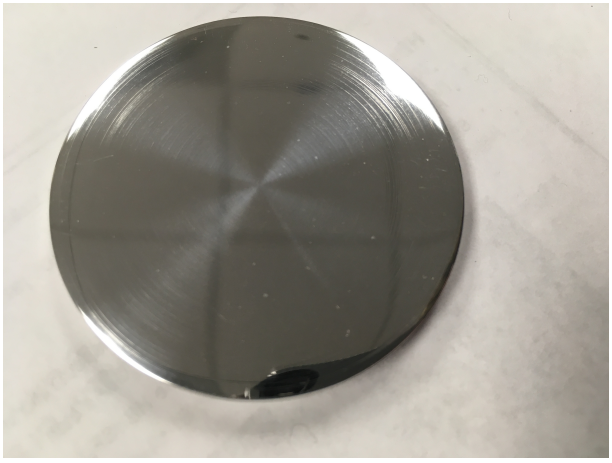

Figure 4.5: Image showing the polished aluminum sample used for this study. The sample is highly specular, as one can observe the reflection of the ceiling tiles on the sample. Additionally, the sample contains machine lining, as shown by the series of circular lines on the aluminum.

4.4.4 Solar Panel

Figure 4.6 shows an image of the solar panel material. The solar panel is highly reflective, as one can see partially see the camera used to capture the image in the picture. When illuminated, the beam was centered upon the sample, which does not include the green/orange components (in Figure 4.6) upon which the solar panel was mounted.

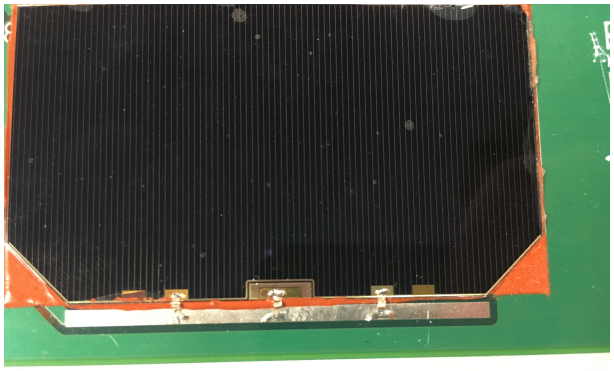

Figure 4.6: Solar panel used in this study. The solar panel is highly reflective, as one can partially see the camera used to capture this picture. Additionally, looking closely, one can observe a series of horizontal grid lines across the sample, which serve as conductors, as well as a series of elliptical scratches/marks on the panel.

The vertical grid lines in Figure (4.6) are conductive elements that run across the entire solar panel. These conductive elements are each about 1 mm wide. When the sample was illuminated, it was rotated 90° so that these "vertical" lines were actually horizontal. Another key aspect of the material is that there is a clear, glossy coating for the sample, and a layer beneath the coating that provides the overall black color of the sample. Overall, the surface is highly specular, as one can see their reflection in the sample. Beyond this, the sample appears to have a series of elliptical scratches/marks on the surface. The combination of the grid lines and these scratches, indicates that the solar panel surface should be highly anisotropic, perhaps more so than the polished aluminum sample. Thus, it was predicted that the algorithm should register this sample as highly anisotropic.

4.4.5 Metal Mesh

The metal mesh material was the final sample analyzed in this study. Figure 4.7 shows an image of the metal mesh along with the mount used to rotate the sample. The sample is a grid like metal that is highly transmissive, as one can see the table (on

which the sample was placed) through the sample. It was predicted that this sample should be registered as anisotropic, as the series of grid lines should cause reflected light to have a directional focus, rather than creating an isotropically reflected beam.

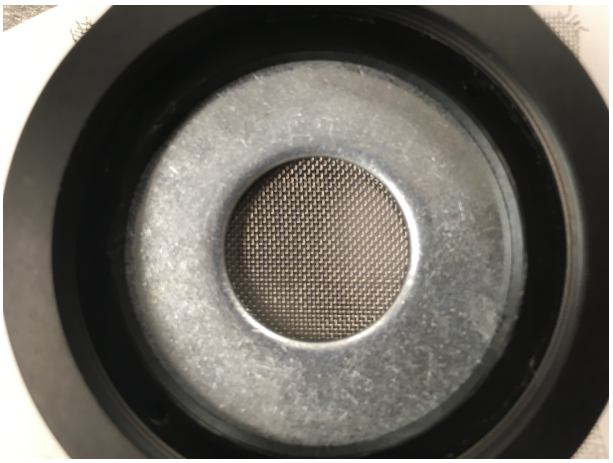

Figure 4.7: Image of the metal mesh material used to generate BRDF data. The mesh is highly transmissive and the series of grid lines should likely cause anisotropic reflection.

4.4.6 Summary

Table 4.1 summarizes all of the predictions for each of the materials based on visual inspection.

Table 4.1: Table summarizing predictions of degree of isotropy.

Material	Prediction
Lab Mirror	Isotropic
Kapton	Leans Isotropic
Polished Aluminum	Anisotropic
Solar Panel	Highly Anisotropic
Metal Mesh	Anisotropic

4.5 Lab Mirror Measurements

This section details the measurements taken of the Lab Mirror at θ_i=20°,40°, and 60° respectively, and discusses the results of the algorithm applied to this data set.

It should be noted that the uncertainty in alignment for this data set was 0.2°.

4.5.1 20° Measurements

The plot in Figure 4.8 shows the lab mirror sample at θ_i=20° in scatter coordinate space. The plot compares, at first glance, well to the simulated isotropic data where σ_g was small (< 0.01), as the simulated data also generated a "small circle" for the contour plots. Figure 4.8 also has some of the "white space" mentioned in section 2 of this chapter, which is due to the fixed spatial extent translation in ϕ_s with increasing θ_s.

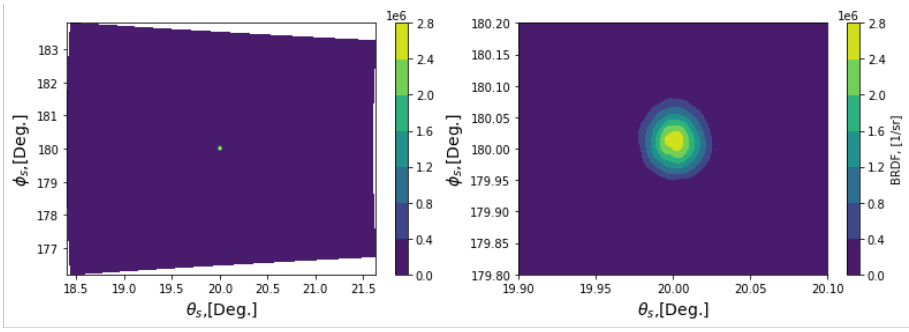

Figure 4.8: Contour plot (and a zoomed in plot) of the BRDF of the lab mirror illuminated at θ_i=20° in scatter coordinate space. The mirror appears to be highly specular and isotropic at first glance. This is because the sample appears very similar to the simulated data generated in scatter space, where a "small circle" was generated by the contour plots.

Converting this plot to direction cosine space (Figure 4.9), one can observe that the mirror sample continues to compare well to the simulated isotropic data. As noted with the signature beam, there is some noise present in the set-up, which makes for a not perfectly Gaussian beam signature, and some of the noise present in Figure 4.9, especially looking at the outermost contour. Overall, the lab mirror appears to consist of the neat series of similar eccentricity contours found in the simulated isotropic and beam signature data. As a note, the BRDF data has been converted to a relative scale (i.e. divided by the maximum value), and data has been narrowed down to two

orders of magnitude below the peak. The contours of each plot are set to occur in 0.5 increments on the log scale. This was done for each of the measurements for each material.

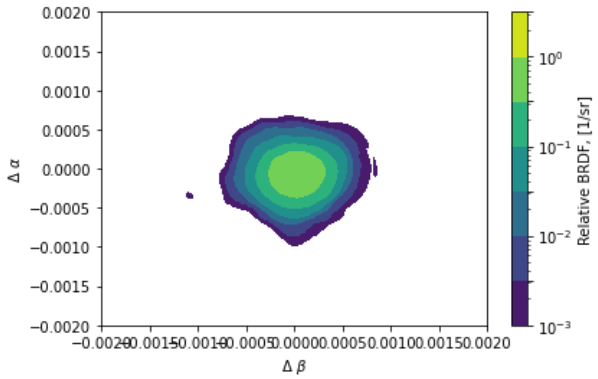

Figure 4.9: Plot of the lab mirror in direction cosine space for 20°. While the outermost contour is somewhat asymmetric, the plot appears to consist of ellipses of similar eccentricity, comparing well to the simulated isotropic and beam signature data.

Pulling the data for the inner and outermost contours of the lab mirror (Table 4.2), one can observe that the eccentricity is very similar (0.81 vs 0.80). Only these two contours are reported as some of the materials had quite a few (some up to 20) contours, and it was found that the innermost and outermost contours highlighted best how the material deviates from the baselines. These contour measurements are already less eccentric than the baseline e=0.73 (which accounts for noise, as a perfectly Gaussian beam should be e=1) reported for the beam signature, favoring a label of isotropy for this material.

Table 4.2: The eccentricity (Ecc.) of the inner and outer contours is of very similar eccentricity. This consistency in eccentricity is most similar to what was observed for the simulated data, with a lower eccentricity than the baseline measurement. In terms of the center x and y positions, the measurements are exactly the same for the x coordinate, shifted only slightly in y. Thus, this material so far exhibits the most consistency, similar to the simulated data.

Material	Angle (Deg)	Ecc.	Semi-Major Axis Scaled (Pixels)	Semi-Minor Axis Scaled (Pixels)	Diameter Scaled	X Center (Pixels)	Y Center (Pixels)
Lab Mirror (Outer)	20	0.81	70.66	57.43	63.13	134.43	111.04
Lab Mirror (Inner)	20	0.80	38.56	30.82	34.42	134.43	111.70

The table below (Table 4.3) further explores the characteristics of the 20° measurement for the Lab Mirror. The sample continues to match the simulated data, as the sample is just slightly less symmetric than the baseline measurement (10.21% vs 9.11% for the mean difference in symmetry), and the mean eccentric is less eccentric than the baseline and standard deviation of eccentricity is lower than the baseline, again indicating isotropy. As a note, when referring to the mean eccentricity, this is the measurement of all contours in Figure 4.9, not merely the innermost and outermost contours. The x and y center of these contours have also been recorded, and will be included in Table 4.8 in Section 1.4.

Table 4.3: The Lab Mirror has a mean percentage difference is slightly higher than that of the baseline set by the beam signature, indicating a strong degree of isotropy. The mean and standard deviation of the eccentricity are lower than the baselines, further indicating isotropy.

Material	Angle (Deg)	Max Dif Symmetry (%)	Min Dif Symmetry (%)	Mean Dif Symmetry (%)	Mean Eccentricity	STD Eccentricity	FWHM ($\Delta\alpha$)
Lab Mirror	20	1061.55	5.83×10^{-5}	10.21	0.80	0.01	0.02

4.5.2 40° Measurements

Figure 4.10 shows the measurement of the Lab Mirror at θ_i=40° in scatter coordinate space. The peak BRDF value increases here by a factor of 1.25, similar to how the simulated data saw an increase in BRDF with θ_i. The sample continues to "mirror" the simulated isotropic data in scatter coordinate space.

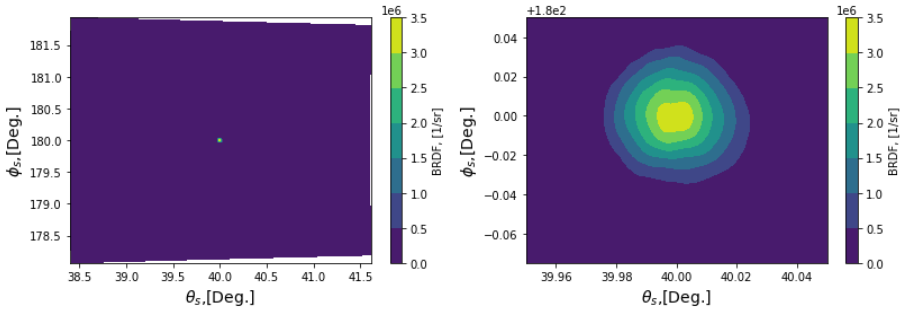

Figure 4.10: Contour plots (full range and zoomed plot) of the lab mirror BRDF in scatter coordinate space for 40°. The peak BRDF value here increases by 1.25 from the 20° peak, similar to how the BRDF of the simulated data increased with θ_i. The sample continues to "mirror" the simulated isotropic data in scatter coordinate space.

Upon converting this measurement to direction cosine space, one can observe that the plot (Figure 4.11) appears similar to the 20° measurement, although extending a smaller spatial extent in direction cosine space.

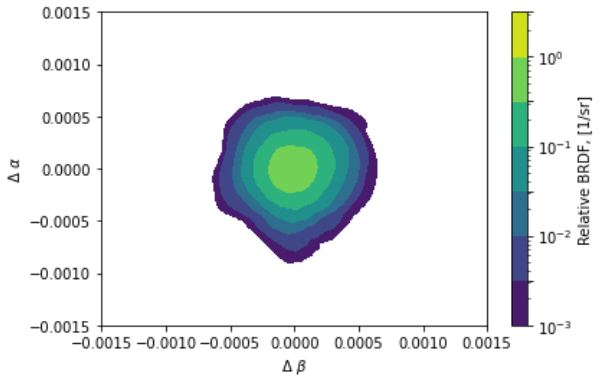

Figure 4.11: Plot of the lab mirror in direction cosine space for 40°. The plot appears similar to the 20° measurement, other than that it spans a smaller spatial extent in direction cosine space.

Table 4.4 shows the characteristics extracted from Figure 4.11 for the innermost and outermost contours. While the eccentricity varies slightly more between the inner and outer contours, the 40° measurement reports near-circular contours (much less eccentric than the baseline measurements) in comparison to the 20°, which indicates a high degree of isotropy. As observed in Figure 4.11, the diameter is smaller in direction cosine space than the 20°, although the semi-major axis and semi-minor axis are larger. The difference in diameter for the 40° compared to the 20° data (even when scaled) denotes that either this material is not fully isotropic, or that this diameter metric has some uncertainty not captured by the simulated data set.

Table 4.4: The inner and outer contours are nearly circular here (eccentricity (ecc.) close to 1), although there is slightly more variation between the inner and outer contour than the 20° measurement. Though the diameter is smaller, the semi-major axis is actually larger than 20° measurement. When scaled, the diameters vary greatly (for the outer contour) between the 20° and 40° measurements, which is a mark against labeling this material isotropic.

Material	Angle (Deg)	Ecc.	Semi-Major Axis Scaled (Pixels)	Semi-Minor Axis Scaled (Pixels)	Diameter Scaled	X Center (Pixels)	Y Center (Pixels)
Lab Mirror (Outer)	40	0.97	94.60	91.52	29.51	135.67	113.00
Lab Mirror (Inner)	40	0.95	36.09	34.28	35.12	133.37	108.50

The symmetry metric for 40° "redeems" this material as more isotropic (shown in Table 4.5), as the percentage differences for symmetry decrease for the mean, maximum and minimum. Part of this decrease in asymmetry is likely due to a smaller range in ϕ_s, as the mean symmetry reported here is actually lower than the baseline for the beam signature. The standard deviation in eccentricity for all contours remains the same as the 20° measurement (again lower than the baseline), another point in isotropy's favor. The mean eccentricity is also lower than the baseline of 0.73. The FWHM is close to half of the 20° measurement, which is expected due to the smaller range in ϕ_s.

Table 4.5: The symmetry increases at 40°, due to the lower percentage differences reported for all categories (max, min and mean). Part of this is likely due to the smaller range in ϕ_s, which likely also caused a decrease by about half for the FWHM. The standard deviation in eccentricity remains the same as the 20° measurement, despite the mean eccentricity becoming near circular.

Material	Angle (Deg)	Max Dif Symmetry (%)	Min Dif Symmetry (%)	Mean Dif Symmetry (%)	Mean Eccentricity	STD Eccentricity	FWHM ($\Delta\alpha$)
Lab Mirror	40	619.64	7.13×10^{-6}	7.55	0.96	0.01	0.009

4.5.3 60° Measurements

Figure 4.12 shows the 60° measurement in scatter coordinate space. The peak BRDF value continues to increase for increasing θ_i. The BRDF increases by a factor of 1.6, continuing the trend of increasing BRDF with increasing θ_i.

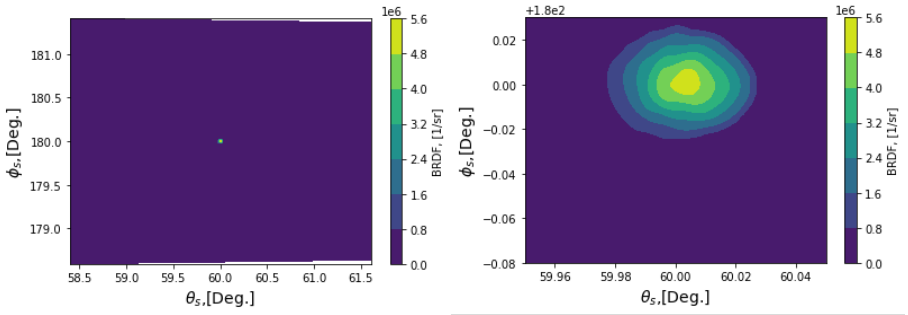

Figure 4.12: Contour plots (full plot and zoomed) of the lab mirror BRDF in scatter coordinate space for 60°. The peak BRDF value increases by a factor of 1.6 from the 40° measurement, continuing the trend of increasing BRDF with increasing θ_i.

Figure 4.13 shows a zoomed in version of Figure 4.12 in direction cosine space. The plot appears to narrow in $\Delta\beta$ in comparison to lower θ_i measurements for the mirror.

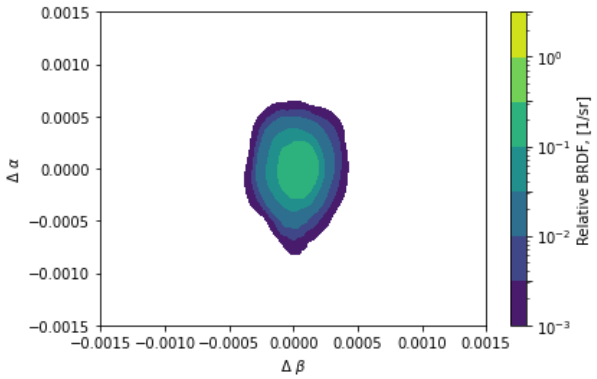

Figure 4.13: Plot of the lab mirror in direction cosine space for 60°. The plot narrows in $\Delta\beta$ in comparison to the 20° and 40° measurements.

Table 4.6 shows how the inner and outer contours of the direction cosine plot compare to the lower θ_i measurements. The eccentricity of both contours increases for both the inner and outer contour, recording measures of eccentricity slightly higher than the baseline. Additionally, the scaled semi-major axis and diameter increase from the 40° measurement. While scaled diameter is greater, it still differs significantly from the 20° measurement, and thus, the diameter parameter continues to indicate either that the material is not fully isotropic, or that there is some uncertainty not being captured in the diameter metric. As with the other lab mirror data, the center x and y coordinates continue to be consistent between the inner and outer contour.

Table 4.6: The scaled measurements (diameter, semi-major axis) are greater than those of the 40° measurements. The increase in scaled diameter does not match the 20° measurement closely though, serving as another "mark" against material isotropy. However, the eccentricity and center x and y positions between the inner and outer contours continue to be consistent, which is a "point" for isotropy.

Material	Angle (Deg)	Eccentricity	Semi-Major Axis Scaled (Pixels)	Semi-Minor Axis Scaled (Pixels)	Diameter Scaled	X Center (Pixels)	Y Center (Pixels)
Lab Mirror (Outer)	60	0.69	130.13	89.24	40.16	134.98	111.05
Lab Mirror (Inner)	60	0.71	39.66	28.35	33.44	134.93	109.00

Table 4.7 shows how the asymmetry increases slightly for the 60° measurement.

his is likely because the measurement becomes stretched in $\Delta\alpha$ somewhat, which corresponds to decreased symmetry in ϕ_s. However, this percentage difference is still rather comparable to the baseline (just slightly higher than the baseline of 9.11%). The standard deviation of eccentricity remains low (0.01), but the eccentricity now exceeds the baseline. However, the FWHM decreases by a factor of 3 (instead of 2) for the 60° compared to the 40° measurement. This is probably also due to the stretching in $\Delta\alpha$.

Table 4.7: The symmetry decreases for the 60° data compared to the 40°. This is likely because Figure 4.13 shows the plot stretching in $\Delta\alpha$. This is also probably why the FWHM decreases by a factor of 3 instead of the expected 2. However, the standard deviation of eccentricity continues to remain low (0.01), which is a mark of isotropy.

Material	Angle (Deg)	Max Dif Symmetry (%)	Min Dif Symmetry (%)	Mean Dif Symmetry (%)	Mean Eccentricity	STD Eccentricity	FWHM ($\Delta\alpha$)
Lab Mirror	60	973.69	7.64×10^{-6}	10.42	0.70	0.01	0.003

4.5.4 Summary of Mirror Data

Table 4.8 summarizes the data captured for the Lab Mirror. The symmetry is relatively high for this material, as the mean percentage difference is just above the 9.11% measured for the beam signature, indicating isotropy. The scaled diameter's standard deviation well exceeds the standard deviation of the baseline, which was set to 3.35, which indicates anisotropy. Harvey theorized that diameter should remain constant with increasing θ_i in direction cosine space. However, perhaps the reason why the diameter, even when scaled appropriately, did not remain constant for this sample (while remaining constant for the simulated data) is more so due to the contours picked by Python not being consistent rather than actual asymmetry in the data. The contour plots in direction cosine space only include the peak BRDF and any values two orders of magnitude below the peak. The cutoff metric could vary somewhat between

increasing θ_i, as the peak BRDF values are also changing. Thus, this likely makes measuring the diameter not the most accurate parameter for measuring isotropy. Another possible explanation for this is that there can be uncertainties associated with aligning the sample properly. For example, if the beam is not exactly centered on the sample, the spot size can elongate as θ_i increases, causing the diameter of the reflected beam to change as well. As a result of these two possible explanations, in the analysis section of this chapter, the diameter metric has been weighted lower in determining the overall isotropy and ranking of materials.

Despite the difference between the diameter baseline and the lab mirror standard devation, the lab mirror measured up fairly well against the rest of the baselines set in Chapter 3. When scaled, the FWHM is the most consistent out of all of the measured materials with a standard deviation of 0.005, just slightly higher than the baseline of 0.002. The x and y center coordinates also have very low standard deviations (the standard deviations are actually both lower than the baseline standard deviation of 3.23), which points further towards isotropy. These x and y centers are measurements of the centers of each contour measured (not just the innermost and outermost contours of each θ_i dataset in direction cosine space). The mean overall eccentricity is higher than the baseline of 0.73, although the standard deviation is somewhat higher than the baseline of 0.04. However, for each θ_i, the standard deviation remained consistently at 0.01 for the eccentricity, which also strongly indicates isotropy. The only point against this material being fully isotropic is the scaled diameter column, which, as noted previously, is likely a faulty metric. Otherwise, the algorithm identified the material as isotropic, matching up with the previous expectation that a smooth surface with no visible scratches or marks should reflect light isotropically.

Table 4.8: This material overall rates as leaning isotropic. This is because the standard deviations reported for the FWHM, eccentricity, x and y centers compare well to the baselines set by beam signature and simulated isotropic data. The symmetry is also high here as it is barely less symmetric than the beam signature data, which is the baseline. The only mark against this material is that the scaled diameter has a relatively high standard deviation.

Material	Mean Symmetry (% dif)	Scaled Diameter (Pixels)	Scaled FWHM ($\Delta\alpha$)	X Center (Pixels)	Y Center (Pixels)	Eccentricity	Classification
Lab Mirror	9.39 ± 1.60	44.27 ± 17.18	0.016 ± 0.005	134.42 ± 1.51	110.12 ± 1.60	0.81 ± 0.10	Isotropic

4.6 Kapton

This section details the measurements collected for the Kapton material at θ_i=20°, 40° and 60° respectively, and discusses the results of the algorithm applied to this dataset. The alignment uncertainty for this sample was 0.2°.

4.6.1 20° Measurements

Figure 4.14 shows the BRDF data in scatter coordinate space for θ_i=20°. As predicted, the Kapton is significantly less specular than the mirror sample, with a peak BRDF value 140 times less than that of the mirror sample.

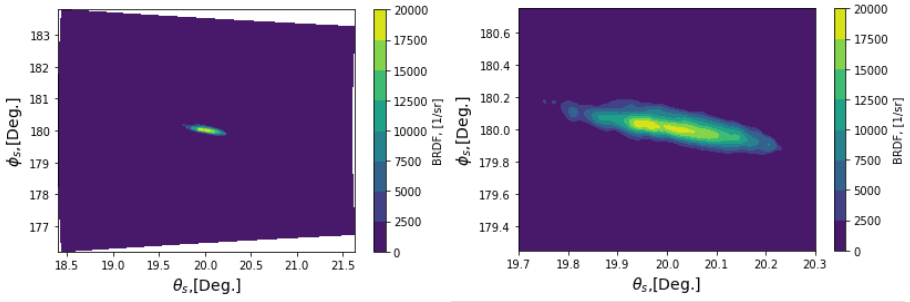

Figure 4.14: Plots (full plot and zoomed) of Kapton BRDF in scatter coordinate space for θ_i=20°. The peak BRDF value captured is 140 smaller than that of the mirror sample, meaning that Kapton is less reflective. The reflected beam also spans a much wider range in scatter coordinate space than the mirror sample, stretched unequally in θ_s and ϕ_s indicating possible anisotropy.

The reflected beam also spans a much wider range in scatter coordinate space, also meaning that the surface is less specular. However, the beam is also stretched unequally in θ_s and ϕ_s, which is a possible indicator of anisotropy. Figure 4.15 shows a zoomed in plot of the BRDF in direction cosine space, and further highlights this anisotropy. The white spaces in Figure 4.15 are likely just low signal, as any BRDF data two orders of magnitude below the peak does not appear in the plot.

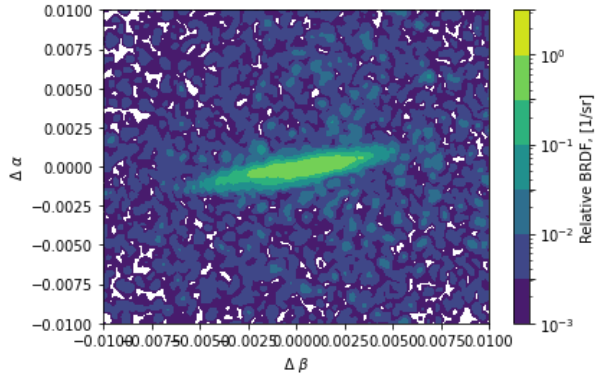

Figure 4.15: Plot of the relative BRDF of Kapton in direction cosine space. The zoomed in plot further illustrated anisotropy, as it is asymmetric in this space.

Table 4.9 captures the features extracted from the direction cosine plot. This table shows that Kapton is more eccentric than the mirror, and spans a much wider range in $\Delta\beta$, even though the mirror and Kapton were not plotted on the same scale. The x and y center points also appear to shift around more than the mirror center points. As a note, the direction cosine space plots were not plotted on the same scale as the mirror plots in order to use the ellipse fitting algorithm. Because the mirror data is more specular, the peak was smaller, and thus it had to be plotted on a smaller scale than the Kapton data in direction cosine space. Table 4.10 provides a better comparison point by looking at relative symmetry, standard deviation in eccentricity and the FWHM.

Table 4.9: Summary of the measurements of Kapton at θ_i=20°. The Kapton is much more eccentric than the mirror, spanning a much wider range in $\Delta\beta$.

Material	Angle (Deg)	Eccentricity	Semi-Major Axis Scaled (Pixels)	Semi-Minor Axis Scaled (Pixels)	Diameter Scaled	X Center (Pixels)	Y Center (Pixels)
Kapton (Outer)	20	0.25	159.06	39.79	60.98	131.11	110.61
Kapton (Inner)	20	0.15	77.25	11.70	29.73	138.27	110.34

Table 4.10: Summary of features extracted for Kapton at θ_i=20°. Using step 3 of the algorithm, Kapton is found to be less symmetric about ϕ_s than the mirror; this is not surprising given the stretching in scatter space. The mean eccentricity and standard deviation is higher than that of the mirror, indicating a higher degree of anisotropy.

Material	Angle (Deg)	Max Dif Symmetry (%)	Min Dif Symmetry (%)	Mean Dif Symmetry (%)	Mean Eccentricity	STD Eccentricity	FWHM ($\Delta\alpha$)
Kapton	20	36745.90	6.62×10^{-6}	318.44	0.19	0.06	0.029

Table 4.10 shows that Kapton is significantly less symmetric in ϕ_s than the mirror data. This is likely due to the fact that the Kapton data is stretched more in scatter space. The mean and standard deviation in the eccentricity of the Kapton is higher than the mirror data at θ_i=20°, indicating anisotropy.

4.6.2 40° Measurements

Figure 4.16 shows the 40° measurement of BRDF for Kapton in scatter coordinate space. The plot also has a higher peak BRDF value (1.4 times larger value), and appears to be stretched further in θ_s than the 20° Kapton data.

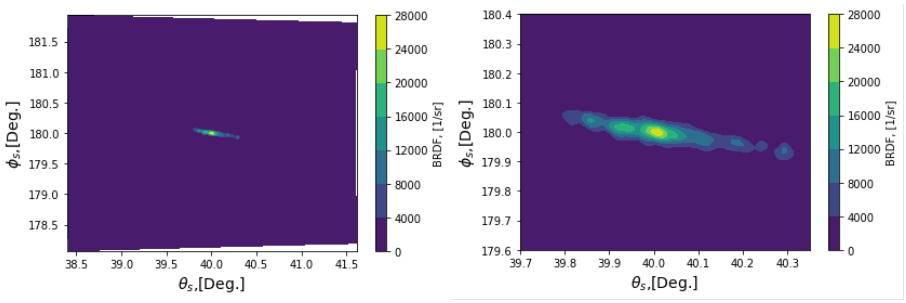

Figure 4.16: Plots (full plot and zoomed) of Kapton BRDF data for θ_i=40° in scatter coordinate space. The plot has a higher peak BRDF value than that of the 20° measurement, and appears to be stretched more in θ_s

Figure 4.17 shows the Kapton data in direction cosine space. It appears to closely resemble Figure 4.15.

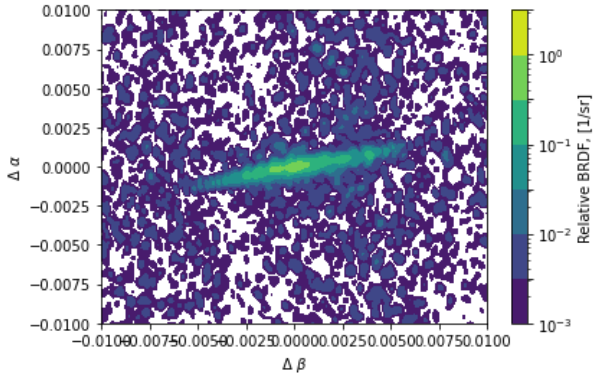

Figure 4.17: Plot of Kapton BRDF data for θ_i=40° in direction cosine space. The plot appears to closely resemble the 20° plot.

Table 4.11 summarizes some of the characteristics of inner and outer contours for the 40° measurement in direction cosine space.

Table 4.11: Measurements collected for the inner and outer contours at 40°. The 40° measurements extend a smaller space in direction cosine space as evidenced by the semi-major and semi-minor axis and diameter measurements (unscaled). When scaled, the semi-major axis is larger than the 20° measurement, as the outer contour is much more eccentric at 40°. The center x and center y coordinates for both the inner and outer contours also shifted somewhat compared to the 20° measurements.

Material	Angle (Deg)	Eccentricity	Semi-Major Axis Scaled (Pixels)	Semi-Minor Axis Scaled (Pixels)	Diameter Scaled	X Center (Pixels)	Y Center (Pixels)
Kapton (Outer)	40	0.14	164.60	22.50	36.39	141.01	108.31
Kapton (Inner)	40	0.21	37.15	7.88	16.13	132.47	109.04

The 40° measurements exhibit a higher degree of eccentricity (for the outer contour, less so for the inner contour). When the ellipse dimensions are scaled by 1.23, the semi-major axis is larger than the 20° measurement, however, all other dimensions remain smaller than the 20° measurements. The center x and y coordinates (for both the inner and outer contours) also shifted somewhat from the 20° measurements. Table 4.12 shows how the relative symmetry in ϕ_s changed for 40°, as well as the overall eccentricity measurements.

Table 4.12: Summary of symmetry data collected for 40°. The 40° measurements are less symmetric in ϕ_s despite extending a smaller range in ϕ_s. The 40° measurements vary less eccentricity-wise than the 20° measurements, however the outer contour is much more eccentric, indicating anisotropy. The FWHM is essentially half that of the 20° measurement, which is likely due to the 40° measurements extending half of the range in ϕ_s.

Material	Angle (Deg)	Max Dif Symmetry (%)	Min Dif Symmetry (%)	Mean Dif Symmetry (%)	Mean Eccentricity	STD Eccentricity	FWHM ($\Delta\alpha$)
Kapton	40	188102.70	2.25×10^{-5}	353.77	0.15	0.04	0.0096

The 40° measurements are less symmetric in ϕ_s than the 20° measurements, despite spanning half the range in ϕ_s. However, the FWHM is half of the measured FWHM for 20°, and this is likely due to the smaller range in ϕ_s translated to $\Delta\alpha$. The

40° measurement also has a lower standard deviation in eccentricity than that of the 20° measurement, but the outer contour is more eccentric than the 20° measurement, indicating anisotropy.

4.6.3 60° Measurements

Figure 4.18 shows the Kapton BRDF for θ_i=60° in scatter coordinate space. The peak BRDF value increases significantly here, increasing by a factor of 6.25 from the 40° measurement.

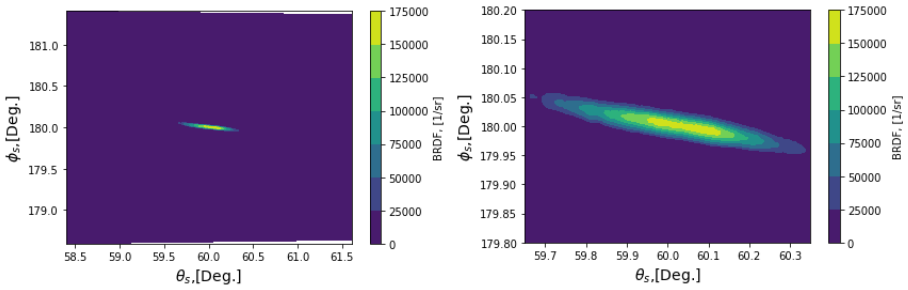

Figure 4.18: Plots (full plot and zoomed) of Kapton BRDF data for θ_i=60° in scatter coordinate space. The peak BRDF value increased by a factor of 6.25 compared to the 40○ plot.

When transformed to direction cosine space and zoomed in, the 60° plot appears to be more centered about (0,0) in direction cosine space compared to the 20° and 40° plots. The plot appears to have more white space than the previous direction cosine plots for Kapton. This is likely due to the fact that the BRDF is higher here at the specular peak than at the lower θ_i, and so the white space is BRDFs lower than 2 orders of magnitude below the peak, so this data is now cut from the plot, while it was included in previous plots.

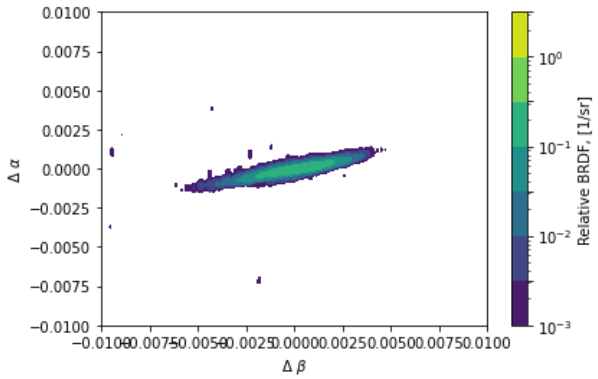

Figure 4.19: Plot of Kapton BRDF data for θ_i=60° in direction cosine space. The plot appears to be centered more about (0,0) in direction cosine space compared to the 20° and 40° plots.

Table 4.13 summarizes the data captured for the inner and outer contours at 60°. The 60° data is more eccentric than the previous θ_i measurements. This is because the semi-major axis measurement is much larger in comparison to the 20° and 40° measurements. Additionally, the outer contour is shifted somewhat in x. Overall, the eccentricity varies less between the inner and outer contours compared to the lower θ_i measurements (but a higher overall eccentricity). Despite this, the 60° measurements exhibit a lower degree of symmetry about ϕ_s, as shown in Table 4.14.

Table 4.13: Measurements of the inner and outer contours of the 60° plot in direction cosine space. The inner and outer contours are very similar in eccentricity, however, both are more eccentric than the 20° and 40° data. However, the semi-major axis is much larger when scaled than the lower θ_i measurements, as the plot is much more eccentric. The outer contour is also shifted somewhat in x compared to the previous measurements.

Material	Angle (Deg)	Eccentricity	Semi-Major Axis Scaled (Pixels)	Semi-Minor Axis Scaled (Pixels)	Diameter Scaled	X Center (Pixels)	Y Center (Pixels)
Kapton (Outer)	60	0.13	288.30	36.92	73.06	122.38	110.13
Kapton (Inner)	60	0.12	107.84	13.01	36.90	135.09	108.98

Table 4.14: Summary of data regarding the symmetry about ϕ_s for 60° as well as the standard deviation in eccentricity as well as the FWHM. The data is less symmetric than the previous θ_i measurements, and the FWHM is less than half of that of the 40° measurement, while varying slightly more in eccentricity.

Material	Angle (Deg)	Max Dif Symmetry (%)	Min Dif Symmetry (%)	Mean Dif Symmetry (%)	Mean Eccentricity	STD Eccentricity	FWHM ($\Delta\alpha$)
Kapton	60	424901.90	1.24×10^{-4}	759.28	0.15	0.05	0.0024

The 60° measurements also exhibit a FWHM that is less than half of that of the 40° measurement, despite the difference in ϕ_s only being half. The mean eccentricity and standard deviation is also slightly higher, indicating that the 60° measurement is more anisotropic.

4.6.4 Summary of Kapton Data

Overall, the Kapton exihibits little similarity to the mirror and simulated data, and appears to be quite anisotropic. The mean percentage difference in symmetry denotes that this sample is more than 50 times more asymmetric about ϕ_s, strongly favoring anisotropy. However, the standard deviation in the scaled diameter, as shown in Table 4.15, is of the same order of magnitude as the standard deviation for the lab mirror. This is likely again due more so to either alignment error or the inconsistency of contour levels, specifically the outermost contour, being measured. The peak BRDF values at each θ_i increased with θ_i, meaning that the contours were not necessarily set to the same levels, when taking into account the peak BRDF value and 2 orders of magnitude below. However, both the lab mirror and the Kapton samples would register as anisotropic via this metric, when compared to the baseline. The standard deviation in the FWHM is also high compared to the baseline, and the deviation is on the same order of magnitude as the mean FWHM, meaning that the FWHM varied significantly even when scaled for each θ_i. This is another mark in anisotropy's

favor. The deviations in x and y centers (of each contour, not just the inner and outer contours) were also above the baseline of 3.23, again indicating anisotropy. Finally, the mean eccentricity was significantly lower than the baseline eccentricity of 0.73, marking anisotropy. However, the standard deviation in eccentricity was actually lower than the lab mirror standard deviation and just above the baseline deviation, which indicates some degree of isotropy. With this, the sample has been labeled as moderately anisotropic, as shown in Table 4.15. In this case, the the algorithm identified the sample as being slightly more anisotropic than expected. The sample was observed to have a few scratches, which would cause some anisotropic reflection. It is possible that the beam was centered to illuminate one of these regions. Another possibility is that the Kapton sample was not laid completely flat, causing the reflection to appear more "anisotropic" than predicted.

Table 4.15: Kapton is more anisotropic than the mirror sample, as it well exceeds the baselines in mean symmetry and standard deviations in scaled FWHM, x and y center, scaled diameter. It also exceeds the baseline for mean eccentricity, while the standard deviation in eccentricity is actually less than that of the mirror. As a result, the sample has been labeled as moderately anisotropic.

Material	Mean Symmetry (% dif)	Scaled Diameter (Pixels)	Scaled FWHM ($\Delta\alpha$)	X Center (Pixels)	Y Center (Pixels)	Eccentricity	Classification
Kapton	477.16 ± 244.96	56.78 ± 18.74	0.019 ± 0.01 ±	136.49 8.07	107.36 ± 7.56	0.16 ± 0.05	Moderately Anisotropic

4.7 Polished Aluminum

This section details the measurements taken of the polished aluminum sample at 20°, 40° and 60° respectively, and shows the results of the algorithm applied the polished aluminum dataset. The alignment uncertainty was 0.2° for this sample.

4.7.1 20° Measurements

Compared to the samples previously discussed, the polished aluminum, at first glance, exhibits the most characteristics in common with the Kapton sample. This is evidenced by the plot shown in Figure 4.20 in scatter coordinate space for a θ_i=20°. The sample exhibits a specular peak, centered at θ_i=θ_s and ϕ_s=π radians. However, the polished aluminum is much more specular and reflective, as its peak BRDF value is twenty times that of the Kapton sample. This makes sense given that the Kapton is semi-transparent, and the polished aluminum is more mirror-like.

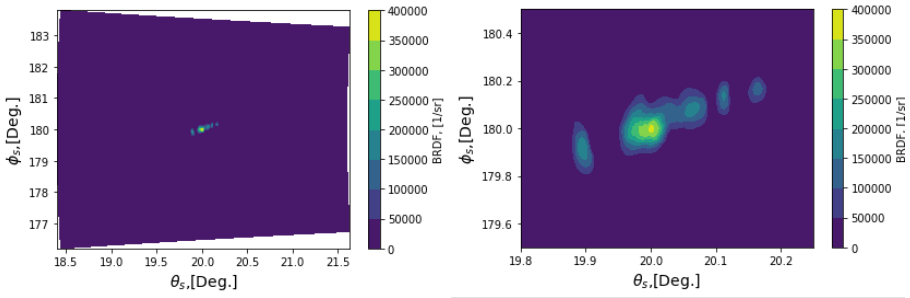

Figure 4.20: Plots (full plot and zoomed) showing the polished aluminum sample in scatter coordinate space for a θ_i of 20°. The sample has a peak BRDF that is twenty times that of the Kapton sample, although the BRDF appears to have a similar shape in scatter coordinate space.

As with the other samples, the polished aluminum BRDF data was converted to direction cosine space, and the peak of the data (plus two orders of magnitude below the peak) was zoomed in upon. Figure 4.21 shows the plot of the data in direction cosine space.

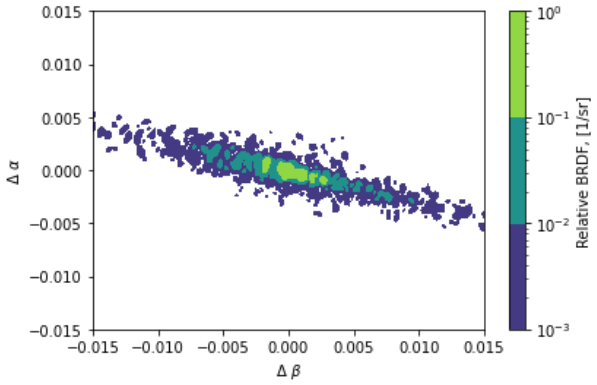

Figure 4.21: Plot showing the polished aluminum sample in direction cosine space. The sample spans a wider range in direction cosine space than the Kapton sample, but is stretched in $\Delta\beta$ compared to $\Delta\alpha$, indicating material anisotropy.

From Figure 4.21, it is evident that the plot is stretched in $\Delta\beta$ compared to $\Delta\alpha$, indicating some degree of material anisotropy. Another characteristic is that the plot spans a wider range in direction cosine space than the Kapton sample. To investigate this further, the parameters of the inner and outer contours of the sample in direction cosine space were pulled and shown in Table 4.16.

Table 4.16: Compared to the Kapton measurements at 20°, the polished aluminum exhibits a lower eccentricity, while also larger semi-major, semi-minor axes and diameters for the outer contour. The inner contour is much smaller in comparison, and is shifted significantly from the center of the outer contour. The scaled columns are scaled by 1 here.

Material	Angle (Deg)	Eccentricity	Semi-Major Axis Scaled (Pixels)	Semi-Minor Axis Scaled (Pixels)	Diameter Scaled	X Center (Pixels)	Y Center (Pixels)
Polished Aluminum (Outer)	20	0.35	311.71	109.87	174.06	119.37	171.01
Polished Aluminum (Inner)	20	0.46	18.18	8.38	11.99	135.22	109.66

Table 4.16 differs from the Kapton sample at 20° in that the sample spans a much wider range in pixel coordinate space (higher semi-major and semi-minor axis and

diameter for the outer contour). The inner most contour is much narrower, indicating that the reflection is more spread out in scatter space instead of narrowly concentrated at the peak. However, the eccentricity is quite high here (compared to the baseline), indicating anisotropy. Table 4.17 below discusses the symmetry of the sample as well as the consistency of eccentricity and FWHM.

Table 4.17: Compared to the Kapton measurements at 20°, the polished aluminum exhibits a lower degree of symmetry in ϕ_s (looking at the max, min and mean symmetry columns) as the percentage differences are all higher for polished aluminum. The polished aluminum is overall less eccentric, and exhibits a similar standard deviation and FWHM to the Kapton.

Material	Angle (Deg)	Max Dif Symmetry (%)	Min Dif Symmetry (%)	Mean Dif Symmetry (%)	Mean Eccentricity	STD Eccentricity	FWHM ($\Delta\alpha$)
Polished Aluminum	20	116529.90	3.26×10^{-5}	532.83	0.41	0.06	0.025

Table 4.17 shows that the polished aluminum sample is less symmetric in ϕ_s than the Kapton when comparing the mean, maximum and minimum percentage differences, indicating anisotropy. The standard deviation of eccentricity for all measured contours (though less eccentric than the Kapton) is comparable to the Kapton sample, along with the FWHM. The mean eccentricity of all contours is high is comparison to the baseline, favoring anisotropy.

4.7.2 40° Measurements

Figure 4.22 shows the 40° measurements of the polished aluminum sample in scatter coordinate space. The peak BRDF value also increases by a factor of 1.2, which is slightly less than the factor the Kapton increased by, but similar to the factor that the mirror sample increased by. This is likely due to the fact that both samples are made out of aluminum, and thus the index of refraction is similar, creating a similar increase as θ_i changes.

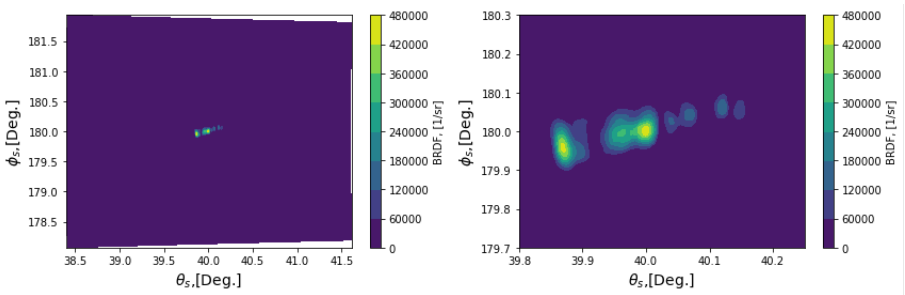

Figure 4.22: Contour Plots (full plot and zoomed) of the BRDF of the polished aluminum sample illuminated at θ_i=40° in scatter coordinate space. The peak BRDF value also increases by a factor of 1.2 (smaller than the increase for the Kapton at 40°, but similar the increase for the mirror sample).

Figure 4.23 shows how the 40° measurement compares to the 20° measurement in direction cosine space. At first glance, the plot appears to be a "shrunken" down version of the 20° measurement.

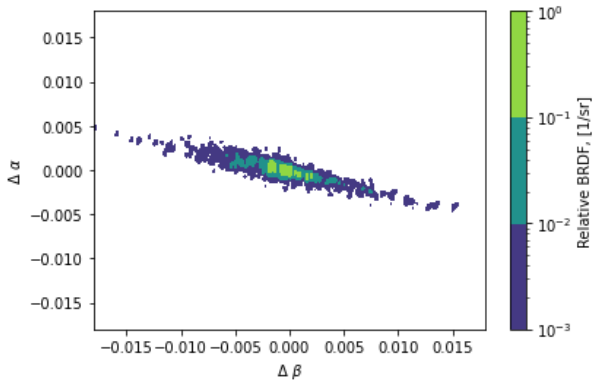

Figure 4.23: Plot showing the polished aluminum sample at 40° in direction cosine space. The plot appears to be a "shrunken" down version spatially of Figure 4.21.

Table 4.18 shows the characteristics of the inner and outer contours of the sample at 40°, verifying that the sample does indeed span a smaller range in direction cosine space (for the unscaled measurements). However, when the sample is scaled, the semi-major axis becomes larger than the 20° measurement, while all other parameters (semi-minor axis and diameter) remained smaller when scaled. As a result, the outer contour of the 40° measurement is much more eccentric than that of the 20°, indicating increased anisotropy. Another point of interest is that inner contour shrinks as well

(even when scaled) from the 20° measurement, while the center x and y coordinates remain more consistent.

Table 4.18: The outer contour of the 40° measurement is much more eccentric than that of the 20° measurement. When scaled, the semi-major axis measurement is larger, while the diameter and semi-minor axis remain smaller. The scaled inner contour also becomes smaller than that of the 20° measurement, while the center x and y measurements are more consistent between the inner and outer contour compared to the 20° data.

Material	Angle (Deg)	Eccentricity	Semi-Major Axis Scaled (Pixels)	Semi-Minor Axis Scaled (Pixels)	Diameter Scaled	X Center (Pixels)	Y Center (Pixels)
Polished Aluminum (Outer)	40	0.14	322.22	43.25	98.52	117.49	107.72
Polished Aluminum (Inner)	40	0.49	16.90	8.25	11.28	130.95	108.56

Given the higher eccentricity of the outer contour (and the greater difference in eccentricity of the inner and contours), it was suspected that the 40° sample would have a higher degree of asymmetry in ϕ_s. Table 4.19 shows that the 40° is indeed slightly less symmetric in ϕ_s. However, interestingly the high standard deviation (paired with the high mean eccentricity of all contours) of eccentricity (0.15) demarcates strong anisotropy for this sample compared to the 20° data. The mean eccentricity increases as expected from the 20° data. The FWHM is half that of the 20° measurement, a result expected for a more isotropic material.

Table 4.19: The asymmetry for the 40° measurement is slightly higher than that of the 20°. Noticeably, the material exhibits a high standard deviation of eccentricity, which demarcates strong anisotropy. The FWHM is half that of the 20° measurement, which is a result expected for a more isotropic material.

Material	Angle (Deg)	Max Dif Symmetry (%)	Min Dif Symmetry (%)	Mean Dif Symmetry (%)	Mean Eccentricity	STD Eccentricity	FWHM ($\Delta\alpha$)
Polished Aluminum	40	145605.80	6.96×10^{-4}	535.03	0.35	0.15	0.01

4.7.3 60° Measurements

Figure 4.24 shows the polished aluminum BRDF captured at θ_i=60° in scatter coordinate space. The peak BRDF value here increased by a factor of 3.3 from the 40°, which differs from the Kapton data, where the peak BRDF value increased by 6.25, and from the mirror data where it increased by 1.6 at 60° from the 40° measurement.

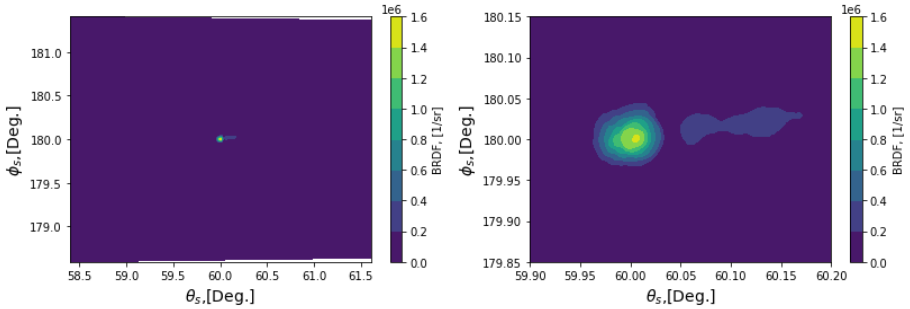

Figure 4.24: Plots (full plot and zoomed) showing the polished aluminum sample illuminated at θ_i=60° in scatter coordinate space. The peak BRDF value also increases by a factor of 3.3, which differs from the Kapton and mirror data where the peak BRDF value increased by 6.25 and 1.6 respectively 60° from the 40° measurement.

Figure 4.24 also appears to have a sharper peak than the previous measurements, and this peak is slightly shifted off of θ_i=θ_s. This may be due to an alignment issue, as the uncertainty in alignment is 0.2°. There appears to be a tail to the data. Zooming in on this peak in direction cosine space (Figure 4.25), one can observe that this is not the case, and the plot maintains the same elliptical shape stretched unequally in

$\Delta\alpha$ and $\Delta\beta$. However, the plot in direction cosine space does span a lower spatial range than the previous polished aluminum measurements.

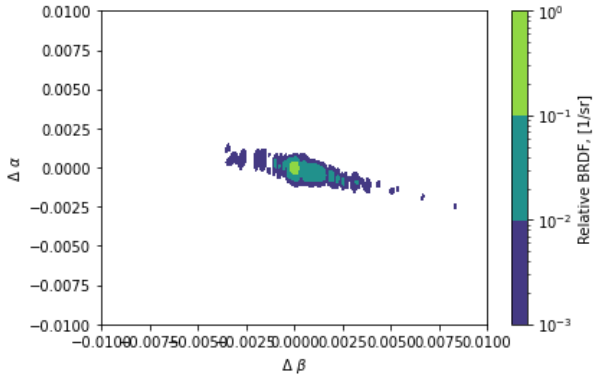

Figure 4.25: Plot showing the polished aluminum sample in direction cosine space for 60°. The measurement maintain the same asymmetric stretching in direction cosine space, but spans a lower spatial extent than the data at lower θ_i.

Table 4.20 shows characteristics of the inner and outer contours of Figure 4.25. The inner contour is significantly less eccentric in comparison to the 40° inner contour. When scaled by 1.86, each of the contours is also smaller than that of the 40°, meaning that the plot occupies a much smaller region in direction cosine space. The BRDF becomes more narrowly focused at 60°. There is also less variation in the x and y center points. However, since the eccentricity between the inner and outer contour varies significantly, the BRDF has become more directionally focused in $\Delta\beta$ as opposed to $\Delta\alpha$, which one can observe by looking at Figure 4.25. Such directional focusing is an indicator of anisotropy.

Table 4.20: The inner contour is significantly less eccentric compared to the 40° case. This means that the difference between the inner and outer contours is also greater. This indicates that the BRDF has skewed significantly in the $\Delta\beta$ direction compared to previous measurements of the polished aluminum. Likely this means that at higher θ_i, directional reflection strongly favors the x direction as opposed to the y direction.

Material	Angle (Deg)	Eccentricity	Semi-Major Axis Scaled (Pixels)	Semi-Minor Axis Scaled (Pixels)	Diameter Scaled	X Center (Pixels)	Y Center (Pixels)
Polished Aluminum (Outer)	60	0.28	139.35	39.17	65.53	149.92	113.14
Polished Aluminum (Inner)	60	0.79	10.53	8.28	9.15	135.58	108.84

Table 4.21 denotes the symmetry of this material at 60°, as well the standard deviation in eccentricity (which was already noted to be high looking at the inner and outer contours), and the FWHM. The eccentricity has a standard deviation of 0.23, which is the highest standard deviation observed so far. However, the mean eccentricity decreased from the previous measurements, which was unexpected. The measured eccentricity is still higher than the baseline, indicating anisotropy. It is possible that the alignment issue noted in Figure 4.24 may be causing the beam to become less eccentric, especially if the same spot is not being illuminated. The direction cosine plot is found to be more symmetric about ϕ_s, however, this is likely due to the smaller extent of the 60° measurement in ϕ_s, as well as the strong directional skewing (observed in $\Delta\beta$) towards the θ_s. The FWHM is less than half that of the 40° measurement, which is further evidence of directional skewing.

Table 4.21: The data below indicates strong directional skewing at 60°. This is because of the very high standard deviation in eccentricity and the FWHM which is less than half of the 40° measurement. The symmetry in ϕ_s also suggests this, as there is significantly less asymmetry for 60∘ that cannot be merely accounted for by the smaller range in ϕ_s at 60°.

Material	Angle (Deg)	Max Dif Symmetry (%)	Min Dif Symmetry (%)	Mean Dif Symmetry (%)	Mean Eccentricity	STD Eccentricity	FWHM ($\Delta\alpha$)
Polished Aluminum	60	62875.35	2.75×10^{-5}	195.10	0.63	0.23	0.004

4.7.4 Summary of Polished Aluminum Data

Referring to Table 4.22, the polished aluminum has a higher standard deviation for all categories with the exception of the mean symmetry and FWHM columns than the Kapton sample. The diameter, even when scaled, has a standard deviation that is half of the mean. With the simulated isotropic sample, this standard deviation was 2% of the mean. Ignoring the lower standard deviation for the mean symmetry, the percentage difference in symmetry (421% vs 477%) was still significant and comparable to the asymmetry in Kapton. Arguably, there was stronger directional skewing in the polished aluminum, which is evidenced by the high standard deviation of eccentricity, despite actually registering a mean eccentricity that was lower. Another point favoring anisotropy of this material is the standard deviations of the x and y centers which are both at least six times that of the baseline standard deviation. Thus, the polished aluminum sample rates as more anisotropic than the Kapton sample. This result matched predictions, as the visible machine lines on the surface caused one to theorize that this would create anisotropic reflection.

Table 4.22: The polished aluminum sample is rated as more anisotropic than the Kapton sample. This is because for nearly all categories (excluding the mean symmetry and FWHM), the standard deviation is significantly higher. The standard deviation for the diameter is half that of the mean, which is significant, compared to the standard deviation that was 3% of the mean for the simulated isotropic material. The x and y center (of every contour, not just the inner and outer contours for each θ_i) shifts around much more, and the eccentricity has a high standard deviation, indicating strong directional skewing (in x). Despite the polished aluminum reporting a higher symmetry, the 421% vs the 477% reported for Kapton, is still similar enough (especially taking into account the standard deviation), that the polished aluminum renders as more anisotropic than the Kapton sample.

Material	Mean Symmetry (% dif)	Scaled Diameter (Pixels)	Scaled FWHM ($\Delta\alpha$)	X Center (Pixels)	Y Center (Pixels)	Eccentricity	Classification
Polished Aluminum	420.99 ± 195.63	112.70 ± 55.64	0.022 ± 0.006	134.85 ± 48.89	119.97 ± 20.13	0.46 ± 0.19	Anisotropic

4.8 Solar Panel

Measurements of the solar panel were collected at 20°,40°, and 60°, respectively. The results of these measurements are expounded upon below. The alignment uncertainty for the solar panel data was 0.2°.

4.8.1 20° Measurements

Figure 4.26 shows the extent of the CCD image captured in scatter coordinate space for a measurement of the solar panel when illuminated at θ_i=20°. The solar panel is less specularthan all of the materials enumerated so far, excepting the Kapton sample, as it records the second lowest BRDF so far.

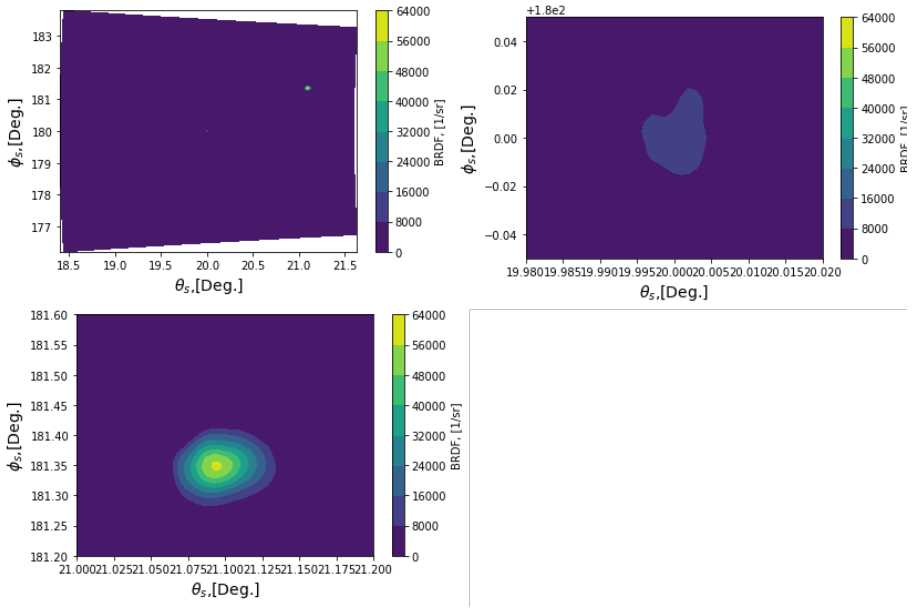

Figure 4.26: Contour plots of the BRDF captured in scatter coordinated space when illuminated at θ_i=20°. There are 2 peaks here, one centered at the specular peak and another (where the maximum value is located) occurring off of the specular peak at θ_s=21.09° and ϕ_s=181.35°. The first peak is to the right of the full plot, and the second peak zoomed in is below the full plot.

Unlike with the previous materials, the solar panel BRDF is split into two peaks, one located directly at θ_i=θ_s and ϕ_s=180° (Peak 1), and another at θ_s=21.09° and ϕ_s=181.35° (Peak 2), where the maximum BRDF value is located. Since the alignment uncertainty is 0.2°, this second peak is most likely not the main specular peak. These two peaks are likely caused by reflections from the two surfaces on the solar panel. Since there is both a glossy coating and layer beneath this coating, it is likely that light is reflecting from both surfaces, which are not parallel to one another and generating two separate peaks. Upon zooming in on the first peak, there is also a diffraction pattern about the peak, as shown in Figure 4.27. This diffraction pattern is likely due to the vertical grid lines mentioned in Section 4.4.4. In scatter coordinate space, the spacing between each peak extends about 0.1° in ϕ_s (looking at Figure 4.27. One can use Fraunhofer diffraction [26] through a rectangular aperture to find the periodicity of the feature creating the diffraction pattern. This is equation is Δx=2λ

z/l. where λ is the wavelength of the HeNe laser, 632.8 nm, z is the distance from the sample to the CCD of 0.325 m, and l is the aperture width of 1mm. Using these parameters and converting to angular coordinates, one will calculate a Δx=0.07°, which compares closely to the spacing of roughly 0.1° in Figure 4.27. Thus, one can conclude that the grid lines are causing the diffraction pattern.

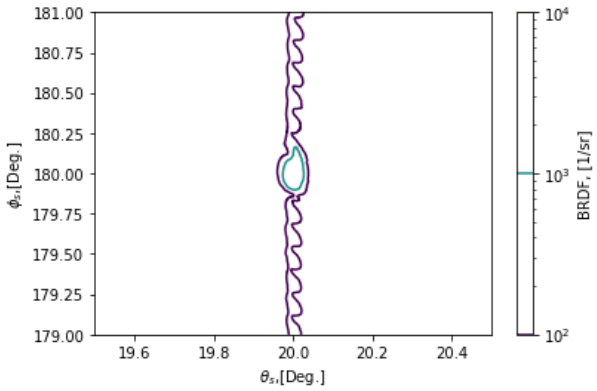

Figure 4.27: Zoomed in version of Peak 1 in scatter space. The colorbar here uses a log scale to show the peak value and data two orders of magnitude below the peak. By zooming in on the data, one can observe the diffraction pattern created by the grid lines.

In order to perform data analysis in the direction cosine space and capture relevant information about eccentricity, semi-major and semi-minor axes and diameter, the CCD data was split into Peak 1 and Peak 2 data and converted to direction cosine space, as shown in Figures (4.28)-(4.29).

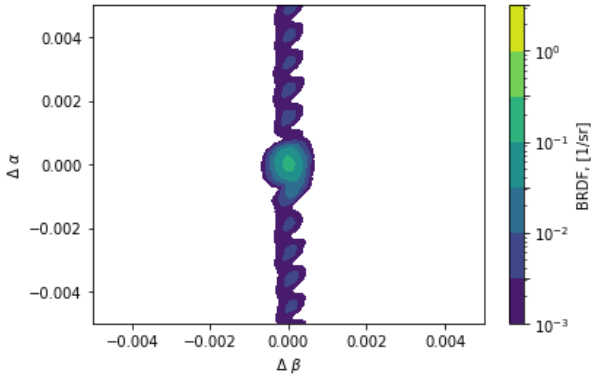

Figure 4.28: Peak 1 showing the diffraction pattern in direction cosine space.

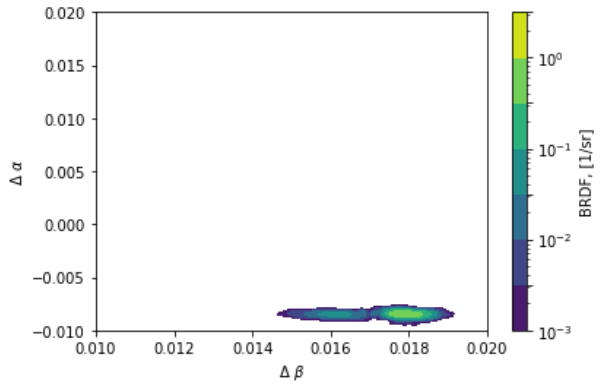

Figure 4.29: Peak 2 appears highly asymmetric in this space and highly stretched in $\Delta\beta$.

In this instance, both Peak 1 and Peak 2 appear highly anisotropic (in comparison to the simulated isotropic data and the lab mirror). Upon performing data processing for the 20° measurements it was found that the measurements of the outermost and innermost contours of Peak 1 and Peak 2 varied greatly (see Table 4.23). Peak 1 is clearly more specular, as the diameter of the BRDF spans a smaller region in direction cosine space, despite the fact that the peak value occurs at Peak 2.

Table 4.23: Table showing the measurements of the innermost and outermost contours for both peaks of the solar panel. The 1st peak has a higher eccentricity and spans a smaller range in direction cosine space than the second peak.

Material	Angle (Deg)	Eccentricity	Semi-Major Axis Scaled (Pixels)	Semi-Minor Axis Scaled (Pixels)	Diameter Scaled	X Center (Pixels)	Y Center (Pixels)
Solar Panel (Outer Peak 1)	20	0.71	45.75	32.52	35.23	132.96	112.37
Solar Panel (Inner Peak 1)	20	0.76	11.33	8.57	9.77	133.69	108.29
Solar Panel (Outer Peak 2)	20	0.30	130.94	36.92	53.36	182.59	185.47
Solar Panel (Inner Peak 2)	20	0.59	33.05	19.42	25.26	212.79	206.08

As a note, for the eccentricity measurements of the solar panel, the diffraction

pattern was not included in measuring the outer and inner contours of Peak 1. (These measurements are included later). The goal here was to note asymmetries in the main peaks not including the diffraction pattern. The eccentricity of the Peak 1 is slightly higher than the baseline for the outer contour, and lower than the baseline for the inner contour, indicating some degree of isotropy in Peak 1. This is not the case for Peak 2, as the inner and outer contours vary significantly in eccentricity, and are far above the baseline eccentricity. Peak 2 also shifts around significantly (looking at the X and Y centers). These measurements indicate a high degree of anisotropy/asymmetry in Peak 2. Table 4.24 shows how symmetric the solar panel data (including both peaks) is, along with how the eccentricity changes for all measured contours.

Table 4.24: The symmetry measurement here was collected by folding the entirety of Figure 4.26 about ϕ_s=π radians. The asymmetry for the solar panel is the highest here out of all of the previously meaured materials. To obtain FWHM, the entirety of Figure 4.26 was converted to direction cosine space, which is why only the Peak 1 row has a measurement, as this data point is for the entire 20° measurement, not just Peak 1. Peak 1 continues to be much more isotropic, measuring a mean eccentricity below the baseline (with a standard deviation slightly above the baseline), while the opposite is the case for Peak 2.

Material	Angle (Deg)	Max Dif Symmetry (%)	Min Dif Symmetry (%)	Mean Dif Symmetry (%)	Mean Eccentricity	STD Eccentricity	FWHM ($\Delta\alpha$)
Solar Panel (Peak 1)	20	3210377.20	5.58×10^{-5}	2619.22	0.76	0.06	0.02
Solar Panel (Peak 2)	20	n/a	n/a	n/a	0.43	0.16	n/a

The symmetry measurements of Table 3.3 are for the entire solar panel plot folded about ϕ_s=π radians (i.e. Figure 4.26 folded about this point). Thus, there is no data for the Peak 2 row, as the symmetry of the entire plot about ϕ_s was represented by the Peak 1 row. The mean and standard deviation of eccentricities are derived from measurements of all of the contours for both Peak 1 and Peak 2. This again does not include the diffraction pattern for Peak 1 (the diffraction pattern will be taken into account in Section 7.4). Peak 2 is more anisotropic, as both the mean and

standard deviation of eccentricity well exceed the baselines. Peak 1 renders as more isotropic, with a mean eccentricity below the baseline, and standard deviation just above the baseline. The differences in isotropy for the two peaks are likely due to the construction of the solar panel itself. Peak 2, which is likley caused by the top glass cover has been glued to the solar cell, and thus is not completely flat, rendering it more anisotropic. Peak 1 is likely made out of uniform metals, rendering it more isotropic, despite the conductive grid lines producing a diffraction pattern. As for the FWHM, it was measured by plotting all of the solar panel data against $\Delta\alpha$, and thus there is no data for row two of the table.

4.8.2 40° Measurements

At first glance, the 40° BRDF measurements (Figure 4.30) appear to be similar to the measurements at 20° as shown in Figure 4.26. However, the peak value of the BRDF is more than two times larger (140,000 vs 64,000), when looking at Peak 2, where the peak value occurred. This increase is the highest rate of increase in BRDF compared to the other materials with respect to θ_i.

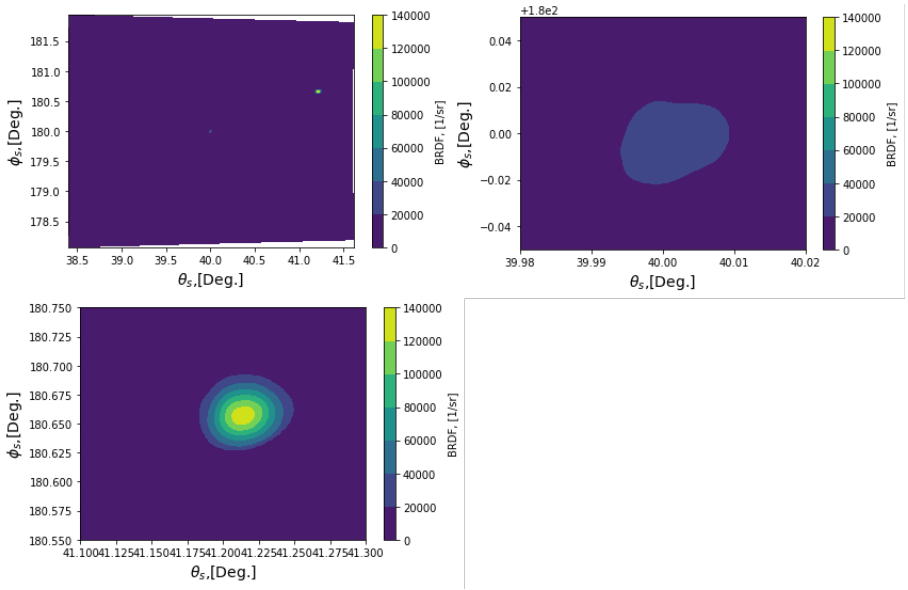

Figure 4.30: Contour plots illustrating the BRDF of the solar panel illuminated at θ_i=40°. The peak BRDF measurement is higher than that of the 20° measurement, increasing by a factor of approximately 2. The first plot is the full plot. To the right in a zoom of the Peak 1, and below is a zoom of Peak 2.

Despite these differences, the 40° measurement still captures two peaks, one centered directly at the specular peak (Peak 1) and another centered off at θ_s=41.22° and ϕ_s=180.66°. Peak 1 still has a diffraction pattern that can be observed when one hones in on Peak 1, as shown in Figure (4.31) below, when both peaks are converted to direction cosine space (Figures 4.31-4.32).

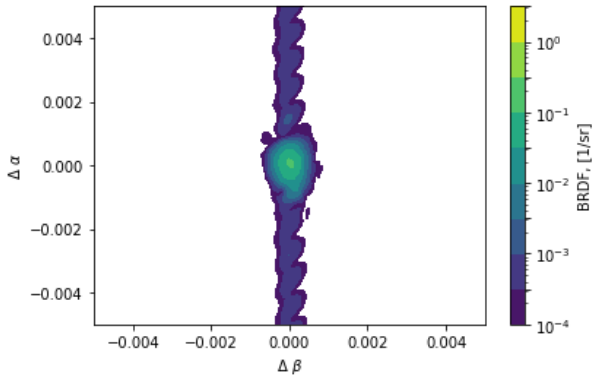

Figure 4.31: Peak 1 continues to have a diffraction pattern centered about a somewhat symmetric looking peak.

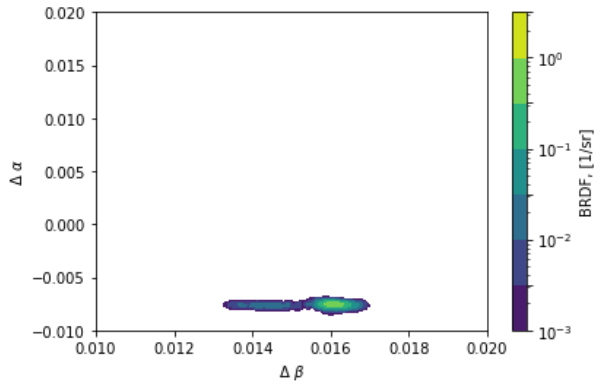

Figure 4.32: Peak 2 continues to stretch significantly in $\Delta\beta$ compared to $\Delta\alpha$.

Comparing Figures 4.31-4.32 to Figures 4.28-4.29, the Peak 1 for both the 20 and 40° measurements appears relatively similar. However, Peak 2 for the 40° measurement appears to extend a much smaller range in direction cosine space than that of the 20° Peak 2 measurement, when plotted on the same scale. It also appears to stretch more in $\Delta\beta$, compared to Figure (4.29). To validate this, the eccentricity, semi-major and semi-minor axes, and diameter of the outer and innermost contours have been collected for the 40° measurement. These measurements have also been scaled using the factor determined in Chapter 3, to account for how a change in θ_s does not correspond directly to an equivalent change $\Delta\beta$ (this depends on θ_i). Table 4.25 show the results for the inner and outer contours.

Table 4.25: For both peaks, the semi-major and semi-minor axes and diameter are smaller for the 40° measurements compared to the 20° measurements, as these extend a smaller region in ϕ_s. The center x and y coordinates are also measured from slightly more consistent points for each contour, although this position still varies significantly between the inner and outer contours of Peak 2. The eccentricities are relatively similar to the 20° measurements.

Material	Angle (Deg)	Eccentricity	Semi-Major Axis Scaled (Pixels)	Semi-Minor Axis Scaled (Pixels)	Diameter Scaled	X Center (Pixels)	Y Center (Pixels)
Solar Panel (Peak 1) Outer	40	0.75	26.17	19.61	22.60	133.71	107.88
Solar Panel (Peak 2) Outer	40	0.29	138.31	40.18	59.20	134.24	166.12
Solar Panel (Peak 1) Inner	40	0.67	8.92	6.00	7.21	134.07	107.22
Solar Panel (Peak 2) Inner	40	0.71	28.95	20.58	24.35	162.80	164.72

As demonstrated by Figures 4.31-4.32 in comparison to Figures 4.28-4.29, the diameter, semi-major and semi-minor axes of the 40° measurements are smaller than those of the 20° measurements reported in Tables 3.1 and 3.2. The center x and y coordinates, however, are measured from slightly more consistent points when comparing the inner and outer contours for each peak, varying more for Peak 2 than for Peak 1. The eccentricities of Peak 1's and Peak 2's contours are relatively similar for the 20 and 40° measurements, excepting the inner contours for Peak 2. For Peak 1, the outer contour measures an eccentricity below the baseline, however, the inner contour measures an eccentricity slightly above the baseline, continuing the trend of recording this peak as leaning isotropic. The inner contour of Peak 2 is similar to the baseline eccentricity, although the outer contour far exceeds the baseline in eccentricity, indicating a high degree of asymmetry/anisotropy. Table 4.26 further investigates

the symmetry of this dataset as well as the overall eccentricity for each contour, and the full width half maximum (FWHM).

Table 4.26: The solar panel is slightly more symmetric at 40° than the 20° data, however, the percentage differences are still higher than those recorded for previous materials. Peak 1 becomes less isotropic, measuring a higher mean eccentricity, while the standard deviation of eccentricity increases for Peak 2, despite recording a lower mean eccentricity. Overall, Peak 1 becomes slightly less isotropic, while Peak 2 maintains a similar degree of anisotropy.

Material	Angle (Deg)	Max Dif Symmetry (%)	Min Dif Symmetry (%)	Mean Dif Symmetry (%)	Mean Eccentricity	STD Eccentricity	FWHM ($\Delta\alpha$)
Solar Panel (Peak 1)	40	2685033.00	0	1634.33	0.69	0.04	0.0008
Solar Panel (Peak 2)	40	n/a	n/a	n/a	0.52	0.18	n/a

Overall, the 40° measurements are slightly more symmetric about ϕ_s=π than the 20° measurements. This is likely due to the fact that the 40° extends a smaller range in ϕ_s, which resulted in overall lower percentage differences for the symmetry. Peak 1 decreases in isotropy, with a higher overall eccentricity compared to the baseline (despite recording the baseline standard deviation), although still leaning towards isotropy. Peak 2 decreases in eccentricity, however, the standard deviation increased, registering this peak as leaning anisotropic. The FWHM was significantly smaller for 40° (25 times smaller), part of which is likely due to the smaller extent of ϕ_s (which is directly related to $\Delta\alpha$ for this θ_i). A smaller ϕ_s range will result in a smaller $\Delta\alpha$ and thus a smaller FWHM. However, since the range was only 2 times smaller, this difference (25 times smaller) is too large to merely be accounted for by this smaller ϕ_s range.

4.8.3 60° Measurements

At 60°, the BRDF peak value drops by a factor of 1.17 from the 40° data, a reverse from the increases observed for the previous materials. Additionally, as can be seen

in Figure 4.33, Peak 2 begins to disappear off of the plot, which resulted in collecting additional data with the detector arm slewed an extra 0.3° to fully capture the second peak. Peak 2 is now located at θ_s=61.65°, and ϕ_s=180.43°.

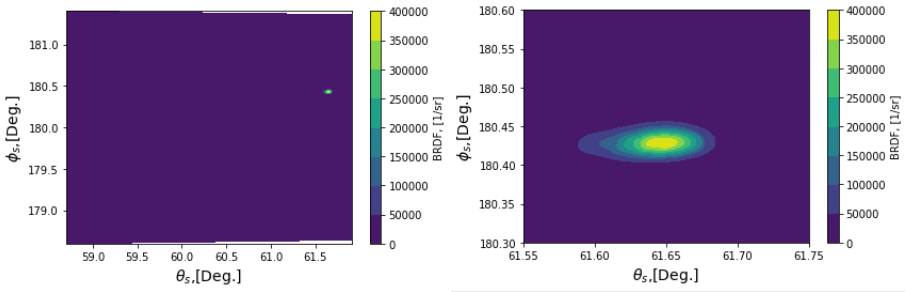

Figure 4.33: Contour plots of the BRDF data in scatter coordinate space for the solar panel illuminated at 60°. The second peak is located slightly off of the captured CCD data, resulting in the detector arm (where the CCD was mounted) being slewed an extra 0.3° to fully capture the second peak. The first plot is the full plot, and the second is the zoom of Peak 2. Peak 1 does not show up on this plot (it must be converted to a log scale to see).

Figures 4.34-4.35 show Peak 1 and Peak 2, respectively in direction cosine space. This data was taken from the slewed detector arm measurements (and this data set was used for the rest of this study in lieu of the original data).

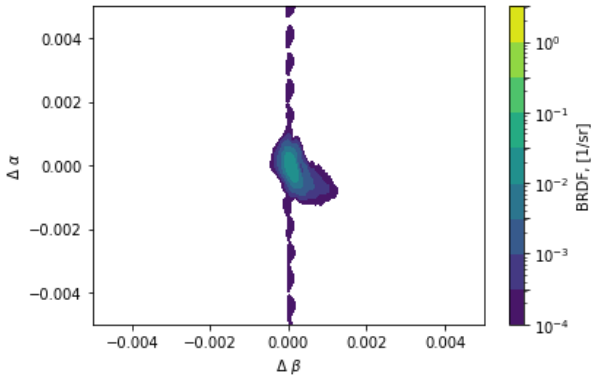

Figure 4.34: Peak 1 appears to stretch more in $\Delta\beta$ compared to previous measurements. This is likely due to the fact that eccentricity generally increases as θ_i increases.

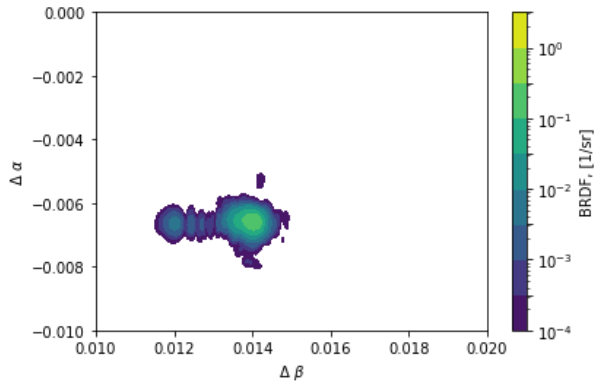

Figure 4.35: Peak 2 appears more symmetric in direction cosine space than the 20° and 40° measurements. It also appears slightly different shape wise, which may be due to a different part of the sample being illuminated as the detector arm was slewed 0.3°.

In Figure 4.35, Peak 2 has noticeably shifted around in direction cosine space from its location measured for 20° and 40°. It also appears to be more symmetric in direction cosine space compared to the lower θ_i. Part of this could be due to the additional slewing of the detector arm. However, Peak 1 (Figure 4.34) is also slightly askew, as the main peak (not including the diffraction pattern) extends a wider range in $\Delta\beta$ as compared to the lower θ_i measurements. Table 4.27 provides measurements of the semi-major and semi-minor axes and diameter, confirming that Peak 1 is somewhat wider in $\Delta\beta$, as the semi-major axis is nearly two times larger than the 40° measurement. However, Peak 2 is also a lot more circular (eccentricity closer to one) compared to smaller θ_i. These widely varying eccentricity measurements for both peaks are an indication that rotatational symmetry is not being maintained as θ_i changes, portending anisotropy.

Table 4.27: Measurements of the inner and outer contours for both Peak 1 and Peak 2 when θ_i=60°. Peak 1 is much more eccentric for 60° than for lower θ_i measurements. It is also somewhat larger in terms of the outer contour dimensions. Peak 2 varies from previous measurements in that it is much less eccentric, and is shifted in direction cosine space (relying upon the Center X and Center Y columns).

Material	Angle (Deg)	Eccentricity	Semi-Major Axis Scaled (Pixels)	Semi-Minor Axis Scaled (Pixels)	Diameter Scaled	X Center (Pixels)	Y Center (Pixels)
Solar Panel (Peak 1) Outer	60	0.49	75.70	36.88	52.17	137.46	111.16
Solar Panel (Peak 2) Outer	60	0.74	87.49	64.93	54.80	102.13	144.02
Solar Panel (Peak 1) Inner	60	0.41	58.29	24.12	36.90	135.79	110.17
Solar Panel (Peak 2) Innerr	60	0.83	26.15	21.78	23.75	106.75	143.06

Table 4.27 confirms a lot of what was observed by looking at Figures 4.34 and 4.35. Peak 1 has become much more eccentric than measurements of Peak 1 at lower θ_i, well exceeding the baseline eccentricity. The outer contour for Peak 1 is also larger than that of the 40° measurements. Peak 2 is significantly smaller than the 40° measurements, and it is shifted in direction cosine space, when one looks at the Center X and Center Y columns in Table 4.27. Peak 2 also records eccentricity measurements for both the inner and outer contour below the baseline, a reversal of previous measurements. This indicates a lack of rotational symmetry, as mentioned previously. Table 4.28 summarizes the contour, symmetry and FWHM data for the solar panel at θ_i=60°.

Table 4.28: The FWHM here is larger than that at 40°, but smaller than the 20° measurement. The eccentricity and standard deviations are comparable to previous measurements. The 60° measurement is more symmetric about ϕ_s, but this is likely due to the smaller range that the plot extends in ϕ_s.

Material	Angle (Deg)	Max Dif Symmetry (%)	Min Dif Symmetry (%)	Mean Dif Symmetry (%)	Mean Eccentricity	STD Eccentricity	FWHM ($\Delta\alpha$)
Solar Panel (Peak 1)	60	1912242.60	1.02×10^{-5}	1190.47	0.47	0.05	0.0017
Solar Panel (Peak 2)	60	n/a	n/a	n/a	0.78	0.03	n/a

In Table 4.28, the standard deviation of eccentricity remains relatively similar to measurements made at lower θ_i, although the eccentricity is on average lower for Peak 2 (in fact, lower than the baseline eccentricity), and higher for Peak 1 (far exceeding the baseline). These large variations from previously recorded eccentricities indicates a lack of rotational symmetry as θ_i increases. The 60° data is also more symmetric in ϕ_s than the 40° data, however, this is likely due to the fact that the plot extends a smaller range in ϕ_s. The FWHM is lower than that that of the 20° measurement, but higher than that of the 40° measurement.

4.8.4 Summary of Solar Panel Data

Overall, the solar panel exhibits characteristics of a highly anisotropic material. Firstly, the existence of a diffraction pattern for each of the measurements at varying θ_i, indicates a highly anisotropic material. The diffraction pattern has been taken into account in the X-center and Y center measurements of Peak 1 in Table 4.29. The algorithm developed by this study indicates that this material is anisotropic, as it registers as anisotropic for each category with the exception of the scaled diameter entry for Peak 2, which has a standard deviation below the baseline. Of these parameters, the degree of asymmetry about ϕ_s is the most significant, exceeding the baseline by a factor of 200. As for the scaled diameters, the standard deviations of both peaks are

lower than those measured for previous materials. However, as previously mentioned, this parameter is a shaky metric, and does not immediately signify material isotropy. It also does not account for alignment uncertainty. For this sample, it was difficult to determine if the sample was aligned with the cover glass or the solar cell underneath. The cover glass is not completely flat, as it is glued on, producing anisotropies. The extra slewing at 60° produced some additional uncertainty in the measurements, as the eccentricity registered as lower there, which may be due to illuminating a different part of the sample.

Looking at the other parameters, the standard deviation of the FWHM is on the order of the mean, indicating anisotropy. The x and y centers register the highest standard deviations, as the inclusion of the diffraction pattern contours significantly increased the standard deviation of Peak 1 (this is where the diffraction pattern was taken into account). While the mean eccentricities recorded for both peaks are lower than measured for Kapton and Polished Aluminum samples, the standard deviations are quite high. This is because the eccentricities vary significantly between different θ_i measurements, indicating a lack of rotational symmetry, and thus anisotropy. Table 4.29 below summarizes these results for the solar panel. Overall, the parameters in Table 4.29 signify that this material is anisotropic, as predicted by the initial visual inspection of the solar panel.

Table 4.29: The solar panel records the highest degree of asymmetry in ϕ_s out of all the materials so far. It also records high standard deviations in the center measurements, when the diffraction pattern is taken into account. These factors, paired with the high standard deviations in eccentricity and FWHM indicate that this sample is anisotropic, as predicted.

Material	Mean Symmetry (% dif)	Scaled Diameter (Pixels)	Scaled FWHM ($\Delta\alpha$)	X Center (Pixels)	Y Center (Pixels)	Eccentricity	Classification
Solar Panel Peak 1	1814.67 ± 731.25	36.67 ± 14.84	0.011 ± 0.011	130.83 ± 27.93	96.04 ± 56.11	0.65 ± 0.13	Anisotropic
Solar Panel Peak 2	n/a	55.79 ± 3.04	n/a	135.59 ± 53.29	161.38 ± 27.02	0.52 ± 0.20	n/a

4.9 Metal Mesh

This section details measurements of the metal mesh taken at 20° and 40°. No 60° measurement was taken due to an issue with being able to adequately slew and collect data at this angle. The uncertainty in alignment for this sample was 0.5°.

4.9.1 20° Measurements

Figure 4.36 shows the metal mesh in scatter coordinate space. The BRDF of the sample is very low, maxing out around 0.9. This is unsurprising, as the mesh sample is highly transmissive as opposed to reflective.

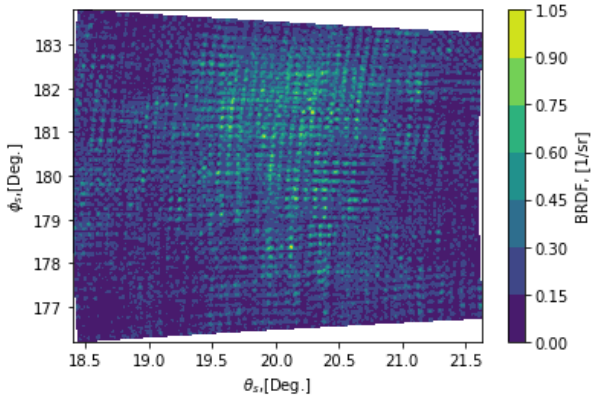

Figure 4.36: Plot of the metal mesh in scatter coordinate space for θ_i=20°. The peak BRDF value is very low, maxing out around 0.9.

When Figure 4.36 is converted to direction cosine space, one finds that there are no ellipses to be extracted from the image. The BRDF is too low and the sample too diffuse for one to use this algorithm. It is obvious that there is a diffraction pattern present in the data, however, even upon narrowing the limits of the plot, the algorithm fails to extract reasonable fits. This here is one of the shortfalls of the image processing technique. Figure 4.37 shows the metal mesh data in direction cosine space for 20°.

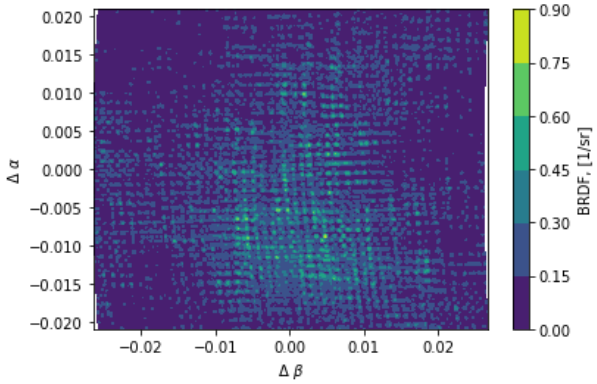

Figure 4.37: Plot of the metal mesh in direction cosine space for 20°. The algorithm is unable to fit ellipses to the data, as it is too diffuse and the BRDF values are too low.

While the algorithm was unable to fit ellipses and measure parameters such as

eccentricity or diameter, data about the symmetry and FWHM was still collected. This data is summarized in Table 4.30. While the mesh was less symmetric in ϕ_s than the lab mirror, on average, the metal mesh had a higher degree of symmetry than the solar panel, kapton and polished aluminum samples for 20°. This again indicates another shortfall of the algorithm, as the sample is clearly visually less symmetric than all of the other samples with its 2D grid. Thus, one cannot use the symmetry parameter on diffuse samples.

Table 4.30: The symmetry of the metal mesh is higher than the symmetry of all of the other materials, excepting the lab mirror for 20°, as the percentage differences were the second lowest (excepting minimum difference). The FWHM is rather small compared to the other materials.

Material	Angle (Deg)	Max Dif Symmetry (%)	Min Dif Symmetry (%)	Mean Dif Symmetry (%)	Mean Eccentricity	STD Eccentricity	FWHM ($\Delta\alpha$)
Metal Mesh	20	5511.24	0	189.37	n/a	n/a	0.0014

4.9.2 40° Measurements

Figure 4.38 shows the metal mesh data for θ_i=40°. As with the 20° measurement, the BRDF remains low, with a peak around 1.4 and representing an increase in BRDF by a factor of about 1.6.

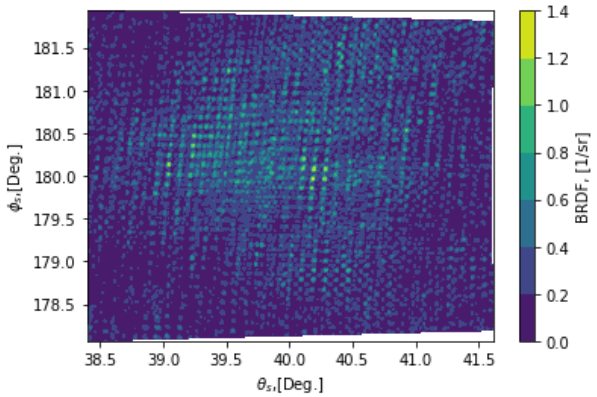

Figure 4.38: Contour plot of the BRDF for the metal mesh at 40°. The peak BRDF increases by a factor of 1.6 here, however, still maintaining a low BRDF with peak around 1.4.

Figure 4.39 shows an attempt to transform the 40° measurements to direction cosine space. As with the 20° measurement, the sample is too diffuse to produce any ellipses that can be detected by the image processing algorithm. However, it is slightly more evident in this plot that the metal mesh produces a 2D diffraction pattern.

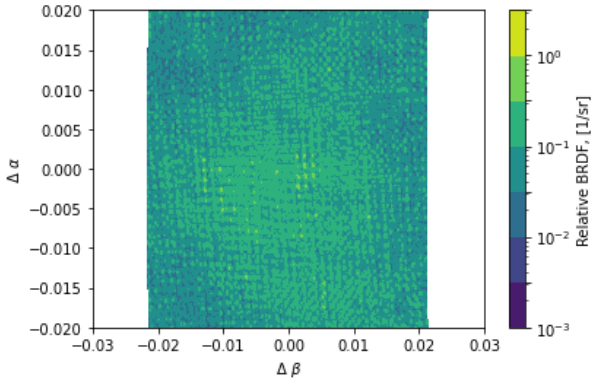

Figure 4.39: Plot of the metal mesh in direction cosine space for 40°. The algorithm is unable to fit ellipses to the data, as it is too diffuse, however, the 40° appears to show signs of a diffraction pattern produced by the material.

As with the 20° measurements, no ellipses were able to be fit and measured by the algorithm. However, the symmetry and FWHM were still able to be measured, and are summarized in Table 4.31. The mean symmetry remains high in comparison

to the other samples, with the exception of the mirror sample, indicating isotropy, contrary to the initial prediction.

Table 4.31: While the max and min symmetry are lower, the mean symmetry of the metal mesh is higher at 40° than at 20°. This is likely due to the smaller spatial extent in ϕ_s. The FWHM decreases by less than half, which is slightly higher than expected. Overall, the metal mesh remains relatively symmetric compared to the other samples.

Material	Angle (Deg)	Max Dif Symmetry (%)	Min Dif Symmetry (%)	Mean Dif Symmetry (%)	Mean Eccentricity	STD Eccentricity	FWHM ($\Delta\alpha$)
Metal Mesh	40	7173.66	2.12×0^{-6}	162.05	n/a	n/a	0.0008

4.9.3 Summary of Metal Mesh Data

The experimental setup prohibited 60° data from being collected. Thus, only the results for 20° and 40° are shown. Overall, this sample was difficult to classify using this algorithm, as there were only two indicators for isotropy for this material, compared to the six normally used to classify the material. This shows a short-fall of the overall algorithm, as diffuse samples cannot be easily classified as isotropic or anisotropic. However, this would have been a shortfall were image processing techniques able to extract parameters such as diameter. This is because the diameter only remains constant as θ_i increases when the sample is very specular. The algorithm attempted to classify the sample as moderately isotropic, as the symmetry was relatively high (second highest out of all samples), and the FWHM (when scaled) had a very low standard deviation (0.0001). However, the sample is obviously anisotropic as it produces a 2D diffraction grid. Had the algorithm been able to detect a distinct pattern, the sample would have registered as more anisotropic. Clearly, ellipse detection does not work well for 2D diffraction patterns, nor for more diffuse samples. This sample ultimately exposed a flaw in the algorithm. The results of the algorithm

are summarized in Table 4.32.

Table 4.32: The algorithm failed to classify the sample. The overall symmetry of the material is the second highest out of all of the materials. Additionally, the standard deviation of the scaled FWHM is very low (0.0001), adding points in favor of isotropy. Without the other parameters, it is difficult to classify the material further, indicating a shortfall in the algorithm.

Material	Mean Symmetry (% dif)	Scaled Diameter (Pixels)	Scaled FWHM ($\Delta\alpha$)	X Center (Pixels)	Y Center (Pixels)	Eccentricity	Classification
Metal Mesh	175.71 $\pm$ 19.32	n/a	0.0015 $\pm$ 0.0001	n/a	n/a	n/a	n/a

4.10 Analysis

In Sections 4-8 of this chapter, each material was discussed and an initial assessment of the material's isotropy/anisotropy was given. This section expounds upon these initial assessments and provides an ranking of each material from most isotropic to most anisotropic, based upon the parameters and baselines established in Chapter 3.7. Table 4.33 is taken from Chapter 3.7 to remind the reader of the established baselines.

Table 4.33: Table summarizing the various baselines and weights for each parameter of isotropicity. STD stands for standard deviation.

Baseline	Scaled Diameter (STD)	X/Y Center (STD)	FWHM (STD)	Eccentricity (Value + STD)	Mean (% difference)
Value	3.35	3.23	0.002	0.73 $\pm$ 0.04	9.11
Weight	0.05	0.18 & 0.18	0.05	0.18 & 0.18	0.18

Using these baselines, each material was measured in terms of how much it deviated from the baseline, and assigned a score. Each parameter was weighted differently, depending upon the reliability of the parameter in assessing material isotropy (ref. Table 4.33). The columns in that were weighted the highest (with a weight of 0.18) were

the mean symmetry, x center and y center, as well as the eccentricity column (both eccentricity close to 1 and low standard deviation were factors), whereas the scaled FWHM and scaled diameter were weighted less (weight of 0.05). This is because any scaling factor introduced reduced the level of confidence in that result. The diameter was already found to be a problematic metric, as it depends upon the contours set by Python when the BRDF is plotted. As θ_i increases, the peak BRDF value increases, and the data that is included in the plot (within two orders of magnitude below the peak), the contours level can shift, creating variations in diameter, that do not necessarily correlate well with the rotational symmetry phenomenon observed by Harvey. Another issue with the scaled diameter term is due to uncertainty in alignment. As the sample is rotated, the beam may drift on the sample, or the spot size becomes elongated, changing the diameter measurement. Thus, the scaled diameter term was mostly used to determine between the Kapton and Polished Alumnium which was more anisotropic, as both had similar rankings before that was taken into account. To rank each of these materials, weights were assigned to each of the six metrics. The mean symmetry, x center, y center, mean eccentricity and standard deviation of eccentricity were weighted 0.18 and the scaled diameter and scaled FWHM, mean eccentricity and standard deviation of eccentricity were weighted 0.05. The percentage difference between the measured value and the baseline was calculated and then weighted by its respective weight. Negative values represent when the data point was below the baseline. Each row then received a final score by summing the weighted percentage differences. The metal mesh sample was not ranked as it could not be assessed for each category. Table 4.34 shows the results of each parameter after being weighted, and the final score for each material. For the solar panel, the higher score was included in the calculation of the final score. In this case, the Peak 2 data used for the x center column, and the Peak 1 data used for the scaled diameter and y

center columns. The Peak 2 data was also used for the eccentricity column, as this metric assesses the eccentricity of contours about the peak BRDF value. The lowest score meant that it was the most isotropic material, and the opposite was the case for the highest score. Scores less than 1 indicate a highly isotropic material. Scores 1-10 indicate a material that leans isotropic. Scores 10 and greater indicate an anisotropic material, and scores higher than 30 indicate a highly anisotropic material.

Table 4.34: The materials are listed from most isotropic to most anisotropic. Some categories were weighted higher than others to produce this order. For example, the symmetry column had a higher weight than the scaled diameter and scaled FWHM. This is because any scaling factor introduced produced some degree of uncertainty about that result. This is why the lab mirror is rated higher than the solar panel, even though the standard deviation is higher on the scaled diameter for the lab mirror. Overall, the parameters that were most important were the symmetry, x center and y center and the standard deviation in eccentricity (paired with the eccentricity being closest to 1).

Material	Scaled Diameter	X Center	Y Center	Scaled FWHM	Mean Eccentricity	STD Eccentricity	Mean Symmetry	Overall Score
Lab Mirror	0.21	-0.10	-0.09	0.08	-0.02	0.27	0.01	0.36
Kapton	0.23	0.27	0.24	0.20	0.14	0.05	9.25	10.38
Polished Aluminum	0.78	2.54	0.94	0.10	0.07	0.68	8.14	13.25
Solar Panel	0.17	2.79	2.95	0.23	0.05	0.72	35.68	42.59

In terms of the robustness of the algorithm in identifying materials as isotropic or anisotropic, some parameters were more robust than others. As discussed previously, the scaled diameter was the least robust parameter, as it was subject more so to the contours set by Python as opposed to actually measuring rotational symmetry. It was able to distinguish the Polished Aluminum sample as being more anisotropic, but failed on the solar panel and mirror samples, identifying the solar panel as more isotropic than the smoothly polished mirror. This diameter metric is also subject to the uncertainties in alignment, as the spot size can be elongated as θ_i increases, causing the diameter to change. The standard deviation in eccentricity also was slightly

less robust than the other parameters, identifying the Kapton as more isotropic than the mirror, despite the fact that Kapton has a significantly higher eccentricity. Interestingly, at each θ_i, the eccentricity was 0.01 for the mirror, but taking into account every contour measurement changed the standard deviation significantly. This was because the eccentricity changed with θ_i, for the mirror sample. However, this was also observed for the simulated data. A more robust measurement would be to average the standard deviation of eccentricity for each θ_i to calculate this standard deviation, and thus more accurately registering a sample as isotropic/anisotropic. Otherwise, each of the metrics performed relatively well in terms of matching the predicted isotropy/anisotropy, as for each of the categories (excepting the diameter and standard deviation of eccentricity), the lab mirror rendered the lowest score. The x/y center, and the mean eccentricity categories ended up being the best measurements of rotational symmetry in direction cosine space. As contour levels changed with θ_i, these parameters acted as substitutes for measuring this symmetry. The more consistent these parameters were with θ_i, denoted a high degree of isotropy.

Measuring the mean symmetry in ϕ_s was generally a robust metric, with the exception of the metal mesh material. This was because the sample, with clear grid lines that should produce anisotropic reflection, rendered as moderately isotropic with this parameter, measuring a high degree of symmetry in this metric than all of the other samples excepting the mirror sample. This was likely due to the fact that the grid produced such small BRDFs, which in turn produced small differences, and lower overall mean percentage difference. The parameter of mean symmetry showed a flaw in the overall algorithm, in that it did not perform well on diffuse data nor on samples which produce a 2D diffraction grid. However, this result was not wholly unexpected, as the algorithm was tuned to look specifically at the data near the specular peak, looking $\pm 2^\circ$ off peak θ_s and $\pm 5^\circ$ off peak in ϕ_s. To confirm this,

the simulated isotropic data was given another look to define the conditions under which this algorithm would work. It was found that the algorithm would likely break when the BRDF dropped below 100 sr^{-1}, or in the case where σ_g is greater than 0.1. Figures 4.40-4.41 show where the BRDF is no longer elliptical in scatter space, and where the algorithm would break, at σ_g greater than 0.1.

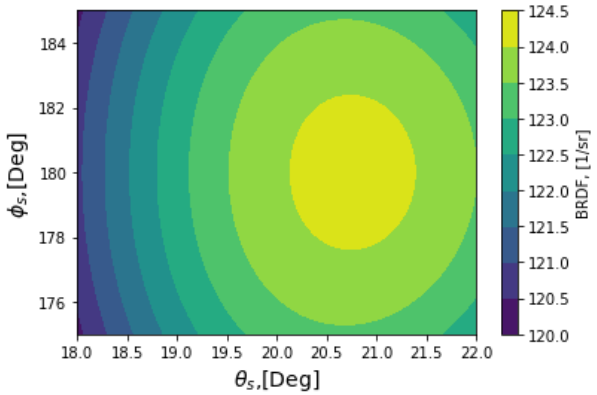

Figure 4.40: Elllipses can still be detected here, where σ_g=0.1.

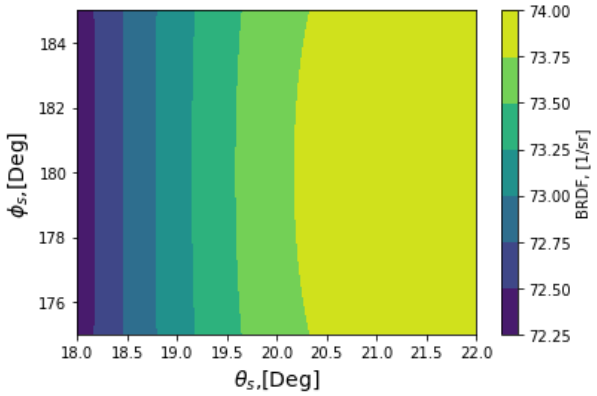

Figure 4.41: The algorithm should break, where the BRDF drops below 100, and σ_g is greater than 0.1. At these points, the plot transitions from an elliptical pattern to a horizontal pattern, where no ellipses can be detected, and the mean symmetry in ϕ_s metric will not work.

4.11 Summary

Overall, the algorithm was able to successfully identify four out of five materials as being conclusively isotropic or anisotropic. The conditions for which the algorithm will work were also defined, as samples where the BRDF drops below 100 sr^{-1}, and where (if modeled using the Beckmann distribution) σ_g is greater than 0.1 cannot be processed by this material. The metal mesh sample was an example where the BRDF was too low, and the presence of the 2D diffraction grid broke the algorithm. The algorithm works best on highly specular materials, and becomes less reliable as the material becomes more diffuse. The x/y center and mean eccentricity criterion are the most robust parameters of the algorithm, able to measure rotational symmetry when the contour levels shift with θ_i better than the scaled diameter metric. Metrics that were flawed or need to be adjusted were the scaled diameter metric (which should be discarded, or adjusted to account for the alignment uncertainty) and the standard deviation of eccentricity, which should be adjusted to be the average standard deviation for each θ_i. Overall, the lab mirror was the most isotropic and similar to the beam signature and simulated data. The solar panel was the most anisotropic material, as it produced two highly asymmetric peaks as well as a diffraction pattern, contributing highly to the anisotropicity, with the Kapton and polished aluminum samples falling in between the mirror and solar panel in terms of anisotropicity. The Kapton sample, which was predicted to lean isotropic, measured barely anisotropic (just above 10). This is possibly due to the fact that if Kapton is not laid completely flat, the reflectance can change. The final results are summarized in Table 4.35.

Table 4.35: Table summarizing the initial prediction compared to the classification done by the algorithm.

Material	Prediction	Score	Classification
Lab Mirror	Isotropic	0.36	Isotropic
Kapton	Leans Isotropic	10.38	Anisotropic
Polished Aluminum	Anisotropic	13.25	Anisotropic
Solar Panel	Highly Anisotropic	42.59	Highly Anisotropic
Metal Mesh	Anisotropic	n/a	n/a

V. Conclusion

5.1 Conclusion

This study began with the goal of developing an algorithm to classify materials as isotropic or anisotropic by merely looking at the BRDF data as opposed to having to fit the data to models to determine the degree of isotropy. First, the characteristics of both isotropic and anisotropic microfacet models were investigated to develop a metric of anisotropy. The microfacet models employed began with looking at the Beckmann distribution function and expanding to the full BRDF data to generate simulated data sets. These simulated data sets generated were 2D contour plots of the BRDF. From the isotropic models, it was found that in scatter coordinate space, isotropic materials reflect light symmetrically about $\phi_s = 180°$. The isotropic models also produced data sets/contour plots that were rotationally symmetric (when scaled appropriately), with a constant diameter as θ_i increased in direction cosine space. Rotational symmetry was defined as maintaining a near constant eccentricity (low standard deviation) of contours in direction cosine space, and various parameters such as the eccentricity and diameter were measured using image processing techniques. The results of investigating the isotropic models helped generate six metrics, which included measurements of the scaled diameter, scaled FWHM, mean and standard deviation of eccentricity, and consistency in center for each ellipse/contour measured. These metrics are the used to generate a score indicating the degree of anisotropy.

While the anisotropic models produced some insights into anisotropy, the models fell short in terms of realistically modeling anisotropic data. As expected, the anisotropic models produced results that were no longer symmetric about ϕ_s=180°. However, these models also produced contour plots in scatter coordinate space that did not adequately account for differing surface roughness in the x and y directions

of a material. While the position of light scattering in a hemisphere depends on the light's incidence angles, θ_i and ϕ_i, it also depends on the surface characteristics upon which the light is reflected. The models do not adequately take into account the varying roughness, as the location where light is scattered solely depends on θ_i and ϕ_i. Changing the parameter controlling the surface roughness in x and y only results in changing the size of the reflected beam, not the location. This was a useful investigation, as it showed that the current anisotropic microfacet models do not adequately represent actual anisotropic surfaces. Thus, the results of the anisotropic models did not contribute to development of the final algorithm used to process actual BRDF data.

The developed algorithm was able to identify materials of varying isotropy, working best on highly specular materials. Each of the materials was first classified as isotropic or anisotropic by a qualitative assessment of the material's surface. The first material was a solar panel sample, which consisted of a top clear layer, and a darker surface underneath with a series of horizontal grid conduction lines. The material is clearly anisotropic due to the directionality of the grid lines (which generated a diffraction pattern). The algorithm was able to successfully identify this surface as anisotropic. The second surface was a Kapton film, which is a semi-transparent film, with no visible machine lining, and some scratches. The algorithm classified this surface as semi-anisotropic, which is likely due to the sample not being laid completely flat, changing the reflectance. The polished aluminum was more clearly anisotropic as the circular polishing lines on the sample was readily visible. As such, the algorithm classified this surface as more anisotropic than the Kapton sample. The lab mirror was the smoothest appearing surface (and was qualitatively classified as such), and the algorithm was able to identify the sample as being slightly less isotropic than the beam signature, which was the baseline. However, the metal mesh sample was unable

to be classified, and was useful in determining the limits of the algorithm. Samples where the BRDF falls below 100 sr^{-1} cannnot be classified by the algorithm, and samples with σ_g greater than 0.1 (using the isotropic Beckmann distribution function) are too optically rough to be classified.

Overall, the the algorithm is robust for relatively specular materials, as employs multiple parameters to successfully analyze out-of-plane BRDF data to classify the degree of isotropy of materials. In its ability to classify materials depending on their degree of isotropy, this algorithm will improve modeling of optical scatter. For example, in light curve analysis, understanding that a solar panel will provide an anisotropic reflection helps not only with tracking of space-based objects, but also in determining other characteristics of said object such as its geometry. Remote sensing and scene generation applications rely upon accurate BRDF models. For example, in remote sensing, accurate modeling of BRDF allows users to determine properties of a remotely sensed scene. This algorithm is better able to classify materials than attempting to fit BRDF data to existing models and then determining the degree of isotropy. As shown in this study, anisotropic models are flawed in that they model non-physical aspects of surface reflection. By circumventing the step of fitting the data to models to determine the surface characteristics, the BRDF can be more accurately characterized, improving the process of extracting scene properties for remote sensing.

5.2 Recommendations for Future Work

From this work, there are several possible avenues for refinement of the algorithm. Firstly, is the scaled diameter metric included in this algorithm. Generally, this metric poorly classified materials, labeling the lab mirror sample as more anisotropic. This was due to the fact that the peak BRDF value changed with θ_i, changing the level of the outermost contour for which the diameter was measured. Even when the diameter

was scaled by an appropriate factor, the standard deviation was significantly higher than the baseline for the lab mirror sample. This also possibly due to some alignment uncertainty, causing the beam to elongate at higher θ_i, and impacting the diameter measurements. Ultimately, the scaled diameter was useful in distinguishing between the degree of isotropy of the Kapton and Polished Aluminum samples. However, it is suggested that this parameter is either removed from the overall algorithm, or a new metric is developed to establish rotational symmetry of isotropic materials in direction cosine space. The eccentricity, FWHM and x/y center metrics serve as intermediate measures of such symmetry, but the diameter metric does not work with contour plots of BRDF. Additionally, another suggestion for the current algorithm is to determine the standard deviation of eccentricity for each θ_i measurement for each material, and average this standard deviation to categorize materials.

This algorithm fell short in successfully classifying all five materials, as it was not able to classify the metal mesh material. As such, a possible area for future work would be to develop an algorithm that can classify highly transmissive materials or materials that create 2D diffraction patterns. The mean symmetry in ϕ_s technique could possibly be refined, possibly drawing on measurements of BTDF to classify these types of materials. The ellipse detection method would likely have to be abandoned. Clearly, the image processing technique of analyzing the contours of a specular BRDF does not work for these types of samples.

Finally, the most ambitious undertaking would be to develop/improve existing anisotropic microfacet models. Currently, the microfacet models are only able to take into account how changing the incidence angles (θ_i,ϕ_i) changes the angles to where light scatters. These models also rely heavily on aligning the sample well so that ϕ_i=$\phi_{material}$. Changing the σ, or width of the distribution function (which is related to the surface roughness), only changes the width of the reflected beam, not where

it scatters. The surface characteristics must also play a role in changing where light scatters. In this, one may have to draw more upon physical optics models to achieve such, as current microfacet models rely upon a series of trigonometric functions (which are based more upon the geometric aspects of optics). The physical optics models can better characterize processes such as diffraction (observed with the solar panel sample) as well as surface characteristics such as differing surface heights in x and y.

Bibliography

[1] Eismann, M. T., *Hyperspectral Remote Sensing*, SPIE Press, 2012.

[2] Nicodemus, F. and et al., "Geometrical Considerations and Nomenclature for Reflectance," *National Bureau of Standards Monograph*, Vol. 160, 1977.

[3] Sandford, B. and Robertson, L., "Infrared reflectance properties of aircraft paint," Proceedings IRIS Targets, Backgrounds and Discrimination, 1985.

[4] Ceniceros, A., Gaylor, D., Anderson, J., and Pinon, E., "Comparison of BRDF-predicted and observed light curves of GEO satellites," Advanced Maui Optical and Space Surveillance Technologies, 2015.

[5] Butler, S. and Marciniak, M., "Comparison of microfacet BRDF model to modified Beckmann-Kirchhoff BRDF model for rough and smooth surfaces," *Optics Express*, Vol. 23, No. 22, 2015.

[6] Montes, R. and Urena, C., "An Overview of BRDF Models," *University of Grenada, Technical Report LSI-2012-001*, 2012.

[7] Rusinkiewicz, S., "A New Change of Variables for Efficient BRDF Representation," Proceedings of The Eurographics Workshop on Rendering, 1998.

[8] Hecht, E., *Optics, Fifth Edition*, Pearson Education Inc., 2017.

[9] Harvey, J., Krywonos, A., and Vernold, C., "Modified Beckmann-Kirchhoff scattering model for rough surfaces with large incident and scattering angles," *Optical Engineering*, Vol. 46, No. 078002, 2007.

[10] Krywonos, A., Harvey, J., and Choi, N., "Linear systems formulation of scattering theory for rough surfaces with arbitrary incident and scattering angles," *J. Opt. Sci. Am.*, Vol. A, No. 28, 2011, pp. 1121–1138.

[11] Beckmann, P. and Spizzichino, A., *The Scattering of Electromagnetic Waves from Rough Surfaces*, Macmillan, 1963.

[12] Butler, S., Nauyoks, S., and Marciniak, M., "Comparison of microfacet BRDF model to modified Beckmann-Kirchhoff BRDF model for rough and smooth surfaces," *Optics Express*, Vol. 23, No. 22, 2015.

[13] Butler, S. and Marciniak, M., "Robust categorization of microfacet BRDF models to enable flexible application-specific BRDF adaptation," Vol. 9205, Proceedings of SPIE, 2014.

[14] Blinn, J., "Models of light reflection for computer synthesized pictures," Proc. 4th annual conference on computer graphics and interactive techniques, 1977.

[15] Torrance, K. and Sparrow, E., "Theory of off-specular reflection from roughened surfaces," *J. Opt. Soc. Am.*, Vol. 57, 1967, pp. 1105–1114.

[16] Cook, R. and Torrance, K., "A Reflectance Model for Computer Graphics," *ACM Transactions on Graphics*, Vol. 1, No. 1, 1982, pp. 7–24.

[17] Ewing, B., Butler, S., and Marciniak, M., "Improved grazing angle bidirectional reflectance distribution function model using Rayleigh-Rice polarization factor and adaptive microfacet distribution function," *Optical Engineering*, Vol. 57, No. 10, 2018.

[18] Ngan, A., Durand, F., and Matusik, W., "Experimental Analysis of BRDF Models," *The Eurographics Association*, 2005.

[19] Matusik, W., Pfister, H., Brand, M., and McMillan, L., "A Data-Driven Reflectance Model," *ACM Transactions on Graphics*, Vol. 22, 2003, pp. 759–769.

[20] Filip, J. and Vavra, R., "Anisotropic Materials Appearance Analysis using Ellipsoidal Mirror," Vol. 9398, Proceedings of SPIE, 2015.

[21] Harvey, J., Goshy, J., and Pfisterer, R., "Modeling Stray Light from Rough Surfaces and Subsurface Scatter," Vol. 9205, Proceedings of SPIE, 2014.

[22] Butler, S., Nauyoks, S., and Marciniak, M., "Experimental Analysis of bidirectional reflectance distribution function cross section conversion term in direction cosine space," *Optics Letters*, Vol. 40, No. 11, 2015.

[23] Johnson, P. and Christy, R., "Optical Constants of the Noble Metals," *Physical Review*, Vol. 6, No. 4370, 1972.

[24] Gonzalez, R. C. and Woods, R. E., *Digital Image Processing, 4th Edition*, Pearson Education Inc., 2018.

[25] Small, T. V., Butler, S. D., and Marciniak, M. A., "Augmenting CASI BRDF measurement device to measure out-of-plane scatter with CCD pixel array," Vol. 11485, Proceedings of SPIE, 2020.

[26] Goodman, J. W., *Introduction to Fourier Optics*, W.H. Freeman and Company, 2017.

REPORT DOCUMENTATION PAGE

Form Approved
OMB No. 0704-0188

1. REPORT DATE *(DD-MM-YYYY)*	2. REPORT TYPE	3. DATES COVERED *(From - To)*
25-03-2021	Master's Thesis	May 2019-Mar 2021

4. TITLE AND SUBTITLE
Data Driven Investigation into the Off-Axis BRDF to Develop an Algorithm to Determine Anisotropicity

5a. CONTRACT NUMBER
F4FGA09014J002

5b. GRANT NUMBER

5c. PROGRAM ELEMENT NUMBER

6. AUTHOR(S)
Werkley, Anne W, 1st Lt, USAF

5d. PROJECT NUMBER
20P503

5e. TASK NUMBER

5f. WORK UNIT NUMBER

7. PERFORMING ORGANIZATION NAME(S) AND ADDRESS(ES)
Air Force Institute of Technology Graduate School of Engineering and Management (AFIT/EN) 2950 Hobson Way Wright-Patterson AFB OH 45433-7765

8. PERFORMING ORGANIZATION REPORT NUMBER
AFIT-ENP-MS-21-M-140

9. SPONSORING/MONITORING AGENCY NAME(S) AND ADDRESS(ES)
Air Force Office of Scientific Research
Attn: Dr. Michael Yakes
875 North Randolph Street
Arlington, VA 22203
COMM 703-696-9586 Email: technicalreports@us.af.mil

10. SPONSOR/MONITOR'S ACRONYM(S)

11. SPONSOR/MONITOR'S REPORT NUMBER(S)

12. DISTRIBUTION/AVAILABILITY STATEMENT
DISTRIBUTION STATEMENT A: APPROVED FOR PUBLIC RELEASE; DISTRIBUTION UNLIMITED.

13. SUPPLEMENTARY NOTES

14. ABSTRACT
The Bi-directional Reflectance Distribution Function (BRDF) is used to describe reflectances of materials by calculating the ratio of the reflected radiance to the incident irradiance. While it was found that isotropic BRDF microfacet models maintained symmetry about \phi_s = \pi, such symmetry was not maintained about the \theta_s = \theta_i axis, except for close to the specular peak. This led to development of a novel data-driven metric for how isotropic a BRDF measurement is. Research efforts centered around developing an algorithm that could determine material anisotropy without having to fit to models. The algorithm developed here successfully classified the degree of anisotropicity in 4 out of 5 samples.

15. SUBJECT TERMS
Optical Scatter, BRDF, Remote Sensing, Scene Generation

16. SECURITY CLASSIFICATION OF:			17. LIMITATION OF ABSTRACT	18. NUMBER OF PAGES	19a. NAME OF RESPONSIBLE PERSON
a. REPORT	b. ABSTRACT	c. THIS PAGE			Lt Col Samuel D. Butler, AFIT/ENP
U	U	U	UU	141	19b. TELEPHONE NUMBER *(Include area code)*: 937-255-3636 samuel.butler@afit.edu